12-2018

First Full Six-Dimensional Phase Space Measurement of a Hadron Beam

Brandon Lee Cathey
University of Tennessee, bcathey1@vols.utk.edu

To the Graduate Council:

I am submitting herewith a dissertation written by Brandon Lee Cathey entitled "First Full Six-Dimensional Phase Space Measurement of a Hadron Beam." I have examined the final electronic copy of this dissertation for form and content and recommend that it be accepted in partial fulfillment of the requirements for the degree of Doctor of Philosophy, with a major in Physics.

Yuri Efremenko, Major Professor

We have read this dissertation and recommend its acceptance:

Alexander Aleksandrov, Sarah Cousineau, Geoffrey Greene, Soren Sorensen

Accepted for the Council:

Dixie L. Thompson

Vice Provost and Dean of the Graduate School

(Original signatures are on file with official student records.)

First Full Six-Dimensional Phase Space Measurement of a Hadron Beam

A Dissertation Presented for the

Doctor of Philosophy

Degree

The University of Tennessee, Knoxville

Brandon Lee Cathey

December 2018

This dissertation is dedicated to my loving parents, Ricky and Jan Cathey.

Acknowledgments

I would first like to express my deepest gratitude to Dr. Sarah Cousineau and Dr. Alexander Aleksandrov for allowing me to work on this project and guiding me throughout. I would also like to thank Dr. Alexander Zhukov, Dr. Robert Welton, and the Spallation Neutron Source operators for maintaining the Beam Test Facility during the project. And thanks to the entire SNS Research Accelerator Division for all their support and advice. Further thanks to my committee members, Dr. Yuri Efremenko, Dr. Geoff Greene, and Dr. Soren Sorensen, for their supportive feedback during this process. My sincerest thanks to the Middle Tennessee State University Physics Department, particularly Dr. Daniel Erenso, Dr. Eric Klumpe, Dr. Victor Montemayor, and my first research advisor, Dr. William Robertson. Thanks also to my graduate cohort for creating a supportive and collaborative environment during our studies, especially Daniel Odell who always pushed me to be better. I would also like to thank Casey Carter, Keaten Holley, and Dr. Joshua Parker, who labored alongside me through our undergraduate careers. Additional thanks to Marcus Swearingen Bates, Dr. Marianne Breinig, Erica Cathey, Michaela Lawrence Jeffery, Chris May, Chrisanne Romeo, and Angela Woody. I would also like to express my sincerest gratitude to Sharena Domingo for her extraordinary help and support. I would especially like to thank my father, Ricky Cathey, for his wisdom, and my mother, Jan Cathey, who taught me how to think like a physicist. Above all, I would like to thank God for blessing me with the opportunities and abilities necessary to excel in this endeavor.

This work was partially supported by the U.S. National Science Foundation under grant PHY-1535312. ORNL is managed by UT-Battelle, LLC, under contract DE-AC05-00OR22725 for the U.S. Department of Energy.

Abstract

A significant limitation for accelerator physics simulation tools is the inability to accurately predict the distribution of particles in a linear accelerator hadron beam. Even state-of-the-art particle-in-cell codes that contain all the relevant physics are only able to reproduce the beam's measured root-mean-square (RMS) parameters. However, characterizing the beam at several standard deviations beyond RMS is necessary to predict beam loss, one of the limiting factors for achievable beam power and performance in high power, high intensity accelerators. The accelerator community agrees that the discrepancy between measurement and simulation stems from a poor understanding of the initial particle phase space distribution entering the linac. This can be credited to the fact that no complete six dimensional measurement of the initial beam distribution entering a linac has ever been accomplished.

This dissertation presents the first complete six-dimensional phase space measurement of a particle beam in a hadron accelerator [1]. The measurement was completed at Spallation Neutron Source Beam Test Facility, a functional duplicate of the SNS front-end capable of producing a pulsed 2.5 MeV H^- ion beam. The technique coordinated six movable slits to isolate small, specified volumes systematically over the full six-dimensional phase space and measure the charge inside each volume. The measurement revealed previously unknown, intensity dependent correlations in the phase space distribution that are not visible in lower dimensional measurements. Results will also serve as a full and accurate particle distribution for bench-marking simulations and predicting beam dynamics at the level which relates to beam loss.

Table of Contents

List of Figures

Chapter 1

Introduction

Modern day hadron linear accelerators are composed of a radio frequency quadrupole followed by a series of accelerating cavities designed for progressively higher energies that together constitute a linac. Large scale modern hadron accelerators generally belong to one of two categories: high energy accelerators and high intensity accelerators. For high intensity accelerators, the goal is to maximize beam intensity by squeezing as many particles into a phase space as possible. Applications for high intensity proton beams include the production of secondary particle beams, such as neutrons, neutrinos, muons, etc.; creation of isotopes for medical applications; and future applications for increasing nuclear fuel availability while removing nuclear waste. In particular, The Spallation Neutron Source (SNS) accelerator creates neutrons by accelerating H^- particles through a linac followed by injection into an accumulator ring. As particles orbit the ring, subsequent particles from the linac are added into the ring, increasing the beam intensity. When the desired intensity is achieved, the beam is extracted from the ring and directed to a liquid mercury target for neutron production. The neutrons produced are used for material science research. The SNS accelerator design is illustrated in Figure 1.1.

Coulomb forces and beam loss are important concerns for accelerators, including SNS. Beam loss is the loss of particles as the beam propagates through the accelerator. At high levels, beam loss results in radio activation of accelerator hardware that impedes the necessary and routine hands-on maintenance of the machine components. For high

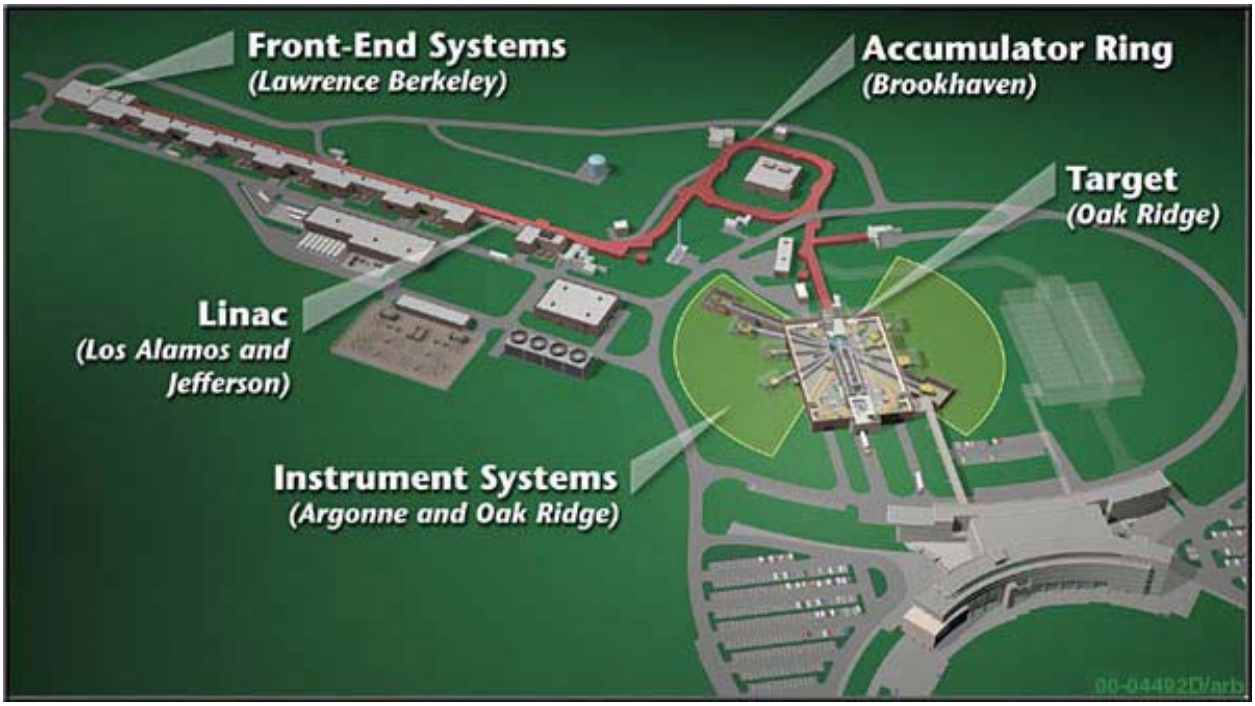

Figure 1.1: Illustration of the SNS accelerator showing the linac, accumulator ring, and target for neutron generation.

density particle beams, strong Coulomb forces contribute heavily to beam evolution and the generation of beam loss.

The field of accelerator physics relies heavily on particle tracking simulations for the study and prediction of beam dynamics. Currently, a significant limitation is the inability of simulation tools to accurately predict the distribution of particles in a linear accelerator hadron beam. Even state-of-the-art particle-in-cell codes that contain all the relevant physics are only able to reproduce the beam's measured root-mean-square (RMS) parameters [2]. However, characterizing the beam at several standard deviations beyond RMS is necessary to predict beam loss. For high power, high intensity accelerators, beam loss is one of the limiting factors for performance and achievable beam power [3]. Accurately predicting beam loss through trusted simulations will lead to improved and novel accelerator designs for next generation accelerators.

There are three components required to accurately simulate a linac: the physics of the accelerating and transport devices, the Coulomb forces between charges, and the phase space particle distribution of the beam entering the linac. The accelerator community agrees that

the physics of the transport devices and the Coulomb forces are accurately represented within simulations. The discrepancy between measurement and simulation is believed to stem from a poor understanding of the actual initial distribution [4, 5, 6, 7]. For linear accelerators in particular, the beam dynamics throughout the linac are intimately dependent on the initial beam entering the system. Without knowing this distribution, there should be no expectation that simulations will accurately predict the beam evolution or beam loss. A particle in an accelerator is described by six independent degrees of freedom (d.o.f.). In a Cartesian coordinate system relative to a design particle, they are the horizontal and vertical positions and their conjugate momentum, $(x, x' = p_x/p_z, y, y' = p_y/p_z)$, the particle energy, w, and the phase measured from the beam repetition frequency, φ. Thus, a beam is fully described by its distribution of particles in the six-dimensional (6D) phase space, and a complete measurement of a distribution must include all six dimensions and their cross-correlations.

A large suite of beam measurement instrumentation, often called beam diagnostics, has been developed to accurately measure properties of a hadron beam as it propagates down the accelerator. For user facilities where the primary function of the beam is dedicated toward external applications or projects, such as the SNS, disruptions to beam propagation need to be limited so that regular operation is maintained as long as possible. As such, many diagnostics are developed to be non-destructive so that measurements can be made without interrupting the beam and therefore neutron production. Beam current monitors (BCMs) and Beam position monitors (BPMs) are the most common non-destructive diagnostics in modern accelerators. BCMs measure the current of the passing particle beam, giving a measurement of the particle count reaching the detector [8]. BPMs measure the average transverse position of the beam [9]. For finding the particle distribution non-destructively, laser-wire scanners are a common tool [10].

The most direct way of measuring the particle distribution is to insert slits into the beam. By blocking all particles except at the slit location, and moving the slit through the beam, the number of particles along an axis can be measured. This is commonly done using only two slits aligned in the same direction to measure a conjugate coordinate pair. Destructive techniques like this have unique concerns due to their direct interference with the beam.

These devices need to be strong enough to withstand the beam power they receive during the measurement. And at user facilities, measurement times need to be short as interference with the accelerator beam for extended periods is problematic.

Unfortunately, traditional beam diagnostics only measure projections of the phase space in one, two, or at most four dimensions. Typically, 2D projections of conjugate position and momentum distribution functions, $f_{\mathrm{x}}(x, x')$, $f_{\mathrm{y}}(y, y')$, $f_{\mathrm{z}}(w, \varphi)$, customarily called emittances, are measured independently [11]. To create an initial 6D distribution f6 for simulations, these 2D projections are assembled together with the assumption that there are no correlations between the d.o.f. not explicitly measured simultaneously:

$$f_6 = f_{\mathrm{x}}(x, x') \cdot f_{\mathrm{y}}(y, y') \cdot f_{\mathrm{z}}(w, \varphi) \tag{1.1}$$

This equation is the definition of uncorrelated distributions f_{x}, f_{y}, f_{z} and is only true if the d.o.f. are independent. For a true six-dimensional scan, all six degrees of freedom need to be measured simultaneously. Such a scan would be able to show any possible correlation that exists in the phase space, not just between conjugate pairs. The implications of this assumption are substantial: any correlation within the phase space has the potential to drive beam evolution. In addition to this, existing experimental measurements do not support this assumption.

Simple linear correlations between transverse dimensions were demonstrated by measuring rms beam parameters [12]. Beyond this, complex correlations have been measured between the transverse rms parameters and longitudinal coordinates for electron beams through the slice emittance technique [13]. Therefore, f_6 is generally not valid, and a direct measurement of the full 6D phase space is required to obtain an accurate distribution for realistic simulations. Specific correlations are known to affect beam evolution [14, 15], and undiscovered correlations could further influence beam dynamics. There have been previous high dimensionality measurements. Pepper-pot methods have demonstrated direct transverse distribution measurements up to 4D [16]. A variety of tomographic techniques have also been developed to reconstruct higher dimensionality distributions using lower dimensionality projections. In general, these techniques are used to reconstruct transverse

or longitudinal 2D projections of the 6D distribution using measured 1D projections [17, 18, 19, 20, 21], or, as seen in one case, to reconstruct the 4D transverse distribution from 1D spatial profiles [22]. The full six-dimensional measurement has not been achieved until this point.

A straightforward method for measuring the 6D phase space distribution of a beam was proposed in [23]. A set of six movable slits is used to localize particles inside a small, specified volume of the 6D phase space: the interval $\pm(\Delta x \Delta x' \Delta y \Delta y' \Delta w \Delta \varphi)$ around the point $(x, x'y, y', w, \varphi)$. Their total charge is measured using a Faraday cup. A Faraday cup schematic is shown in Figure 1.2. They measure the number of ions or electrons that impact with the conducting surface by measuring the current that travels from ground to neutralize the added charge. The particle distribution throughout the phase space is measured by moving all the slits sequentially to span the whole phase volume occupied by the beam. As the scan is sequential, it requires n^6 steps, where n is the number of points per each dimension. In practice, a multi-hour scan is required to achieve a reasonable resolution of 1020 points per dimension. Therefore, the technique is ideally suited for a dedicated facility with significant beam time available for measurement.

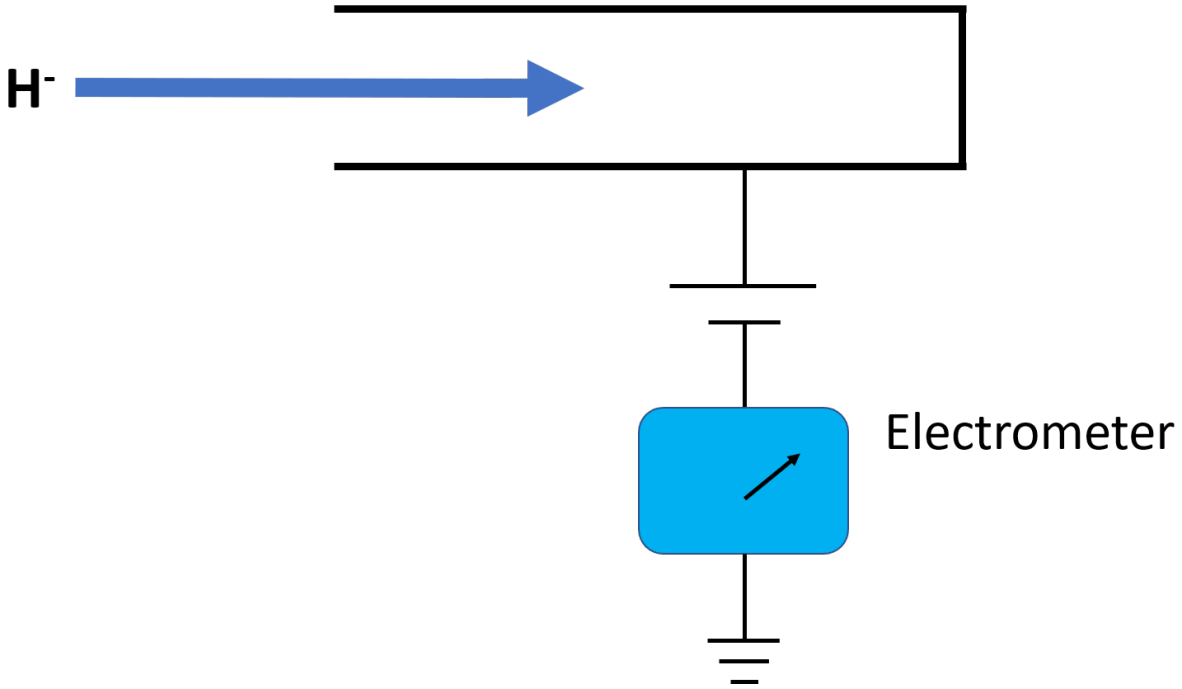

Figure 1.2: Schematic for a Faraday Cup, a diagnostic tool used to measure the number of electrons or ions that impact it.

This technique was implemented at SNS Beam Test Facility (BTF). The BTF is a functional duplicate of the SNS front-end capable of producing a pulsed 2.5 MeV H^- ion beam [24]. Many measurements, including the first full six-dimensional scan, were completed using the BTF. This dissertation details implementation and results from the multidimensional scans conducted on the BTF. Chapter 2 presents the background accelerator physics involved, including the mathematics necessary to determine the six parameters. Chapter 3 explains the experimental setup focusing on the BTF design and component specifications. Finally, Chapter 4 presents the results, including an analysis of the uncertainties and an examination of an unexpected correlation discovered in the measurement.

The measurement has answered questions that have long persisted about the existence of correlations between the six degrees of freedom. It will also serve as a full and accurate particle distribution for benchmarking simulations and predicting beam dynamics at the level which relates to beam loss. These results are an important step in furthering the development of accelerator science.

Chapter 2

Background

2.1 Phase Space

There are six independent degrees of freedom for a particle in an accelerator beam. For a Cartesian coordinate system, the degrees of freedom are the horizontal and vertical positions along with their conjugate momentum (x, x', y, y'), and the energy and phase (w, φ). All coordinates are given relative to a design reference particle, called a synchronous particle, and depend on the position of the synchronous particle, s, along the beam path. This is shown in Figure 2.1. We will define the transverse momentum (x', y') of a particle as the angle of the particle trajectory from the path of the synchronous particle. Since the synchronous particle defines $x = y = 0$, we therefore have:

$$x' = \frac{\mathrm{d}x}{\mathrm{d}s} \quad \text{and} \quad y' = \frac{\mathrm{d}y}{\mathrm{d}s} \tag{2.1}$$

The phase in a non-continuous, or bunched, beam is measured with respect to the beam frequency and shows the time of arrival relative to the synchronous particle. All six dimensions are required to fully characterize a particle in a beam for any position s.

To find the particle distribution, all six degrees of freedom need to be measured over the beam. As discussed previously, the traditional method uses three separately measured two-dimensional scans and combines them to find the full distribution. These scans are of each of the conjugate position and momentum pairs, (x, x'), (y, y'), (w, φ). The three scans

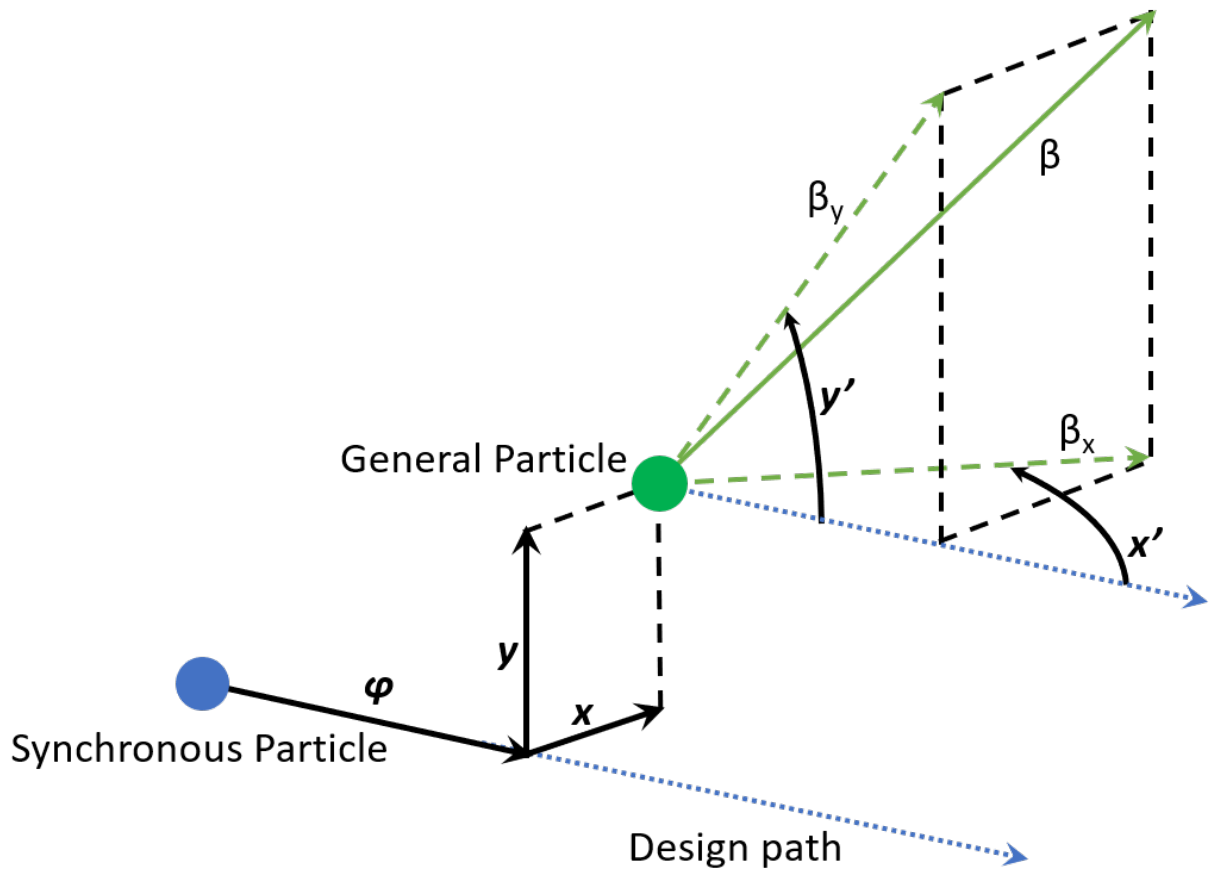

Figure 2.1: Representation of any particle (green) in a distribution. All particles in a distribution are defined relative to the synchronous particle (blue) which travels the design path.

are combined assuming that each two-dimensional scan has no correlation with the other two scans:

$$f_6 = f_{\mathrm{x}}(x, x') \cdot f_{\mathrm{y}}(y, y') \cdot f_{\mathrm{z}}(w, \varphi) \tag{2.2}$$

Because the distribution is typically found by only measuring the (x, x'), (y, y'), and (w, φ) projections, the assumption is that any degrees of freedom not directly measured together have no correlation with each other.

2.2 Phase Space Dynamics

Because particles in a beam repel each other from Coulomb forces, it is necessary to manipulate the particle phase space such that the beam stays contained. For a bunched beam—what SNS uses—all six degrees of freedom need to be contained within physical parameters defined by the accelerator. Of particular importance to this experiment are radio-frequency cavities, quadrupole magnets, and dipole magnets.

2.2.1 Radio-Frequency Cavities

Radio-frequency cavities, or RF cavities, are resonators that serve two purposes: accelerating and bunching particles. RF cavities accomplish this by creating standing waves with a time varying electric current. By tuning the geometry of the cavity, the generated field will point along the longitudinal axis on the beam path. Because the field varies in time, particles must reach the cavity at the correct time when the field vector is pointing in the correct direction with the right magnitude to increase the beam energy to the target energy. If tuned properly, particles arriving early will be given less energy; particles arriving late will be given more energy. This focuses the beam around the design energy and causes the beam to be divided longitudinally into small time scale (nanosecond) microbunches based on the RF frequency. This frequency is the same one used to define the phase of a particle in the six-dimensional phase space. As the beam accelerates, cavities tuned to the same frequency must be spread out so that the design particle always arrives at the correct phase of the electric field. Figure 2.2 shows the concept behind an RF cavity.

2.2.2 Quadrupole Magnets

Quadrupoles in accelerators are used to keep the beam within the transverse spatial parameters. They are created by wrapping wire around four metal poles with alternating magnetic poles to create a magnetic quadrupole. Two pole structures are shown in Figure 2.3. The field is designed to be linear in space so that:

$$\vec{B}(x) = \frac{\mathrm{d}B_y}{\mathrm{d}x} x\hat{y} \quad \text{along the horizontal axis,} \tag{2.3a}$$

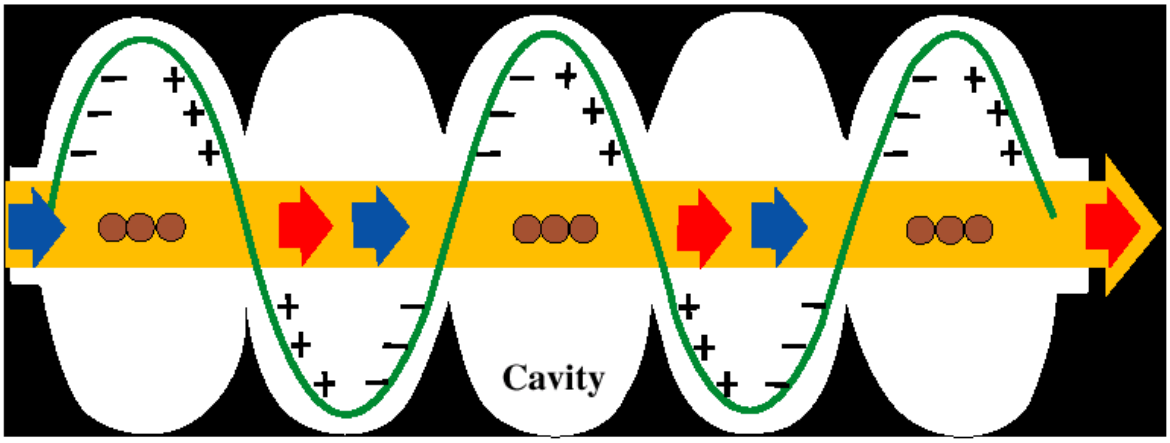

Figure 2.2: Conceptual schematic for a radio-frequency (RF) cavity. The time dependent field accelerates and bunches the particles.

$$\vec{B}(y) = \frac{\mathrm{d}B_x}{\mathrm{d}y} y\hat{x} \quad \text{along the vertical axis.} \tag{2.3b}$$

In order to satisfy Maxwells equation, that $\nabla \times \vec{B} = 0$ in free space, we must have that:

$$\frac{\mathrm{d}B_y}{\mathrm{d}x} = -\frac{\mathrm{d}B_x}{\mathrm{d}x} = G \tag{2.4}$$

Where G is a constant. The Lorentz force on a charged particle going through the quadrupole is then:

$$\vec{F} = m\frac{\mathrm{d}^2\vec{r}}{\mathrm{d}t^2} = e\vec{v_0} \times \vec{B} \tag{2.5}$$

Here, $\vec{v_0}$ is the longitudinal velocity through the accelerator and $\vec{r}$ is the radial position from the quadrupole center. Because particles in an accelerator are moving much faster longitudinally than in either transverse axis, the equation for particles on the horizontal axis becomes:

$$\frac{\mathrm{d}^2x}{\mathrm{d}t^2} = \frac{ev_0}{m} B(x) \tag{2.6}$$

Where x is the horizontal postion at $y = 0$. We also have that:

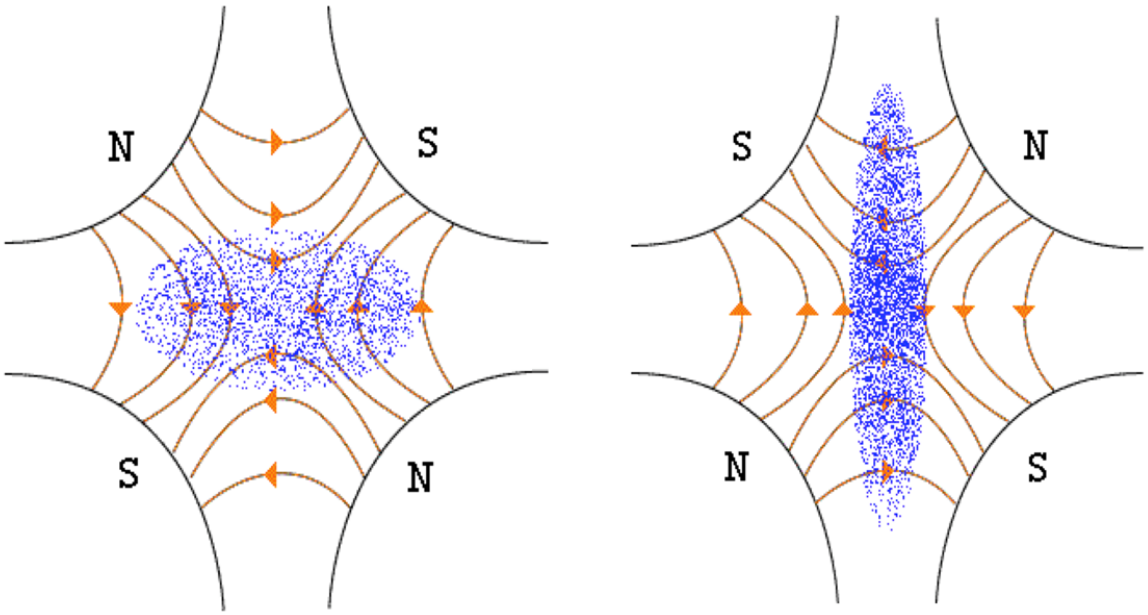

Figure 2.3: Magnetic fields in quadrupoles. The left picture is vertical focusing and the right is horizontal focusing. In both pictures, positive charge is going into the page. It is also apparent how focusing in one direction defocuses in the other.

$$\frac{\mathrm{d}^2x}{\mathrm{d}t^2} = \frac{\mathrm{d}^2x}{\mathrm{d}s^2}\frac{\mathrm{d}^2s}{\mathrm{d}t^2} = v_0^2\frac{\mathrm{d}^2x}{\mathrm{d}s^2} = v_o^2x'' \tag{2.7}$$

Therefore:

$$x'' = \frac{e}{mv_0}\frac{\mathrm{d}B_y}{\mathrm{d}x}x = Kx \tag{2.8}$$

Where K is a constant representing the strength of the quadrupole. Following the same logic for a particle on the vertical axis, we get:

$$y'' = \frac{e}{mv_0}\frac{\mathrm{d}B_x}{\mathrm{d}y}y = -Ky \tag{2.9}$$

Because the field strength increases with distance away from the center, a net focusing affect occurs if K is positive. In this sense, the math describing the effect of quadrupoles on the phase space is analogous to optical lenses. By running the current in one direction, the magnetic fields focus the beam like a convex lens. Conversely, running the current in the opposite direction—switching the poles—will defocus the beam like a concave lens. However,

because the sign in front of K is opposite between axes, focusing in one axis will cause a defocusing effect in the other. For this reason, quadrupoles are usually grouped in pairs to focus the beam overall.

The differential equation above gives as the solution for x:

$$x = A\sin(\sqrt{K}s) + B\cos(\sqrt{K}s) \quad \text{for} \quad K > 0, \tag{2.10a}$$

$$x = A\sinh(\sqrt{|K|}s) + B\cosh(\sqrt{|K|}s) \quad \text{for} \quad K < 0 \tag{2.10b}$$

For the initial conditions $x(0) = x_0$ and $x'(0) = x'_0$, we then have:

$$x = \frac{1}{\sqrt{K}}\sin(\sqrt{K}s)x'_0 + \cos(\sqrt{K}s)x_0 \quad \text{for} \quad K > 0, \tag{2.11a}$$

$$x = \frac{1}{\sqrt{|K|}}\sinh(\sqrt{|K|}s)x'_0 + \cosh(\sqrt{|K|}s)x_0 \quad \text{for} \quad K < 0 \tag{2.11b}$$

The new x' can be calculated with a simple derivative:

$$x' = \cos(\sqrt{K}s)x'_0 - \sqrt{K}\sin(\sqrt{K}s)x_0 \quad \text{for} \quad K > 0, \tag{2.12a}$$

$$x' = \cosh(\sqrt{|K|}s)x'_0 + \sqrt{|K|}\sinh(\sqrt{|K|}s)x_0 \quad \text{for} \quad K < 0 \tag{2.12b}$$

These equations can be expressed together as two matrices, one for the focusing quadrupole:

$$\begin{bmatrix} x \\ x' \end{bmatrix} = \begin{bmatrix} \cos(\sqrt{K}l) & \frac{1}{\sqrt{K}}\sin(\sqrt{K}l) \\ -\sqrt{K}\sin(\sqrt{K}l) & \cos(\sqrt{K}l) \end{bmatrix} \begin{bmatrix} x_0 \\ x'_0 \end{bmatrix} \tag{2.13}$$

and another for the defocusing quadrupole:

$$\begin{bmatrix} x \\ x' \end{bmatrix} = \begin{bmatrix} \cosh(\sqrt{|K|}l) & \frac{1}{\sqrt{|K|}}\sinh(\sqrt{|K|}l) \\ \sqrt{|K|}\sinh(\sqrt{|K|}l) & \cosh(\sqrt{|K|}l) \end{bmatrix} \begin{bmatrix} x_0 \\ x'_0 \end{bmatrix} \tag{2.14}$$

with l being equal to the effective length of the quadrupole. Because the quadrupole effect on each axis is linked, a four-dimensional matrix can be constructed for the transverse plain with x focusing:

$$\begin{bmatrix} x \\ x' \\ y \\ y' \end{bmatrix} = \begin{bmatrix} \cos(\sqrt{K}l) & \frac{1}{\sqrt{K}}\sin(\sqrt{K}l) & 0 & 0 \\ -\sqrt{K}\sin(\sqrt{K}l) & \cos(\sqrt{K}l) & 0 & 0 \\ 0 & 0 & \cosh(\sqrt{|K|}l) & \frac{1}{\sqrt{|K|}}\sinh(\sqrt{|K|}l) \\ 0 & 0 & \sqrt{|K|}\sinh(\sqrt{|K|}l) & \cosh(\sqrt{|K|}l) \end{bmatrix} \begin{bmatrix} x_0 \\ x'_0 \\ y_0 \\ y'_0 \end{bmatrix} \tag{2.15}$$

The matrix for focusing on the y axis is then given by:

$$\begin{bmatrix} x \\ x' \\ y \\ y' \end{bmatrix} = \begin{bmatrix} \cosh(\sqrt{|K|}l) & \frac{1}{\sqrt{|K|}}\sinh(\sqrt{|K|}l) & 0 & 0 \\ \sqrt{|K|}\sinh(\sqrt{|K|}l) & \cosh(\sqrt{|K|}l) & 0 & 0 \\ 0 & 0 & \cos(\sqrt{K}l) & \frac{1}{\sqrt{K}}\sin(\sqrt{K}l) \\ 0 & 0 & -\sqrt{K}\sin(\sqrt{K}l) & \cos(\sqrt{K}l) \end{bmatrix} \begin{bmatrix} x_0 \\ x'_0 \\ y_0 \\ y'_0 \end{bmatrix} \tag{2.16}$$

2.2.3 Bending Magnets

Magnets are used to change the beam path. A bending magnet uses a dipole magnetic field perpendicular to the beam path. The field originates from two conducting coils of wire that lie above and below the beam pipe. Because charged particles in uniform fields travel in circles, we will use circles to determine how particles exit the magnet based on how they enter. The equation for a circle is given by:

$$(X-a)^2 + (Y-b)^2 = r^2 \tag{2.17}$$

Here we are using X and Y to denote the coordinate plane to differentiate them from the phase space coordinates x and y, the center of our particle circle is given by (a, b), and the radius is r. Let the magnetic field only exist in the third quadrant as shown in Figure 2.4. The synchronous particle circle will then be centered on the origin and have the same radius ρ as the bending magnet:

$$X_s^2 + Y_s^2 = \rho^2 \tag{2.18}$$

The radius of any particle can be found using circular motion and the magnetic force:

$$F = \frac{\gamma m v^2}{r} = e(\vec{v} \times \vec{B}) \cdot \hat{r} = evB \tag{2.19}$$

$$r = \frac{\gamma m v}{eB} = \frac{P}{eB} \tag{2.20}$$

where P is the particles momentum. To find the momentum relative to the synchronous particle, we use the term $\frac{P-P_s}{P_s} = \frac{\Delta P}{P_s}$. This momentum expression will be included with the transverse variables to build a transport matrix for a bending magnet. Using the fact that $\rho = \frac{P_s}{eB}$, r can be found as a function of momentum:

$$r - \rho = \frac{P}{eB} - \frac{P_s}{eB} \tag{2.21}$$

$$r = \rho + \frac{\Delta P}{eB} \tag{2.22}$$

$$r = \rho + \rho\frac{\Delta P}{P_s} = \rho\left(1 + \frac{\Delta P}{P_s}\right) \tag{2.23}$$

This shows that r depends only the particles momentum, which makes physical sense.

In the BTF, the dipole magnet bends in the horizontal plane, so we need to focus on how the field affects x, and x'. Figure 2.4 shows the geometry used to calculate the dipole matrix. Here, we constrain the field to the third quadrant. By defining the magnetic field to be bound by the X and Y axes, we can define our circle at $Y = 0$ by how a particle enters the bending magnet. From Figure 2.4, we see that the angle the tangent of the circle at $Y = 0$ makes with a normal line will give x'_0. The slope of the tangent line for a circle can be found by taking the total differential of the equation:

$$2(X - a)\mathrm{d}X + 2(Y - b)\mathrm{d}Y = 0 \tag{2.24}$$

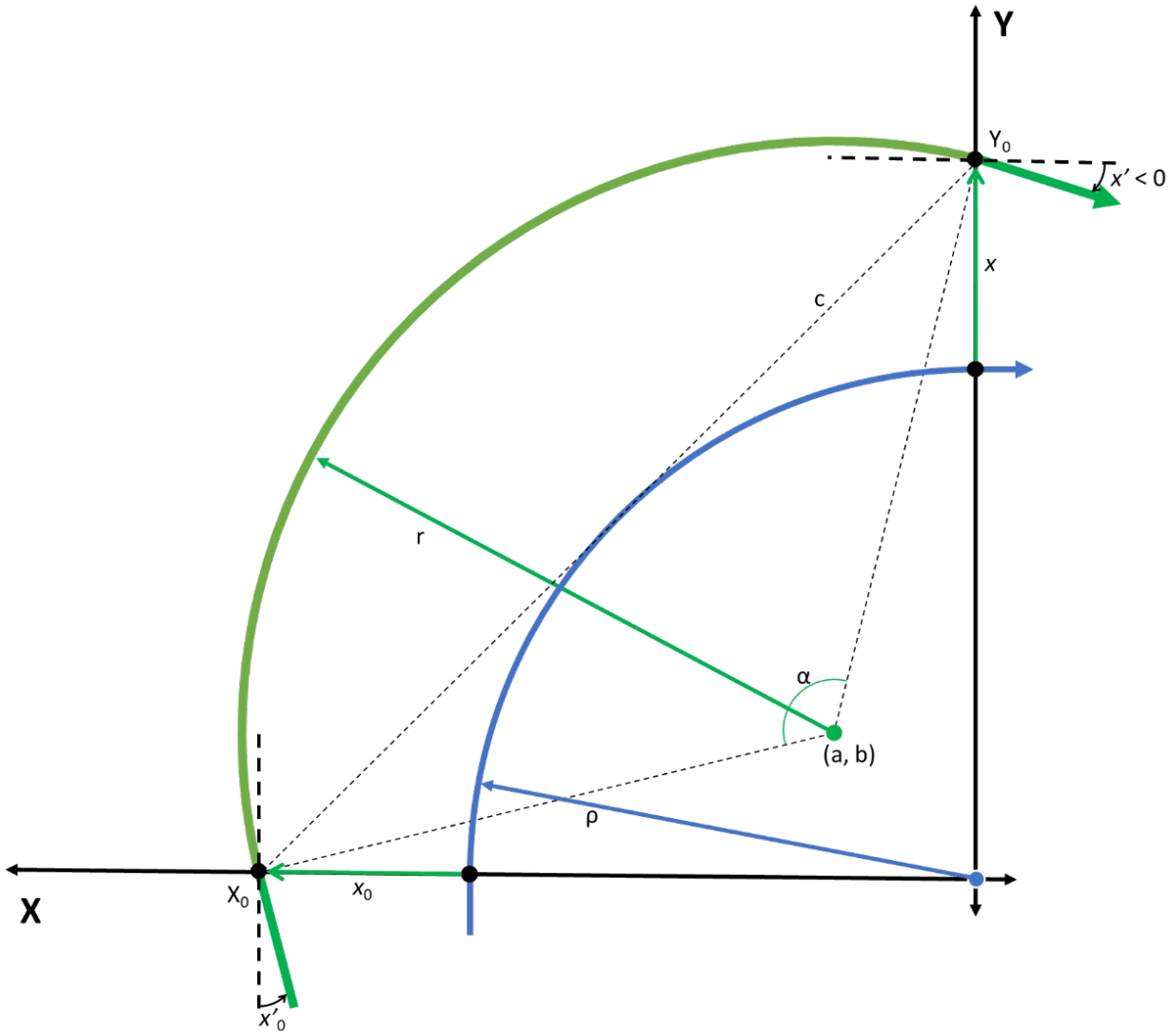

Figure 2.4: The geometry for finding the dipole matrix. The blue path represents the synchronous the particle and the green path is a general particle. A magnetic dipole field is constrained to the quadrant shown.

Solving for the slope gives:

$$-\frac{\mathrm{d}Y}{\mathrm{d}X} = \frac{X-a}{Y-b} \tag{2.25}$$

On the X axis where the particle enters the field, $Y = 0$ and

$$\frac{\mathrm{d}Y}{\mathrm{d}X} = \frac{X_0-a}{b} \tag{2.26}$$

Because the slope of the tangent is the hypotenuse for x_0', the equation for x_0' can be written as:

$$\tan x_0' = -\frac{\mathrm{d}X}{\mathrm{d}Y} = \frac{-b}{X_0-a} \tag{2.27}$$

The negative sign here comes from how a positive angle is defined. The sign of x' is defined to coincide with the sign of x such that a positive x' indicates that x is increasing. Because x_0 is defined opposite of X, x_0' must be as well. From the equation for a circle it is easy to see that on the X axis:

$$X_0 - a = \pm\sqrt{r^2-b^2} \tag{2.28}$$

Because we are only looking at the third quadrant, the negative sign is the correct sign. This gives x as:

$$\tan x_0' = \frac{b}{\sqrt{r^2-b^2}} \tag{2.29}$$

By forming a right triangle and using the Pythagorean theorem, this equation can be rewritten as:

$$\sin x_0' = \frac{b}{r} \tag{2.30}$$

We are only interested in keeping x_0, x_0', and $\frac{\Delta P}{P_s}$ to first order as these differences from the synchronous particle are small. We then use the small angle approximation to show b is:

$$b \approx r x_0' \tag{2.31}$$

This makes sense as a positive b requires a positive x_0' so that the general particle is initially moving away from the synchronous particle. The final unknown in our circle equation is a. This can be determined from analyzing Figure 2.4. The figure shows:

$$X_0 = -\sqrt{r^2 - b^2} + a = -x_0 - \rho \tag{2.32}$$

Remember that x_0 is defined as opposite of X. Therefore, a is given by:

$$a = -x_0 - \rho + \sqrt{r^2 - b^2} \tag{2.33}$$

By substituting for b, a becomes:

$$a = -x_0 - \rho + \sqrt{r^2 - r^2 {x_0'}^2} = -x_0 - \rho + r\sqrt{1 - {x_0'}^2} \tag{2.34}$$

Keeping to first order in ${x_0'}^2$ by using binomial approximation and dropping the higher order terms gives a as:

$$a \approx -x_0 - \rho + r(1 - \frac{1}{2}{x_0'}^2) \approx -x_0 - \rho + r \tag{2.35}$$

With the circular motion for a particle completely defined relative to the synchronous particle, its possible to determine how the particle will leave the magnetic field relative to the synchronous particles exit. Because the experiment described below only involves a 90° bending magnet, we will define the magnetic field to end on the Y axis. From Figure 2.4, the particle crosses the Y axis at:

$$Y_0 = \rho + x = \pm\sqrt{r^2 - a^2} + b \tag{2.36}$$

The positive sign is the correct choice here so that Y_0 stays positive. Note that so x is defined consistently around the bend, the sign of x is the same as Y_0. This is shown clearly in Figure 2.4. Solving for the variable we want, x, gives us:

$$x = -\rho + b + \sqrt{r^2 - a^2} \tag{2.37}$$

Plugging in for a and b gives:

$$x = -\rho + rx_0' + \sqrt{r^2 - (-x_0 - \rho + r)^2} \tag{2.38}$$

$$x = -\rho + rx_0' + \sqrt{r^2 - {x_0}^2 - \rho^2 - r^2 - 2\rho x_0 + 2rx_0 + 2\rho r} \tag{2.39}$$

$$x = -\rho + \rho\left(1 + \frac{\Delta P}{P_s}\right)x_0' + \sqrt{-{x_0}^2 - \rho^2 - 2\rho x_0 + 2\rho\left(1 + \frac{\Delta P}{P_s}\right)x_0 + 2\rho^2\left(1 + \frac{\Delta P}{P_s}\right)} \tag{2.40}$$

We now keep x_0 and $\frac{\Delta P}{P_s}$ to first order and find:

$$x = -\rho + \rho x_0' + \sqrt{-\rho^2 + 2\rho^2\left(1 + \frac{\Delta P}{P_s}\right)} \tag{2.41}$$

$$x = -\rho + \rho x_0' + \rho\sqrt{1 + 2\frac{\Delta P}{P_s}} \tag{2.42}$$

Another binomial approximation gives:

$$x = -\rho + \rho x_0' + \rho\left(1 + \frac{\Delta P}{P_s}\right) \tag{2.43}$$

$$x = \rho x_0' + \rho\frac{\Delta P}{P_s} \tag{2.44}$$

The exit angle x' is found in a similar method to x_0'. The slop of the tangent line at the Y axis can be found from Figure 2.4:

$$\frac{\mathrm{d}Y}{\mathrm{d}X} = \frac{a}{Y - b} \tag{2.45}$$

At $X = 0$, this becomes:

$$\frac{\mathrm{d}Y}{\mathrm{d}X} = \frac{a}{\sqrt{r^2 - a^2}} \tag{2.46}$$

Figure 2.4 shows a situation where $x' < 0$ as the angle means x is decreasing. In general, x' can be written as:

$$\tan x' = \frac{a}{\sqrt{r^2 - a^2}} \tag{2.47}$$

Following the same logic as before, we find that:

$$\sin x' \approx x' = \frac{a}{r} \tag{2.48}$$

$$x' = \frac{-x_0 - \rho + r}{r} \tag{2.49}$$

$$x' = -\frac{1}{\rho}\left(1 + \frac{\Delta P}{P_s}\right)^{-1} x_0 - \left(1 + \frac{\Delta P}{P_s}\right)^{-1} + 1 \tag{2.50}$$

$$x' = -\frac{1}{\rho}\left(1 - \frac{\Delta P}{P_s}\right) x_0 - \left(1 - \frac{\Delta P}{P_s}\right) + 1 \tag{2.51}$$

$$x' = -\frac{1}{\rho} x_0 + \frac{\Delta P}{P_s} \tag{2.52}$$

The particle energy and vertical phase space are unaffected by a dipole magnet so only the effect on the particle phase is left to be examined. For the transfer matrix being constructed, we will use the change in path length, λ, to determine how the bending magnet affects longitudinal placement. From Figure 2.4, we see the that the change in λ over the path will be the difference in arc length from the X axis to the Y axis between the particle and the synchronous particle:

$$\lambda = \alpha r - \frac{\pi \rho}{2} \tag{2.53}$$

where α is the angle on the general particle circle between the axes. To find α, the law of cosines (see Figure 2.4) can be used to give:

$$c^2 = r^2 + r^2 - 2r^2 \cos\alpha \tag{2.54}$$

$$\cos\alpha = 1 - \frac{c^2}{2r^2} \tag{2.55}$$

$$\cos\alpha = 1 - \frac{c^2}{2\rho^2}\left(1 + \frac{\Delta P}{P_s}\right)^{-2} \tag{2.56}$$

Because the changes from the synchronous path are small, we can rewrite $\cos\alpha$ as $\sin\left(\frac{\pi}{2} - \alpha\right)$ and use the small angle approximation to write:

$$\alpha = \frac{\pi}{2} - 1 + \frac{c^2}{2\rho^2}\left(1 - 2\frac{\Delta P}{P_s}\right) \tag{2.57}$$

The distance between the two end points, c, is found using (keeping to first order):

$$c^2 = |(0, Y_0) - (X_0, 0)|^2 \tag{2.58}$$

$$c^2 = |(X_0, Y_0)|^2 \tag{2.59}$$

$$c^2 = {X_0}^2 + {Y_0}^2 \tag{2.60}$$

$$c^2 = (-x_0 - \rho)^2 + (\rho + x)^2 \tag{2.61}$$

$$c^2 = 2\rho^2 + 2\rho x_0 + 2\rho x \tag{2.62}$$

$$c^2 = 2\rho^2 + 2\rho x_0 + 2\rho\left(\rho x_0' + \rho\frac{\Delta P}{P_s}\right) \tag{2.63}$$

$$c^2 = 2\rho^2 \left(1 + \frac{x_0}{\rho} + x_0' + \frac{\Delta P}{P_s}\right) \tag{2.64}$$

Therefore:

$$\alpha = \frac{\pi}{2} - 1 + \left(1 + \frac{x_0}{\rho} + x_0' + \frac{\Delta P}{P_s}\right)\left(1 - 2\frac{\Delta P}{P_s}\right) \tag{2.65}$$

$$\alpha = \frac{\pi}{2} - 1 + 1 + \frac{x_0}{\rho} + x_0' + \frac{\Delta P}{P_s} - 2\frac{\Delta P}{P_s} \tag{2.66}$$

$$\alpha = \frac{\pi}{2} + \frac{x_0}{\rho} + x_0' - 1\frac{\Delta P}{P_s} \tag{2.67}$$

Substituting for α, λ finally gives:

$$\lambda = \left(\frac{\pi}{2} + \frac{x_0}{\rho} + x_0' + \frac{\Delta P}{P_s}\right)\rho\left(1 + \frac{\Delta P}{P_s}\right) - \frac{\pi\rho}{2} \tag{2.68}$$

$$\lambda = \frac{\pi}{2}\rho + x_0 + \rho x_0' - \rho\frac{\Delta P}{P_s} + \frac{\pi}{2}\rho\frac{\Delta P}{P_s} - \frac{\pi\rho}{2} \tag{2.69}$$

$$\lambda = x_0 + \rho x_0' + \rho\left(\frac{\pi}{2} - 1\right)\frac{\Delta P}{P_s} \tag{2.70}$$

The final equation also needs to include any previous changes to the path length occured before the bending magnet. This just adds the old path change, λ_0, as another term:

$$\lambda = x_0 + \rho x_0' + \lambda_0 + \rho\left(\frac{\pi}{2} - 1\right)\frac{\Delta P}{P_s} \tag{2.71}$$

We can now construct a matrix for a bending magnet to first order:

$$\begin{bmatrix} x \\ x' \\ \lambda \\ \frac{\Delta P}{P_s} \end{bmatrix} = \begin{bmatrix} 0 & \rho & 0 & \rho \\ -\frac{1}{\rho} & 0 & 0 & 1 \\ 1 & \rho & 1 & \rho\left(\frac{\pi}{2} - 1\right) \\ 0 & 0 & 0 & 1 \end{bmatrix} \begin{bmatrix} x_0 \\ x_0' \\ \lambda_0 \\ \frac{\Delta P_0}{P_s} \end{bmatrix} \tag{2.72}$$

2.2.4 Radio-Frequency Quadrupoles

A radio frequency quadrupole (RFQ) is a clever device used to simultaneously focus particles in all three spatial dimensions while accelerating the beam. As with an RF cavity, standing electric radio waves are used to manipulate particles. Instead of cavities, the particles travel between four electrodes near the center of the RFQ. The mode used for the electric field oscillates between the vertical electrodes and horizontal electrodes, such that the charge between adjacent electrodes is always opposing. The electrodes are also modulated so that when the vertical electrodes encroach on the beam path, the horizontal electrodes are retreating from the center space and vice versa (See Figure 2.5). The complex interaction between the standing wave and modulation mimics the RF cavity effect, and an alternating longitudinal field is created between the ridges of adjacent electrodes. This simultaneously accelerates the beam and creates the micro-bunches as described above with RF cavities; both effects are shown in Figure 2.6. Additionally, the RFQ ridges initial close density (Figure 2.7) allows for this fine structure to be created adiabatically from a longitudinally free beam.

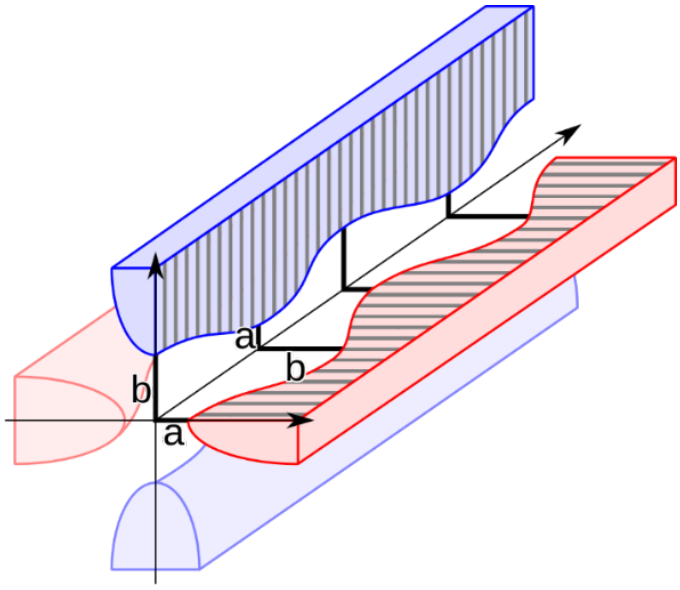

Figure 2.5: Conceptual schematic of RFQ electrodes.

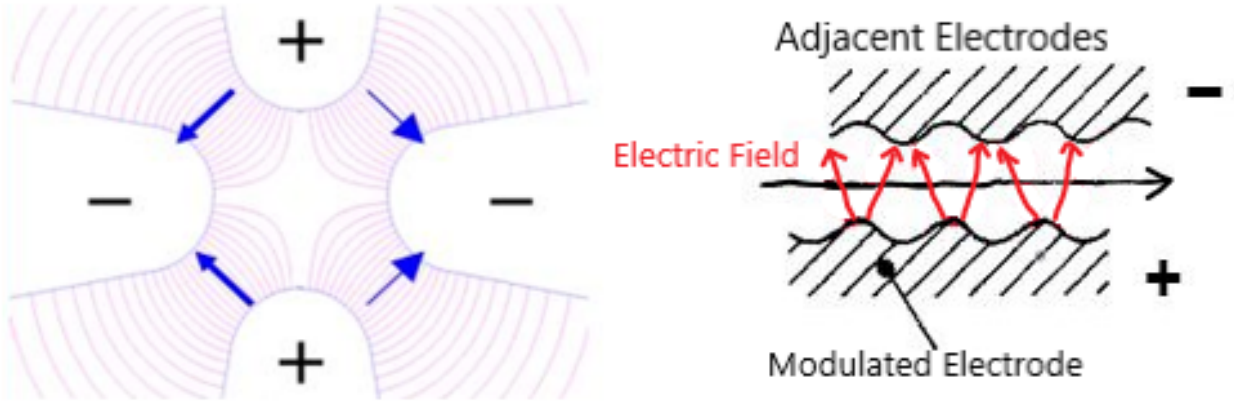

Figure 2.6: Electric fields in an RFQ. The left shows the transverse electric field forming a quadrupole. The right shows how adjacent electrodes form the longitudinal forces that accelerate and bunch particles in a beam.

2.3 Phase Space

Within a particle distribution, correlations can develop between the six dimensions of the phase space. Obvious examples of this are between conjugate space and momentum pairs. These cases are well studied and can be measured using conventional diagnostics. Correlations between dimensions of different axes have traditionally been assumed to not exist. However, the physics within an accelerator allow for the creation of correlations between non-conjugate dimensions. Rotated quadrupoles, solenoid magnets, and self-created Coulomb forces are all capable of causing these correlations, and existing experimental measurements discussed in the previous chapter showed their existence [12, 13].

Because linacs are single pass systems, the evolution of the beam is intimately related to the initial distribution. To show the effect of correlations between the independent variables within the initial distribution on the evolution of the beam, two similar beams were simulated to travel down the same beam line. One beam was based on a Kapchinsky-Vladimirsky (KV) distribution, a well-known distribution often used in accelerator physics that has a complicated correlation between the four transverse degrees of freedom [25]. The other beam was created by taking the KV beam, simulating a typical phase space measurement of scanning separately the (x, x') and (y, y') spaces, and putting these measurements together assuming no correlations. In this method, the correlation between the x and y axis has been removed from the initial KV distribution, but the conjugate position and momentum

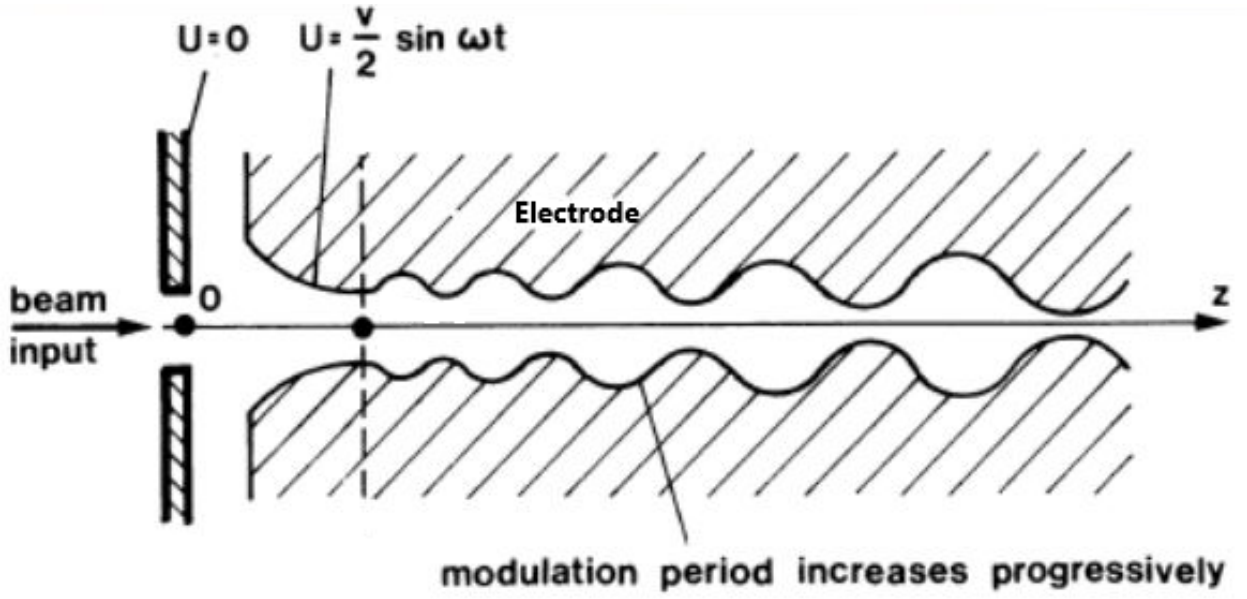

Figure 2.7: This a diagram of electrodes on opposite sides. Increasing modulation period maintains the beam arrival phase relative to the RFQ frequency during acceleration.

distribution spaces that are typically measured remain identical between the two beams (Figure 2.8). Using these two distributions as initial distributions, both beams were modeled traveling through a beam line consisting only of alternating focusing and defocusing quadrupoles. Without space charge, little difference could be seen in the evolution of the two beams after traveling the beam line. However, with space charge, the uncorrelated distribution was seen to grow much larger in size than its correlated counterpart (Figure 2.9). Both beams initially would be indistinguishable without higher dimensional measurements, demonstrating the importance of measuring all six dimensions to properly characterize a beam.

2.4 Phase Space Measurements

A phase space can be measured by dividing the space onto a grid with the appropriate dimensions and measuring the charge at each grid point. Measuring a specific grid point can be accomplished by blocking particles of the beam everywhere but a specified coordinate and measuring the remaining charge that reaches a diagnostic at the end of the beam line, such as a Faraday cup (Figure 1.2). For example, a vertical slit passing through the beam

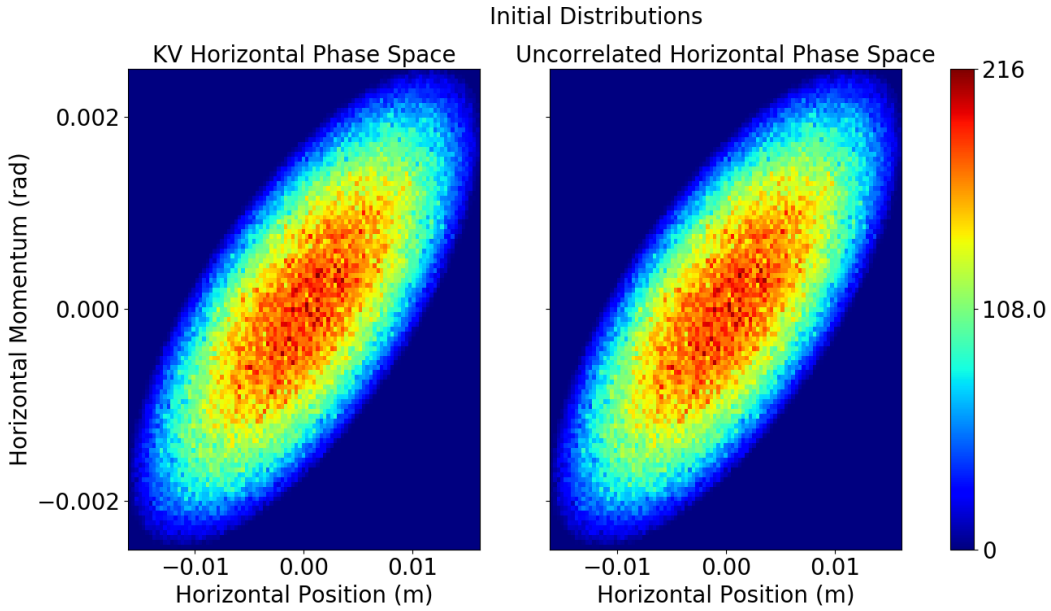

Figure 2.8: A KV distribution (left) and an uncorrelated distribution (right) before simulation. The uncorrelated beam was created by randomizing each conjugate 2D phase against the others. In a traditional machine, there would be no way to distinguish the two.

can be used to find the horizontal projection by measuring the charge that accumulates at different horizontal positions of the slit. A horizontal slit works similarly for the vertical projection. To find the (x, x') projection, two vertical slits traverse the beam with the first slit specifying the horizontal position x. Finding $x' = \frac{\mathrm{d}x}{\mathrm{d}s}$ is done by taking the difference between the slit horizontal positions, $\mathrm{d}x$, and divided by the distance between them, $\mathrm{d}s$. The (y, y') projection is found similarly with horizontal slits. This double-slit technique is a common method of measuring the beam distribution and is one way the 2D emittances described previously are measured. Other methods were already discussed in Chapter 1 [16, 17, 18, 19, 20, 21, 22].

A true 6D scan requires every dimension to be measured simultaneously. Because measuring the distribution requires blocking particles, each dimension decreases the signal strength. If a Gaussian distribution is assumed for each dimension, the current can be described as:

$$I = I_0 \frac{\exp\left(-\frac{x^2}{2\sigma_x{}^2} - \frac{x'^2}{2\sigma_{x'}{}^2} - \frac{y^2}{2\sigma_y{}^2} - \frac{y'^2}{2\sigma_{y'}{}^2} - \frac{w^2}{2\sigma_w{}^2} - \frac{\phi^2}{2\sigma_\phi{}^2}\right)}{8\pi^3} \tag{2.73}$$

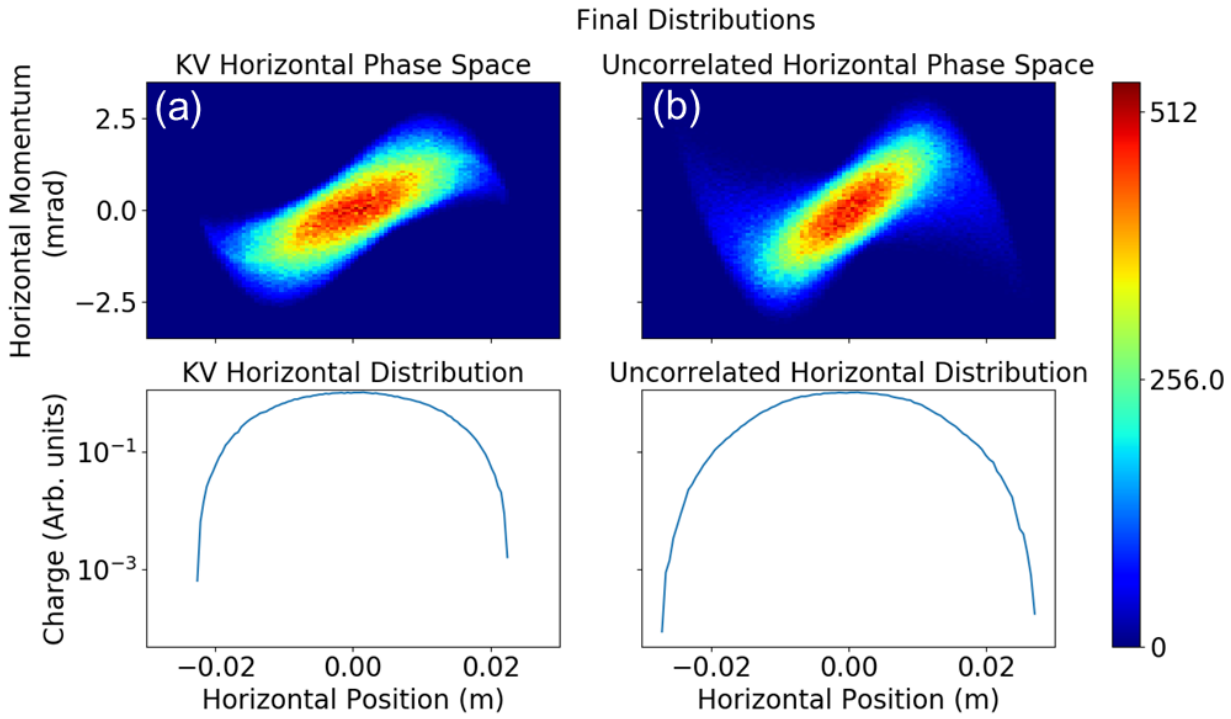

Figure 2.9: The correlated KV beam (a) after propagating through a beam line and its uncorrelated copy (b) having formed a beam halo.

Where I_0 is the total current, x, y, x', y', w, and ϕ are the phase coordinates described previously, and is the standard deviation for each dimension. The current that passes through a small gap of each dimension can be approximated by:

$$I = I_0 \frac{\exp\left(-\frac{x^2}{2\sigma_x{}^2} - \frac{x'^2}{2\sigma_{x'}{}^2} - \frac{y^2}{2\sigma_y{}^2} - \frac{y'^2}{2\sigma_{y'}{}^2} - \frac{w^2}{2\sigma_w{}^2} - \frac{\phi^2}{2\sigma_\phi{}^2}\right)}{8\pi^3} \frac{\Delta x}{\sigma_x}\frac{\Delta x'}{\sigma_{x'}}\frac{\Delta y}{\sigma_y}\frac{\Delta y}{\sigma_{y'}}\frac{\Delta w}{\sigma_w}\frac{\Delta \phi}{\sigma_\phi} \tag{2.74}$$

Where Δ represents the gap width for each dimension. We will assume a gap width of $\frac{\Delta}{\sigma} \approx 0.2$ and use a current of $I_0 \approx 32$mA with a beam pulse of $\tau \approx 50\mu$s to get $N_0 \approx 10^{13}$ starting particles. This gives $N_{final} \approx 2.6 \cdot 10^6$ for the number of particles after six slits at the center of the particle distribution, $r = 0$. At $r = 1\sigma$ we get $N_{final} \approx 1.6 \cdot 10^6$, $r = 3\sigma$ gives $N_{final} \approx 2.9 \cdot 10^4$, and $r = 5\sigma$ yields $N_{final} \approx 9.7$. A Faraday cup is sensitive down about 10^4 particles, which limits us to 3σ, but it should be noted that the goal of this measurement is to determine the distribution at the beam core that causes beam growth, not to measure the beam extremum directly.

The second and much more limiting factor in completing a 6D measurement is the time it takes to perform a scan. In order to fully cover all dimensions, each dimension needs to be scanned for each other dimension. This means scanning the full area for two-dimensions, and the full volume for three-dimensions. A six-dimensional scan needs to then cover a full six-dimensional space, giving the equation for the total number of measurements as:

$$N_{bins} = m^6 \tag{2.75}$$

where m is the number of steps along a dimension. With a sparse 10 points per dimension, a total of 1,000,000 measurements will need to be taken. With a scan rate of one measurement per second, a complete scan will take 280 hours or about two weeks. A faster rate of 10 measurements per second would still take 28 hours. These long times require stability with very consistent results and a beam that is not shared with users—a challenge for large facilities to accommodate.

Chapter 3

Measurement

3.1 The Beam Test Facility

This first six-dimensional phase space measurement was performed at the SNS Beam Test Facility (BTF), which is a functional duplicate of the first section of the main SNS accelerator [24]. The BTF was built at SNS for the purpose of optimizing hardware, testing and commissioning spare RFQs, and performing beam dynamics experiments for high intensity beams, including high dimensionality phase space measurements. Because the BTF is not for neutron production, the beam was not shared with users and could thus be dedicated to high dimensionality scans. Figure 3.1 shows a schematic of the beam line.

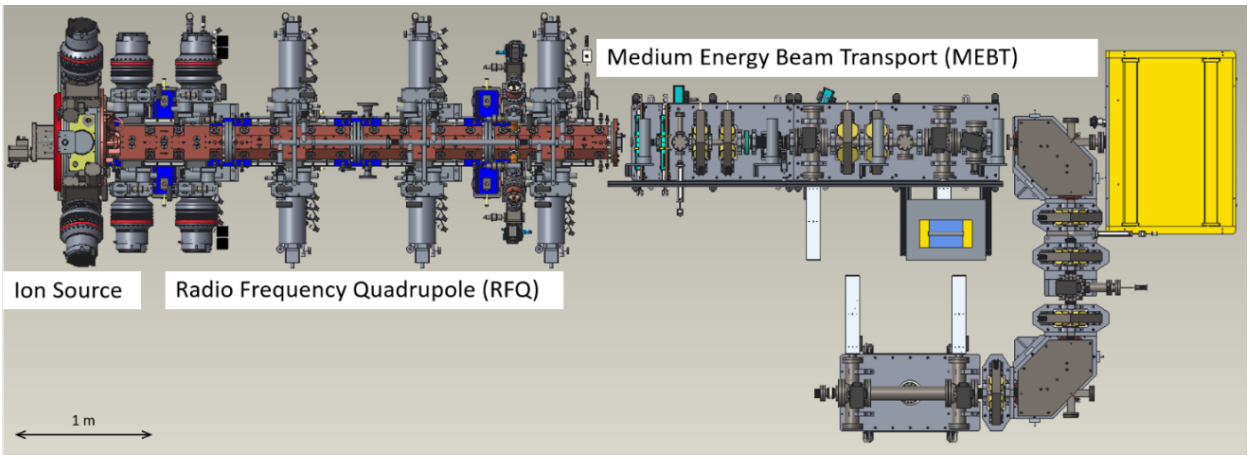

Figure 3.1: A schematic of the Beam Test Facility (BTF).

The BTF produces a pulsed 2.5 MeV ion beam with a peak current of up to 50 mA, pulse width of 50 μs, and repetition rate up to 10 Hz when using the beam line diagnostics. The beam is made from H^- ions, just like the SNS linac. A useful parameter to characterize a beam is the RMS emittance, which should not to be confused with the subspaces called emittances described previously. The RMS emittance gives an idea of the area a beam fills in a conjugate pair phase space. It is defined as:

$$\epsilon = \sqrt{\langle x^2 \rangle \langle x'^2 \rangle - \langle x x' \rangle^2} \tag{3.1}$$

where (x, x') are any of the three conjugate position/momentum pairs. For the BTF beam, the typical transverse rms emittance is 0.4 mm $\cdot$ mrad; the longitudinal emittance is approximately 0.25 MeV $\cdot$ deg at 402.5 MHz.

3.1.1 The Front-End

Together, the ion source and RFQ make up the front-end of the BTF. The H^- beam is produced in the ion source before going through the Low Energy Beam Transfer, or LEBT. The schematic for these can be seen in Figure 3.2. Hydrogen gas is pumped into the source and converted to plasma by the RF antenna. The filter magnets use a transverse magnetic field to only allow cool plasma out of the source and into the Cesium collar. Cesium is used because its low work function allows for electrons to be easily given to the Hydrogen ions to form H^-. The slight angle shown in the figure is to correct the beam path after electron dumping. Magnets are used to keep any electrons from continuing by turning them into the dumping electrodes. The remaining electrodes in the LEBT then accelerate the beam while also focusing the transverse size so that the particles fit into the RFQ.

The primary acceleration in the BTF is performed by the RFQ. The BTF RFQ uses four vanes as the electrodes described in the previous chapter. Klystrons provide the necessary energy to allow the vanes to alternate charge at 402.5 MHz. This is the frequency to which the longitudinal particle phase is referenced. Ridges on the vanes create the micro-bunches which are accelerated. As particles need to fit within a time gap on the order of nanoseconds to accelerate with a frequency of 402.5 MHz, the longitudinal phase needs to be measured

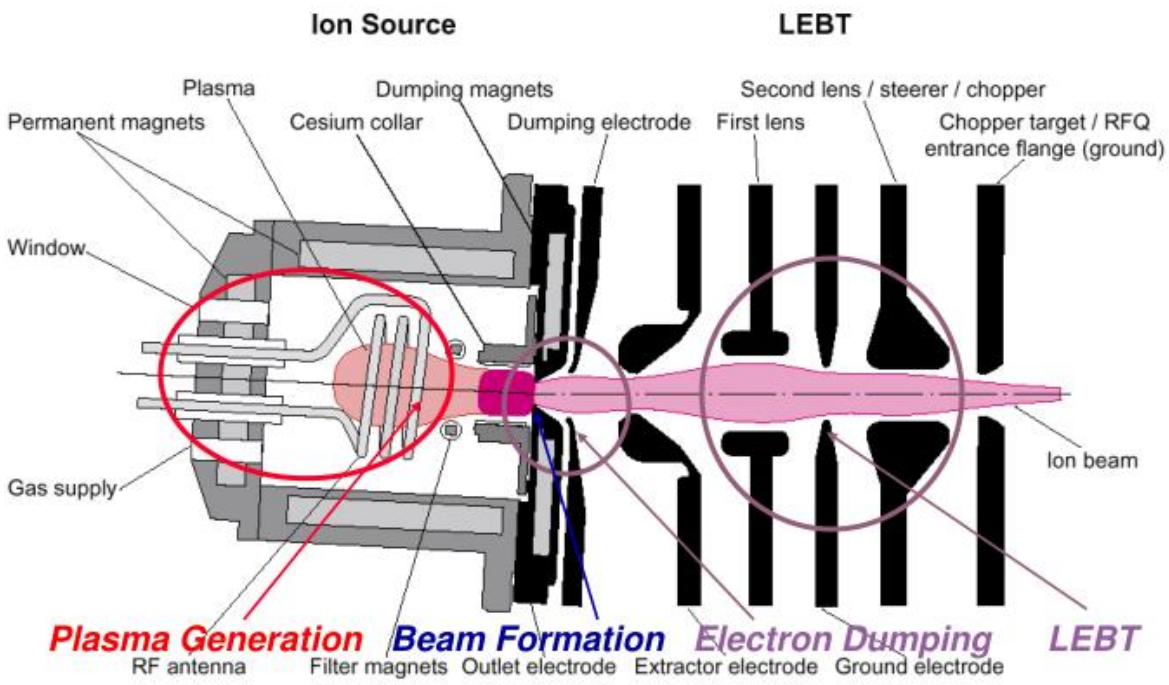

Figure 3.2: Ion source and LEBT schematic..

on the order of degrees. After leaving the RFQ, the beam has reached an energy of 2.5 MeV. Figure 3.3 is a view looking down the inside of the SNS RFQ.

The ion source and RFQ work together to create the longitudinal time structure of the ion beam. There are two components to the time structure. At the smallest level, the RFQ micro-bunching is always on with a period of 2.4845 ns. On top of that is the beam repetition rate, controlled by turning the plasma on and off, creating macro-bunches. The ion source produces particles in intervals from 50 μs to 1 ms at either 1 Hz, 2 Hz, 5 Hz, 10 Hz, or 60 Hz. The 1 ms macro-bunch size at the 60 Hz repetition rate is used to commission new devices for the main SNS beam which need to be tested under production settings. Because the 6D scan diagnostics cannot handle that power, the dimensional measurements were conducted with the lower beam repetition rates with a 50 μs macro-bunch. Figure 3.4 shows the time structure as the RFQ micro-bunching occurs over the ion source macro-bunching. The longitudinal phase distribution that is desired for a 6D scan is the micro-bunch structure. It is assumed that every micro-bunch is the same within and between macro-bunches. Therefore, when a data point is measured, it has been averaged over approximately 20,000 micro-bunches within a measured macro-bunch.

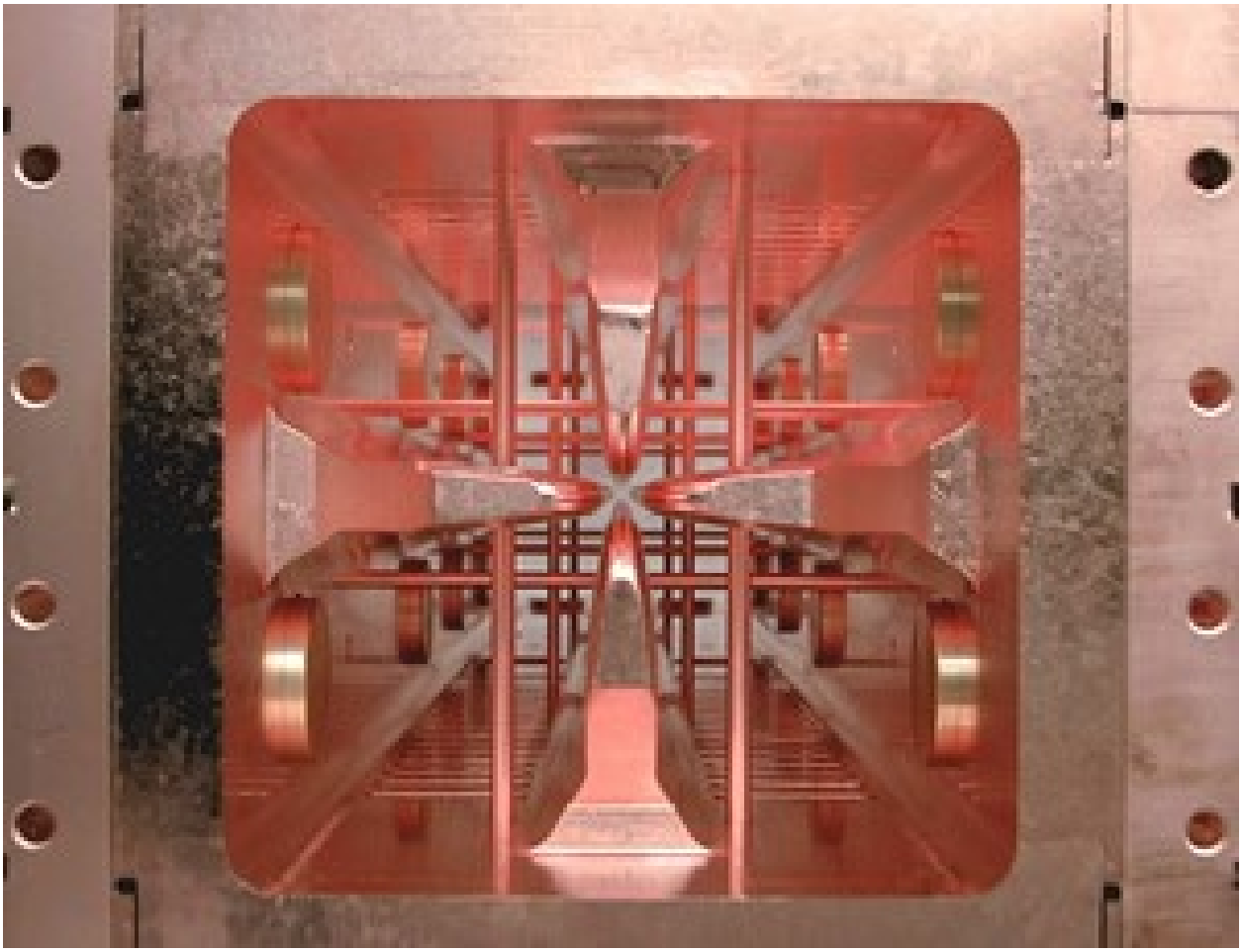

Figure 3.3: The BTF RFQ internal view.

3.1.2 The Medium Energy Beam Transport (MEBT)

Right after the RFQ, the beam is focused by four quadrupoles. The magnets are adjustable in order to focus the beam for measuring elements. Two more quadrupoles are placed between the measuring slits. These quadrupoles are useful for focusing the beam before the bending magnet so that the beam remains within the range of the final instruments. A 90° dipole bending magnet can be turned off to allow the beam to pass straight through or be activated to turn the beam into the rest of the diagnostics. Both paths end with a beam stop. All the magnets have adjustable currents to control the beam. There are two beam stops equipped with Faraday cups used to terminate the beam line. The larger one, shown in yellow in Figure 3.5, is used when running at the 60 Hz repetition rate. A smaller beam stop is used after turing through the bending magnet for the lower beam powers. Figure 3.6 shows the

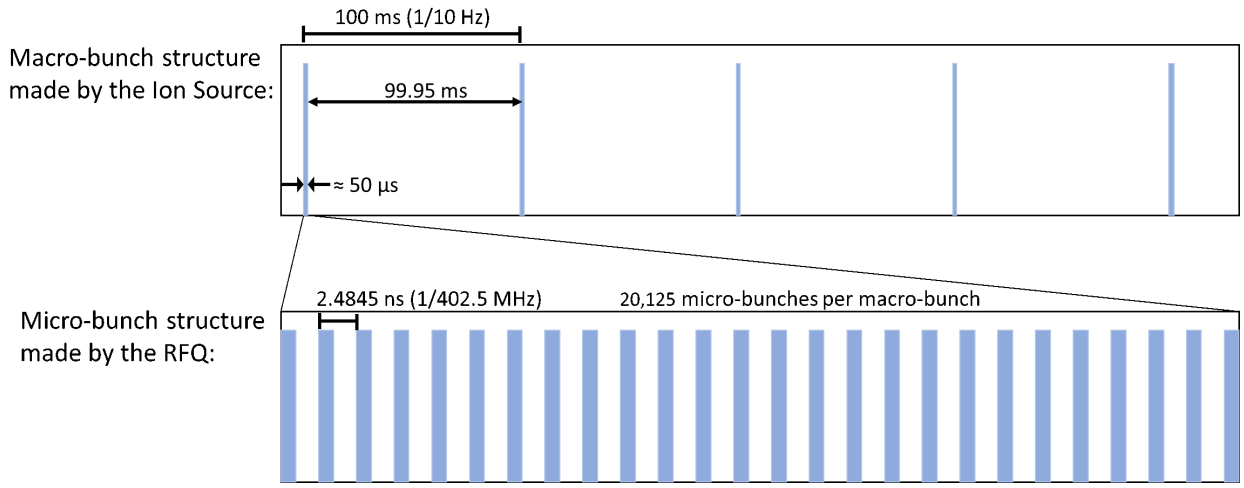

Figure 3.4: Time structure of the BTF beam.

RMS horizontal and vertical sizes of the beam as it progresses through the BTF given by a simulation in the code pyORBIT. The quadrupole and dipole effects on the beam can be seen.

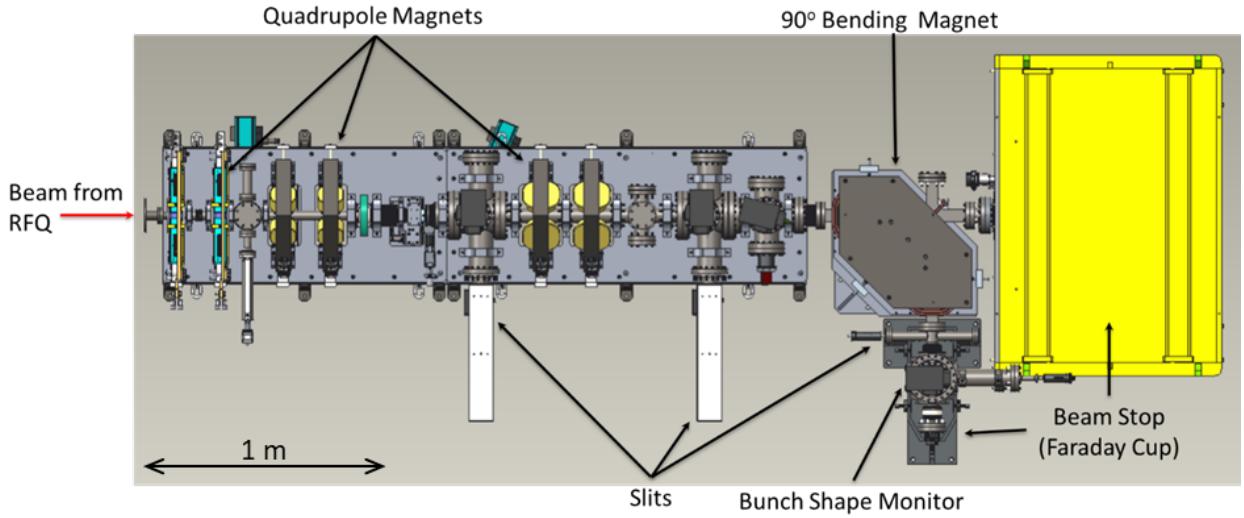

Figure 3.5: Schematic of the BTF MEBT where the diagnostics are located.

The ion source, LEBT, and RFQ are exact replicas of the main SNS beam line. The beam that emerges from the BTF RFQ should be the same beam that emerges from the SNS RFQ. Not only is this useful for testing new equipment before installing in the main machine, but it also means that the measured 6D beam on the BTF is valid for simulations of the main beam.

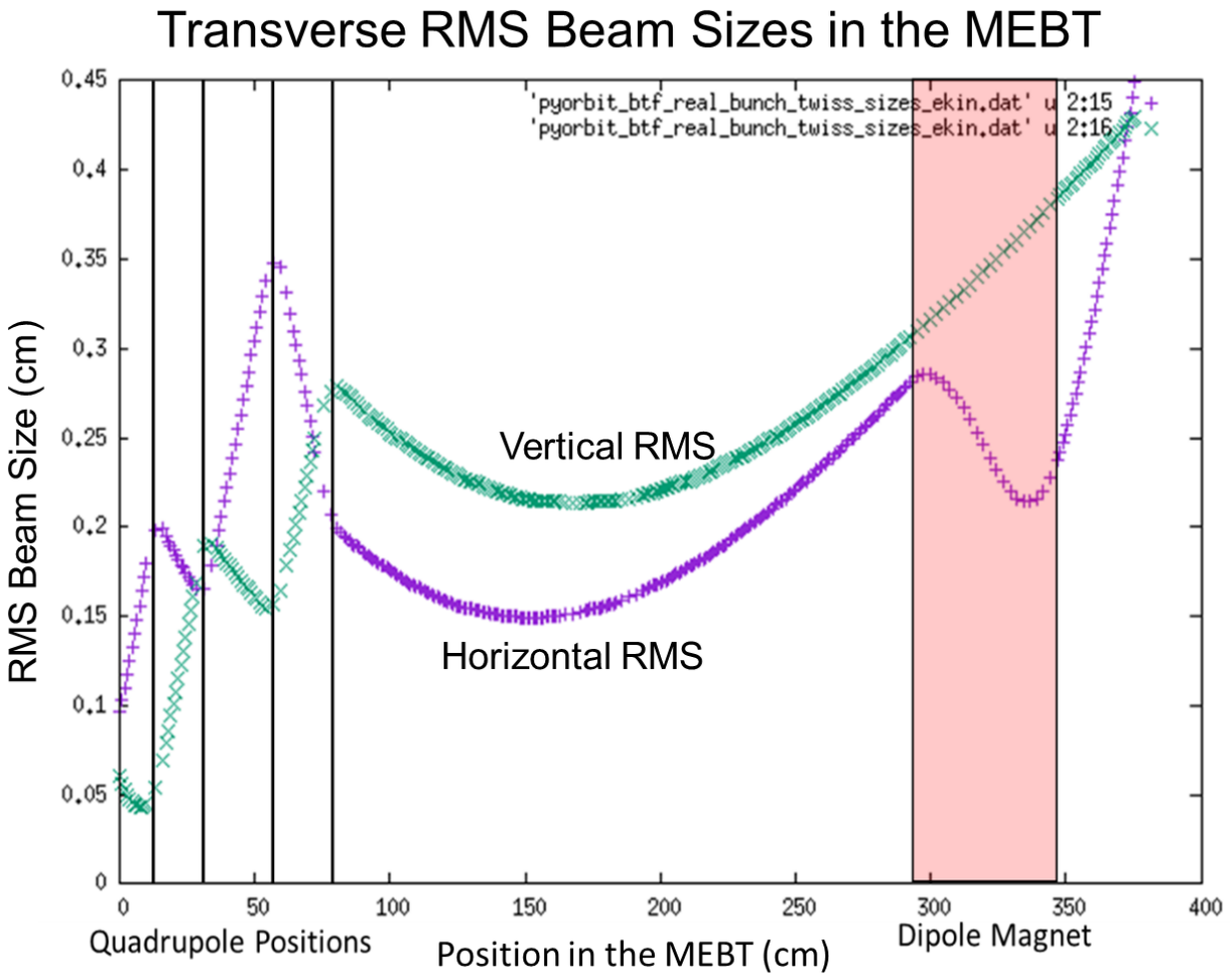

Figure 3.6: RMS transverse beam sizes along the beam line.

3.2 Diagnostics

The technique used here is the same in principle as the aperture technique described in the previous chapter, but for all six dimensions simultaneously. See Figure 3.7 for a schematic of the principle behind the scan and Figure 3.5 for the placements of the diagnostics in the beam line. The particles go through a series of five apertures, or slits. Each aperture will allow particles through at the coordinate being measured. The first four apertures, each 200 μm wide, measure the transverse four-dimensional distribution. They can be seen in Figure 3.8. These slits use the standard double slit emittance measuring technique previously described, but by combining the two pairs of apertures—one pair of horizontal slits and another pair of vertical slits—the full 4D transverse phase space can be measured (Figure

3.9). The transverse slit pairs are 0.947 m apart along the beam line. These slits are motorized with actuators, allowing their movements to be programed during the scan. The actuators were accurate to 0.02 mm. The first two slits measure the (x, y) subspace. The transverse momentum is measured as the angle from the synchronous particle. Using the small angle approximation, the momenta can be found by taking the difference between the slits transverse positions and dividing by the distance between them:

$$x' = \frac{x_2 - x}{L}, y' = \frac{y_2 - y}{L} \tag{3.2}$$

where L is 0.94 m.

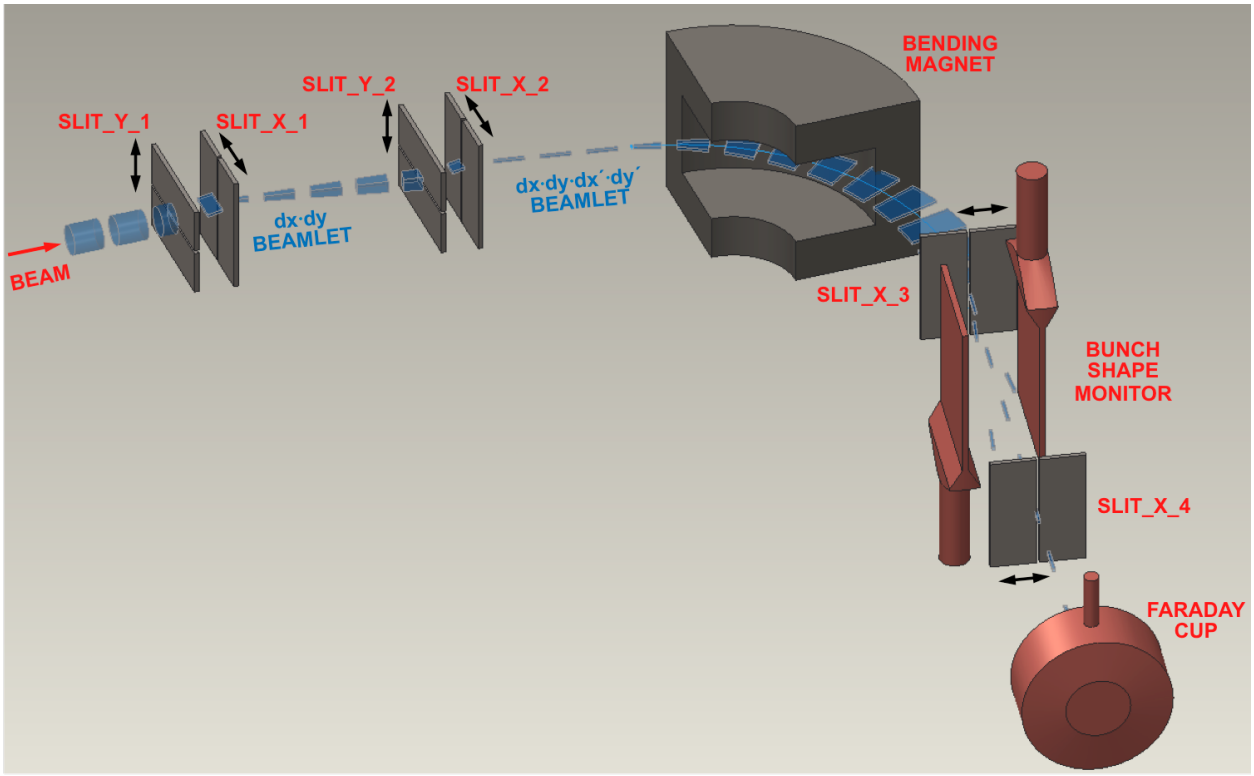

Figure 3.7: A diagram showing the principle behind a full six-dimensional emittance scan. Secondary electrons from the BSM are not shown.

3.2.1 Energy Selection

To find the longitudinal momentum, the 90° bending magnet is used. During the turn, the beam spreads as higher momentum and lower momentum particles separate horizontally.

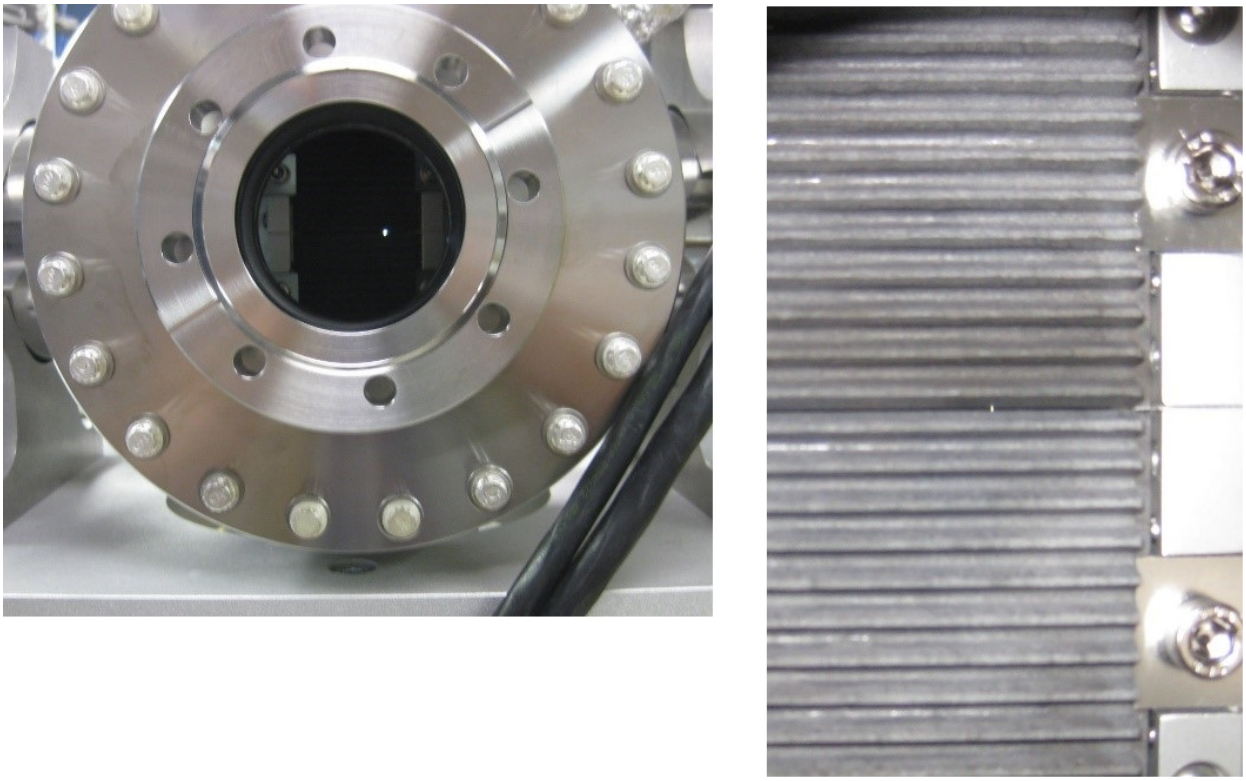

Figure 3.8: Picture of a transverse graphite slits.

This effect, called dispersion, allows the selection of particles with certain momentum based on their horizontal position, which is executed using a third movable 800 μm wide vertical slit: the fifth slit. To calculate the energy of a particle, we need the (x, x') at a point before the bending magnet, and the particles horizontal position after the magnet. Because of the previous vertical slits, we know the (x, x) value and the energy slit gives the final position. We then use the matrices from the previous chapter to calculate the energy along with the matrix for particles moving freely down the beamline, the drift matrix:

$$\begin{bmatrix} x \\ x' \\ \lambda \\ \frac{\Delta P}{P_s} \end{bmatrix} = \begin{bmatrix} 1 & L & 0 & 0 \\ 0 & 1 & 0 & 0 \\ 0 & 0 & 1 & 0 \\ 0 & 0 & 0 & 1 \end{bmatrix} \begin{bmatrix} x_0 \\ x'_0 \\ \lambda_0 \\ \frac{\Delta P_0}{P_s} \end{bmatrix} \tag{3.3}$$

This matrix makes intuitive sense: without external forces, the horizontal and longitudinal momentum will not change, which means the path length will not change either.

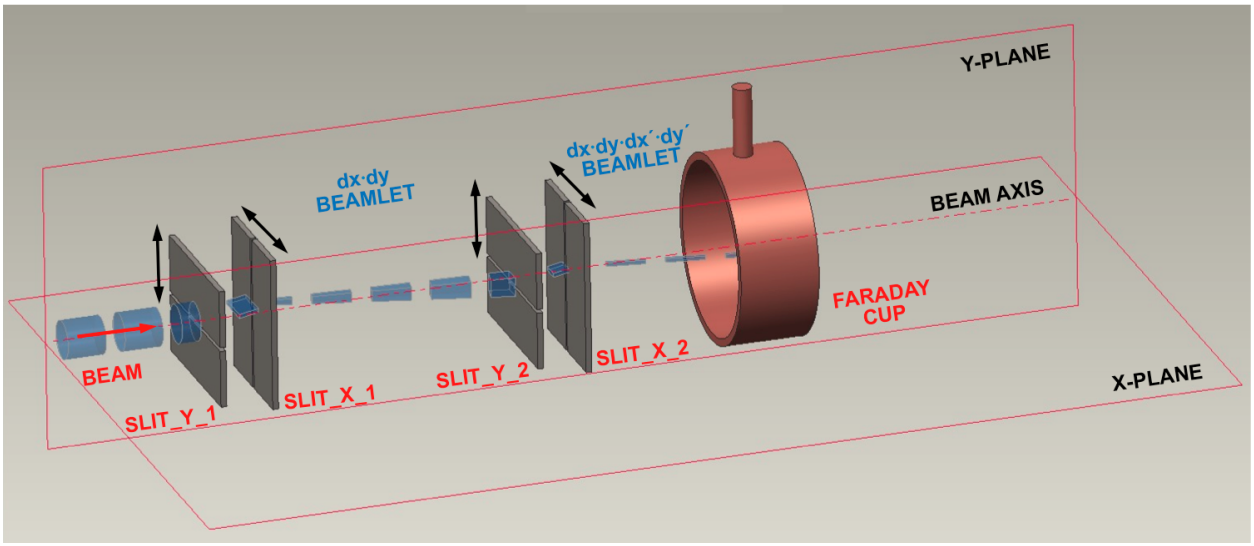

Figure 3.9: A diagram showing the principle behind a four-dimensional scan over the transverse plane.

Because $x' = \frac{\mathrm{d}x}{\mathrm{d}s}$, the new x value will be x' multiplied by the drift distance, L. This is also the matrix reached if the limit is taken as K goes to 0 in the quadrupole matrix from the previous chapter. To find the transformation matrix for multiple elements, the matrices are multiplied in order of their appearance so that:

$$\begin{bmatrix} x \\ x' \\ \lambda \\ \frac{\Delta P}{P_s} \end{bmatrix} = M_4 M_3 M_2 M_1 \begin{bmatrix} x_0 \\ x'_0 \\ \lambda_0 \\ \frac{\Delta P_0}{P_s} \end{bmatrix} = M_{1\to 4} \begin{bmatrix} x_0 \\ x'_0 \\ \lambda_0 \\ \frac{\Delta P_0}{P_s} \end{bmatrix} \tag{3.4}$$

For the measurement, the quadrupoles between the first pair of slits were not used, so our matrices are the drift between first slits and the dipole ($L = 1.530\,\mathrm{m}$), the dipole magnet ($\rho = 0.3556\,\mathrm{m}$), and the drift to the final slit ($l = 0.304\,\mathrm{m}$). Multiplying these matrices gives:

$$M_{l,\rho,L} = M_l M_\rho M_L = \begin{bmatrix} 1 & l & 0 & 0 \\ 0 & 1 & 0 & 0 \\ 0 & 0 & 1 & 0 \\ 0 & 0 & 0 & 1 \end{bmatrix} \begin{bmatrix} 0 & \rho & 0 & \rho \\ -\frac{1}{\rho} & 0 & 0 & 1 \\ 1 & \rho & 1 & \rho\left(\frac{\pi}{2} - 1\right) \\ 0 & 0 & 0 & 1 \end{bmatrix} \begin{bmatrix} 1 & L & 0 & 0 \\ 0 & 1 & 0 & 0 \\ 0 & 0 & 1 & 0 \\ 0 & 0 & 0 & 1 \end{bmatrix} \tag{3.5}$$

$$M_{l,\rho,L} = \begin{bmatrix} 1 & l & 0 & 0 \\ 0 & 1 & 0 & 0 \\ 0 & 0 & 1 & 0 \\ 0 & 0 & 0 & 1 \end{bmatrix} \begin{bmatrix} 0 & \rho & 0 & \rho \\ -\frac{1}{\rho} & -\frac{L}{\rho} & 0 & 1 \\ 1 & L+\rho & 1 & \rho\left(\frac{\pi}{2}-1\right) \\ 0 & 0 & 0 & 1 \end{bmatrix} \tag{3.6}$$

$$M_{l,\rho,L} = \begin{bmatrix} -\frac{l}{\rho} & \rho - \frac{Ll}{\rho} & 0 & l+\rho \\ -\frac{1}{\rho} & -\frac{L}{\rho} & 0 & 1 \\ 1 & L+\rho & 1 & \rho\left(\frac{\pi}{2}-1\right) \\ 0 & 0 & 0 & 1 \end{bmatrix} \tag{3.7}$$

We then have that:

$$\begin{bmatrix} x \\ x' \\ \lambda \\ \frac{\Delta P}{P_s} \end{bmatrix} = M_{l,\rho,L} \begin{bmatrix} x_0 \\ x_0' \\ \lambda_0 \\ \frac{\Delta P_0}{P_s} \end{bmatrix} = \begin{bmatrix} -\frac{l}{\rho} & \rho - \frac{Ll}{\rho} & 0 & l+\rho \\ -\frac{1}{\rho} & -\frac{L}{\rho} & 0 & 1 \\ 1 & L+\rho & 1 & \rho\left(\frac{\pi}{2}-1\right) \\ 0 & 0 & 0 & 1 \end{bmatrix} \begin{bmatrix} x_0 \\ x_0' \\ \lambda_0 \\ \frac{\Delta P_0}{P_s} \end{bmatrix} \tag{3.8}$$

Considering the equation for x gives:

$$x = -\frac{l}{\rho}x_0 + \left(\rho - \frac{Ll}{\rho}\right)x_0' + (l+\rho)\frac{\Delta P_0}{P_s} \tag{3.9}$$

P, the momentum of a particle, can be found by:

$$x = -\frac{l}{\rho}x_0 + \left(\rho - \frac{Ll}{\rho}\right)x_0' + (l+\rho)\frac{P - P_s}{P_s} \tag{3.10}$$

$$(l+\rho)\frac{P - P_s}{P_s} = x + \frac{l}{\rho}x_0 - \left(\rho - \frac{Ll}{\rho}\right)x_0' \tag{3.11}$$

$$P = \left(\frac{x + \frac{l}{\rho}x_0 - \left(\rho - \frac{Ll}{\rho}\right)x_0'}{l+\rho} + 1\right)P_s \tag{3.12}$$

$$P = D(x_0, x_0', x)P_s \tag{3.13}$$

This gives the momentum of a particle as a function of the (x, x') value of the particle and its position x at the energy slit. The relativistic γ_s for a proton with a kinetic energy of $E_s = 2.5$ MeV is:

$$\gamma_s = \left(\frac{E_s}{m_0} + 1\right) = 1.0027 \tag{3.14}$$

which gives a β_s of:

$$\beta_s = \sqrt{1 - \frac{1}{{\gamma_s}^2}} = 0.073 \tag{3.15}$$

The error for not using relativistic energy is given by:

$$\frac{(\gamma_s - 1)m_0 - \frac{1}{2}m_0{\beta_s}^2}{(\gamma_s - 1)m_0} = 0.01\,\text{MeV} \tag{3.16}$$

Because the energy deviation in the distribution is about $\pm 0.05\,\text{MeV}$, a relativistic treatment is necessary. The kinetic energy difference is then calculated by:

$$w = \Delta E = E - E_s \tag{3.17}$$

Putting this in terms of the total energy, E_T, yields:

$$w = E_T - m_0 - E_s \tag{3.18}$$

$$w = \sqrt{P^2 + {m_0}^2} - m_0 - E_s \tag{3.19}$$

$$w = \sqrt{(DP_s)^2 + {m_0}^2} - m_0 - E_s \tag{3.20}$$

$$w(x_0, x_0', x) = \sqrt{D^2(x_0, x_0', x)((E_s + m_0)^2 - {m_0}^2) + {m_0}^2} - m_0 - E_s \tag{3.21}$$

Therefore, for any measurement of (x_0, x_0', x), the energy difference w can be found.

A difference from the initial concept illustrated above was that the energy slit, shown in Figure 3.10, moves manually: it is not on a programmable actuator. Therefore, instead of moving this slit, the slit was positioned in the beam path and the dipole magnet current was changed. This changed the energy selected by the slit without needing to move the slit. This slit also doubles as one of two screens which could measure the charge in addition to a Faraday cup. This allowed for an entire dimension to be measured at once. However, because using a screen blocks the beam, the energy screen could not be used for a full six-dimensional scan as the longitudinal component had not been measured at that point. A camera was used to record the screen luminescence, whose capture was synched to be beam frequency so that each image was the result of a singular macro-bunch. By looking at the slit in the energy screen, the horizontal pixel size on the camera was determined to be 0.079 mm wide.

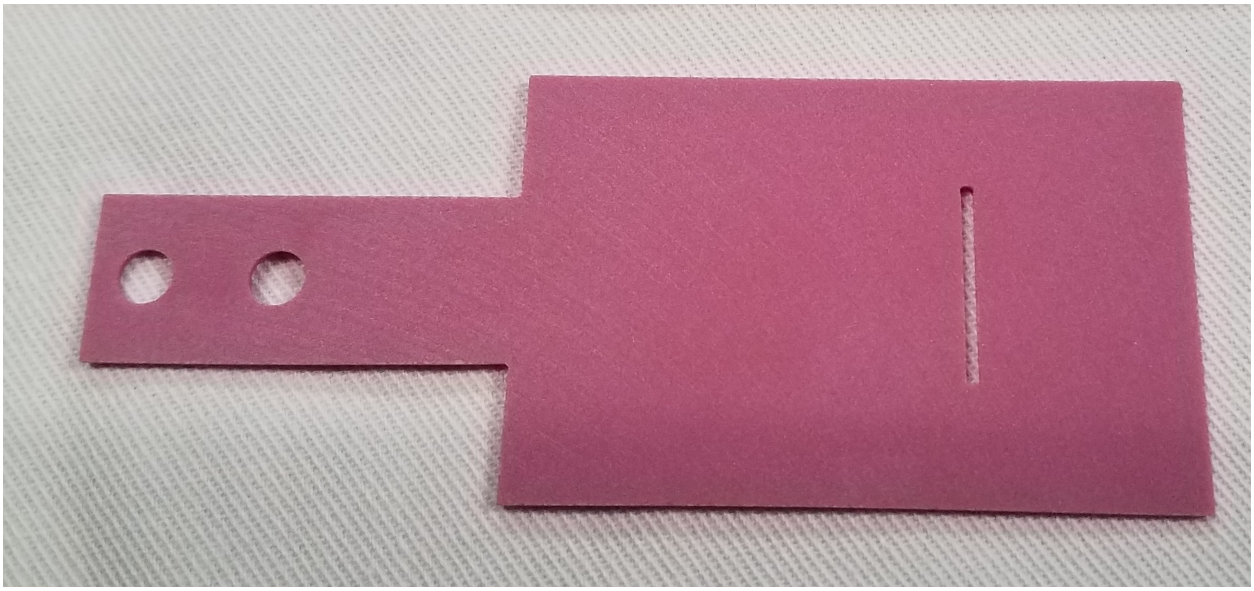

Figure 3.10: The Energy (fifth) slit that also doubled as a scintillating screen. It is made of ceramic with a 800 μm wide slit. Scintillation occurs using chromium.

3.2.2 The Bunch Shape Monitor (BSM)

The final dimension, the longitudinal phase, was measured using a Bunch Shape Monitor (BSM) [26]. The BSM contains a suspended wire with a -10 kV potential in the beam pipe. When the hadron beam hits the wire, secondary electrons are emitted and repelled from the wire due to the potential on the wire. After passing through an aperture to leave the

beam pipe, a deflector, which creates an RF electric field, easily changes the trajectory of the electrons. See Figure 3.11. Electrons will be transversely deflected based on when they so that electrons emitted due to particles early in the beam will be deflected differently than electrons emitted by particles further back. By changing the phase of the electric field, electrons from a chosen longitudinal position in the beam will be not be deflected when they arrive. These electrons then hit a Faraday cup and are measured as current. Electrons are used because protons are much harder to deflect with the RF field.

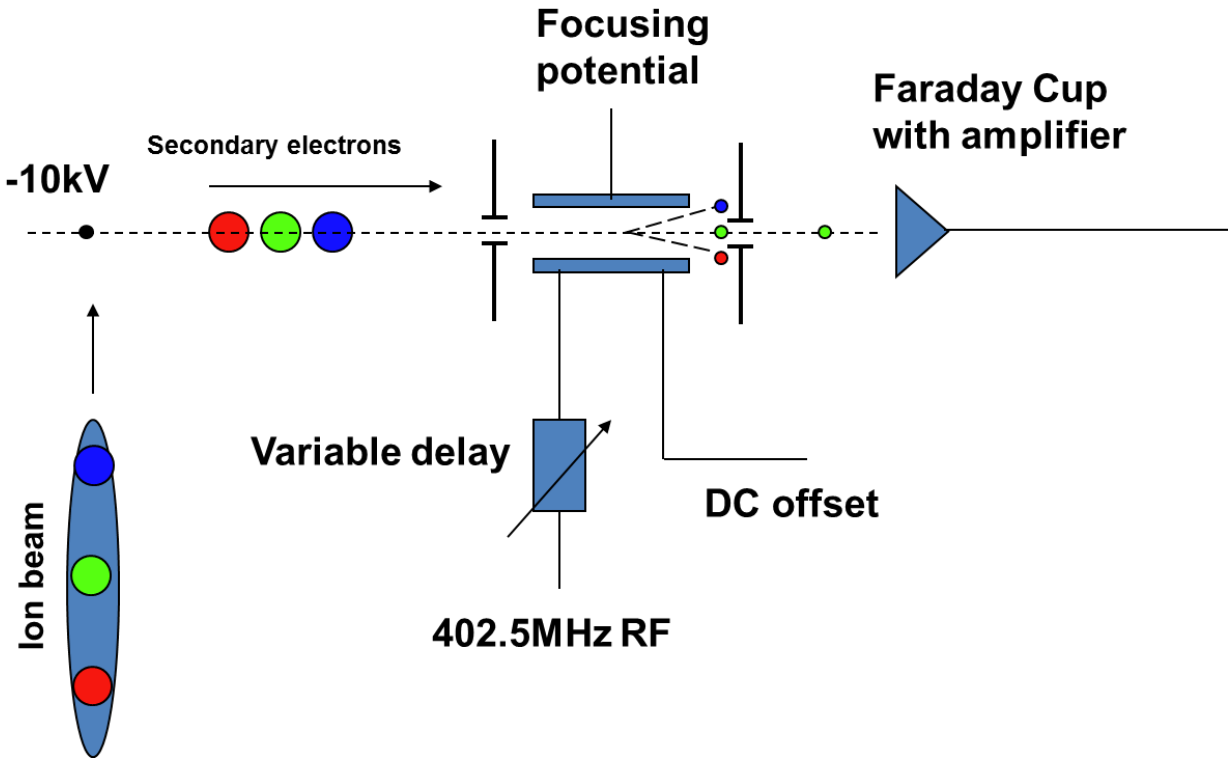

Figure 3.11: A diagram of the basic plan behind the BSM for measuring the arrival time of hadrons in the beam.

The resolution of the BSM is about 1° of the 402.5 MHz. The BSM used a LabVIEW program that was previously coded. Calibration of the beam phase based on the RF deflector phase was a simple matter of making sure the signal repeats at exactly 360°. The application worked by running through a set of phases and saving the signal at each phase. While this is convenient for taking singular scans, it was necessary to modify the application to allow for the RF deflector phase to be changed by external input and not proceed through a scan on its own.

The second scintillating screen replaced the aperture and Faraday cup after the deflector inside the BSM. As the BSM was the last component in a full six-dimensional measurement, this screen was the primary method for using the BSM after its installation, including the final 6D measurement. Because many particles are removed with each slit, the signal strength for the BSM screen was quite low. As such, a micro-channel plate (MCP) was used to increase the signal strength for the BSM screen.

A consequence of including no longitudinal control elements in the MEBT is that each bunch expands longitudinally due to the energy spread until particles from subsequent bunches overlap. However, this was not an issue due to the multidimensional nature of the scans. Using the bending magnet, each bunch will be separated for phase measurement as particles with higher energy will have a greater radius in their trajectory than particles with lower energy. Simulations looking at the (ϕ, x) subspace after the bending magnet indicate that successive bunches will not overlap and hinder data collection (Figure 3.12).

A final change to the initial concept was using the BSM wire for the second vertical position measurement. Electrons for the RF deflector are only emitted for protons that hit the wire. If the second vertical slit was used, it would be necessary to code the wire to follow the beam as both vertical slits affect the position of particles that reach the wire. Instead, because the wire uses the same actuators as the slits, its position is just as accurate and is synced with the other recording devices. A slight concern was that the bending magnet might interfere with measuring y'. The effect of the bending magnet on vertical position was tested by comparing the y' distribution measured with the energy screen against the distribution measured with the two vertical slits before the dipole. Figure 3.13 shows the results indicating the bending magnet had no effect.

3.3 Scan Organization

Specialized scripts based on an Open XAL framework were developed and used to perform the scans [27]. The BTF hardware used LabVIEW for control and EPICs to communicate between the LabVIEW code and the scripts running dimensionality scans. Java was used to coordinate the hardware and run scans. Because scans could run longer than a day,

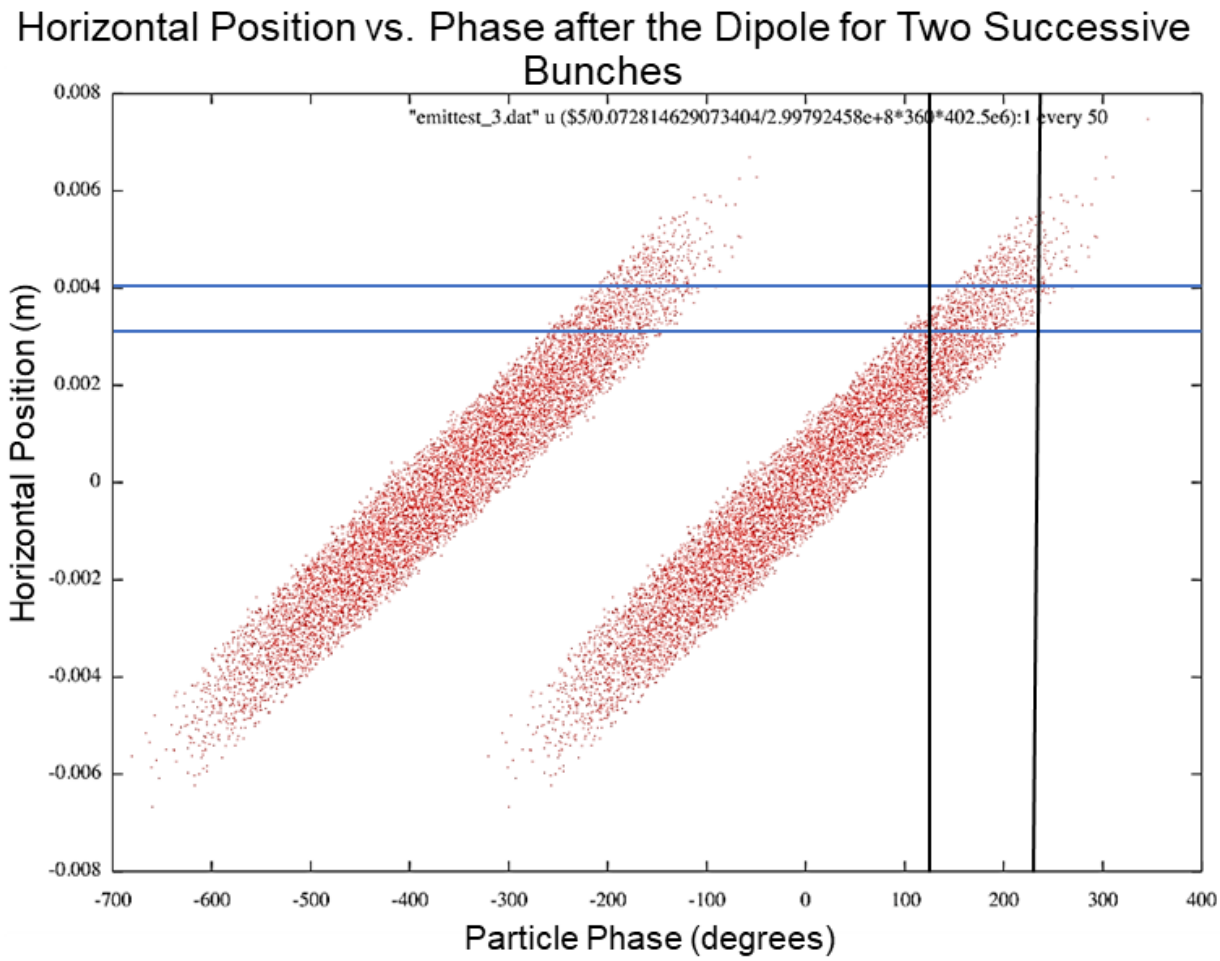

Figure 3.12: Simulation showing separation of subsequent bunches after the bending magnet. The blue lines show the gap in the energy slit and the black lines show the phase selection.

automation was necessary. To cover the full phase space, the scan needed each parameter selector to move one at a time. The term selector is used here to represent the slits, dipole, and wire that select which coordinate in the phase space is being measured at that moment. For a systematic scan, a hierarchy is needed where one selector almost constantly moves and each subsequent selector after that moves less and less. Figure 3.14 shows the 6D scan scheme. The first slit in the beam path, the horizontal position selector or x slit, received the most energy from the beam. To protect this slit, it was kept in constant motion which distributed the energy over its surface. After the x selector finished a sweep, the y selector would move a step, and the x selector would sweep backwards to minimize scan time. Once the y selector covered its path, the x' slit would take a step and the y slit would begin traveling backwards

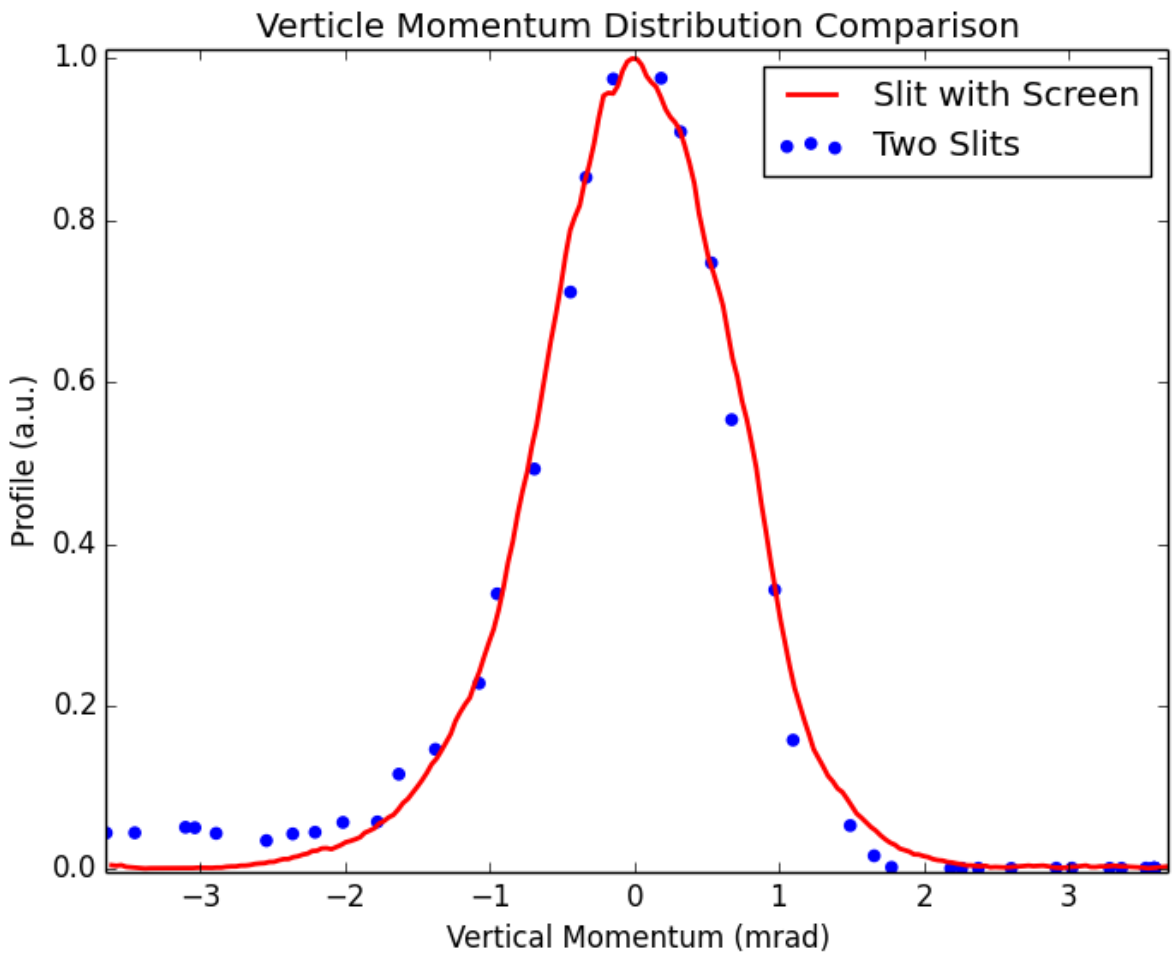

Figure 3.13: Comparison of measuring y' before and after the dipole magnet.

and the same pattern would continue. Eventually, all four selectors covered the transverse phase space. This is sufficient for a four-dimensional transverse scan, or a five-dimensional scan that measures the energy using the energy screen. When used, the bending magnet current would be the last detector. Because the current read-back was not triggered by the beam like the previous selectors, the scan needed to wait to make sure the dipole current finished changing before continuing. Therefore, the dipole needed to change its selection the least to minimize the scan time. This also helps with hysteresis effects between the current and magnetic field as the last selector only travels in one direction, so the dipole current either only increases or decreases for the duration of a scan. For the six-dimensional scan, once a transverse phase space was measured, the dipole would change, and the transverse

space was measured again. A sixth selector was not needed for the final six-dimensional scan as the particle phase was measured using the screen in the BSM described previously.

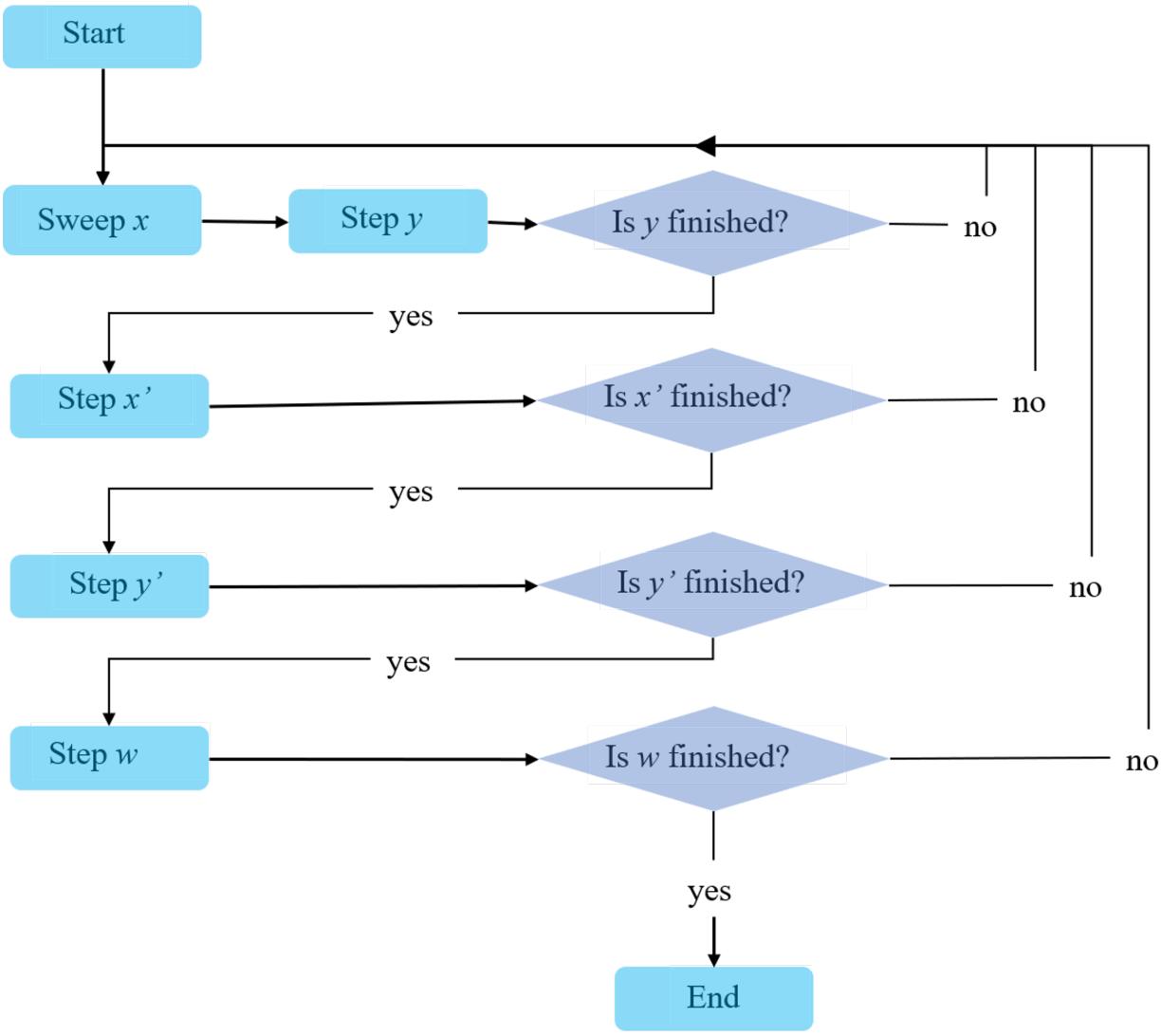

Figure 3.14: Diagram showing the logic behind a six-dimensional scan.

While the BSM used a camera to measure the particle phase distribution, the BSM could not cover the entire phase of the bunch. Without any rebunchers in the MEBT, the beam was very long when it reached the BSM. However, because the energy is selected first and strongly correlated to the phase, the phase spread reaching the BSM was small enough to measure (Figure 3.12). Therefore, the BSM central RF phase had to change with the energy to keep the particle distribution in the center of the screen. The x, x', and dipole current all determine the energy of the particles reaching the BSM. Ideally, the position of all three

would be used to keep the electrons as centered as possible, but, like the dipole current, the RF phase read-back was not triggered by the beam. This means that the horizontal actuators would have to step and wait for the central phase to adjust each time. This is particularly troublesome regarding the x selector as it continuously moves during a scan to save time. However, the x selector showed to have a small enough effect on the energy that the central deflector phase was set to only change linearly with the dipole current and x' slit position. The RF amplitude was set to maximize sensitivity but keep the electrons within the screen area.

3.4 Scan Efficiency

Efficiency of the scan time and the amount of data were priorities in development. The biggest improvement to scan time came from using the above described screens. Measuring an entire dimension at one time exponentially decreases scan times. The time was additionally minimized by taking account of the correlations between conjugate spatial and momentum parameters. The x and y selectors cover different displacements depending on x' and y' respectively to ensure time was not wasted on phase space volumes without beam. Figure 3.15 demonstrates the idea. This required the (x, x') and (y, y') subspaces to always be measured before higher dimensional scans to verify the beam was tightly covered. This includes a scan of the $(x, x', w,)$ subspace as well due to the correlation between the selectors of these coordinates as described above. While this increased scan efficiency, it meant the data was now irregularly gridded which would need to be fixed during analysis.

Because the BSM RF deflects only in one dimension, the other dimension could be integrated away to minimize amount of data saved. When using a screen, each configuration of selectors resulted in an array that needed to be saved. In case of a failure, each measurement was saved as it was collected so that an interrupted scan could continue from where it left off. The script was also configured to pause any time the beam current monitor (BCM) upstream of the first slits indicated that the beam had stopped. This kept unnecessary data from taking up space and ensured that parts of the phase space were not skipped.

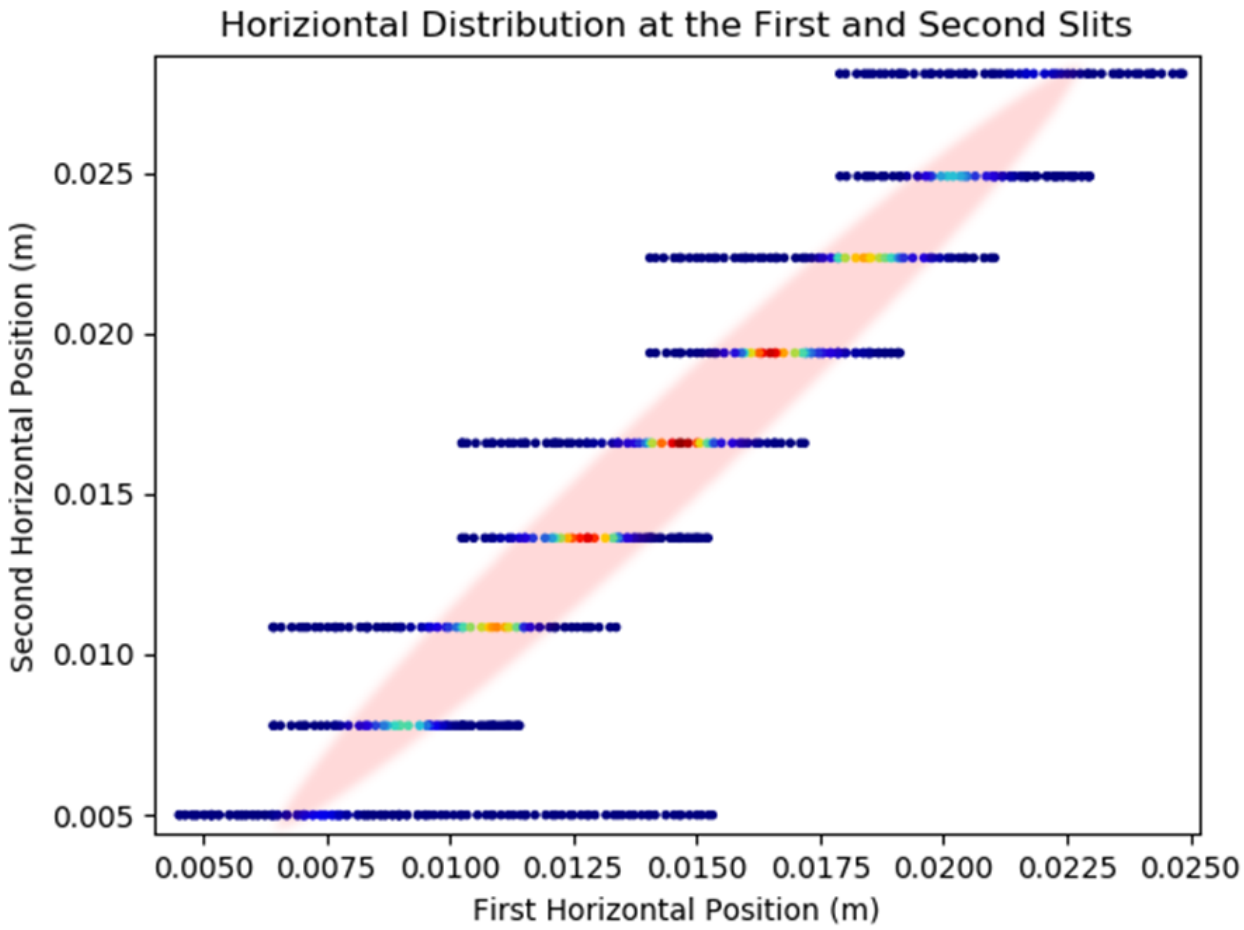

Figure 3.15: An example of efficient scanning in the horizontal phase space. The color represents the measured charge at that point. The red shading is an artificial representation of the true beam area.

The scan repetition rate had an average of only 2.5 Hz for two primary reasons. One reason was the size of the data. During lower dimensional scans, memory size was not an issue. It was only when higher dimensions were reached that the script had trouble saving the data during a scan and needed time to pause. This will be fixed in the future with a more efficient file type to store data. The second reason was the lack of actuator accuracy at faster speeds. When moving, the actuator position read-backs were accurate up to 2.0 mm/s. The limiting factor for the 6D scan was the reliable speed of the x actuator as it was the selector constantly moving.

Chapter 4

Results

4.1 Analyzing the Results

4.1.1 Calibrations

The luminosity of the screens was checked against measurements from a Faraday cup to make sure the relationship between luminosity and charge were linear. Figure 4.1 shows the results that display the linear relationship. As was stated in the previous chapter, the dipole magnet current was used to change which particles traveled through the energy slit. To find the relationship between the current and what the horizontal position of the beam would be which goes through the slit, a graph of the current against the beam center was created and the slope was found. The measurement was taken with the energy screen, which allowed for finding the beam center by averaging the horizontal signal from the camera. Figure 4.2 shows the graph which resulted in a slope of 1.184 mm/A. Calibration for the BSM camera is shown in Figure 4.3. This graph was made by changing the RF deflector phase and measuring the beam center location on the camera like how the energy calibration was made. The resulting slope was 0.39 degrees/pixel.

4.1.2 Interpolation and Distribution Creation

Analyzing high-dimensionality data is complicated. There is no guaranteed method for finding every correlation between an arbitrary number of parameters, but the first obstacle

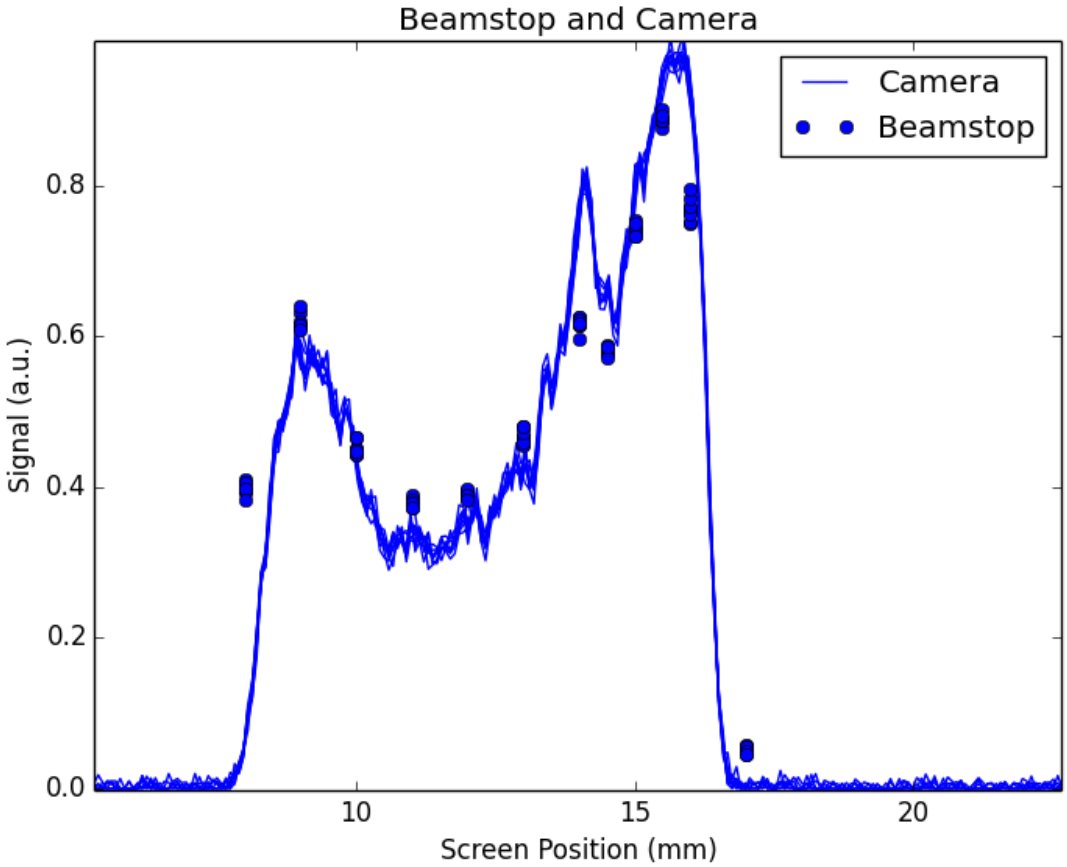

Figure 4.1: Comparison between screen with camera and a Faraday cup.

to finding new correlations is interpolating the measurement. Because the steps for each dimension are sparse and not regularly gridded between dimensions, the data need to be interpolated to a regular 6D grid. This will allow for quick integration over dimensions to view subsets of the data. Custom codes were written to take advantage of how the data were saved. A linear interpolation method is displayed in Figure 4.4 showing how the six-dimensional data set is interpolated. The logic is to interpolate one dimension at a time in the order of how the selectors were iterated, starting with the selector that was constantly moving. For the six-dimensional scan, this means starting by interpolating over the set of x positions for each different set of (y, x', y', w). This is done by interpolating the phase plots point by point linearly to determine the phase plot at new regular x positions. The result is a regular 2D grid of x and ϕ for each set of (y, x', y', w). This technique continues for each

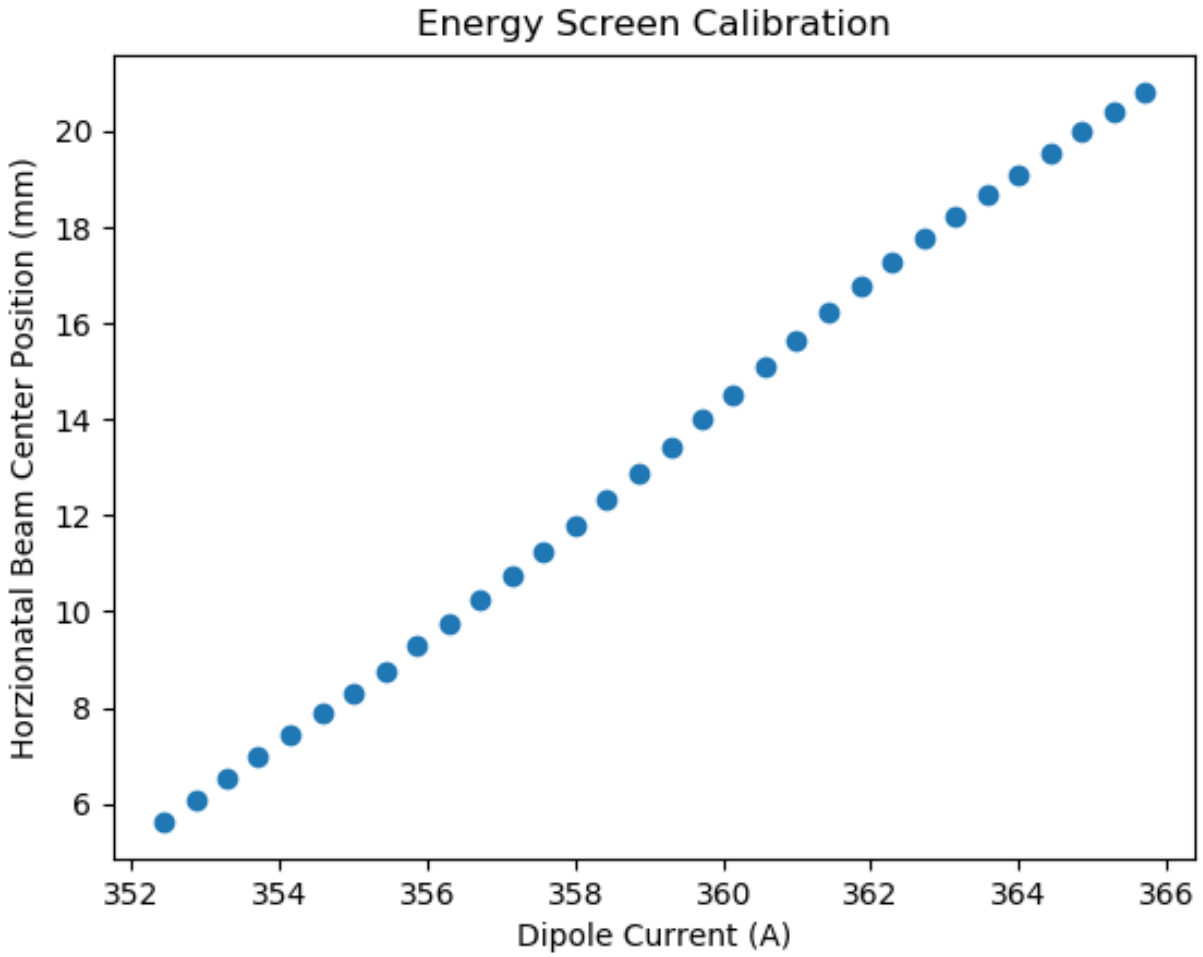

Figure 4.2: Calibration curve to go from dipole current to position on the energy slit.

dimension, interpolating point by point for increasing dimensionalities, using the same order as the scan until a regular 6D space is built.

Because SNS uses particle-in-cell simulation techniques, distributions for simulation contain a list of six-dimensional coordinates of macroparticles. A macroparticle is a representation of a group of particles within the simulation but is treated as physically behaving like a single particle. To generate a distribution of macroparticles, the interpolated six-dimensional array is assigned a number of particles based on its value. Each particle is then given a random displacement from the coordinate to fill in the space between points on the array. Because of the high number of dimensions, large macroparticle counts are needed to preserve structures seen in the raw data. Over a million particles may be necessary.

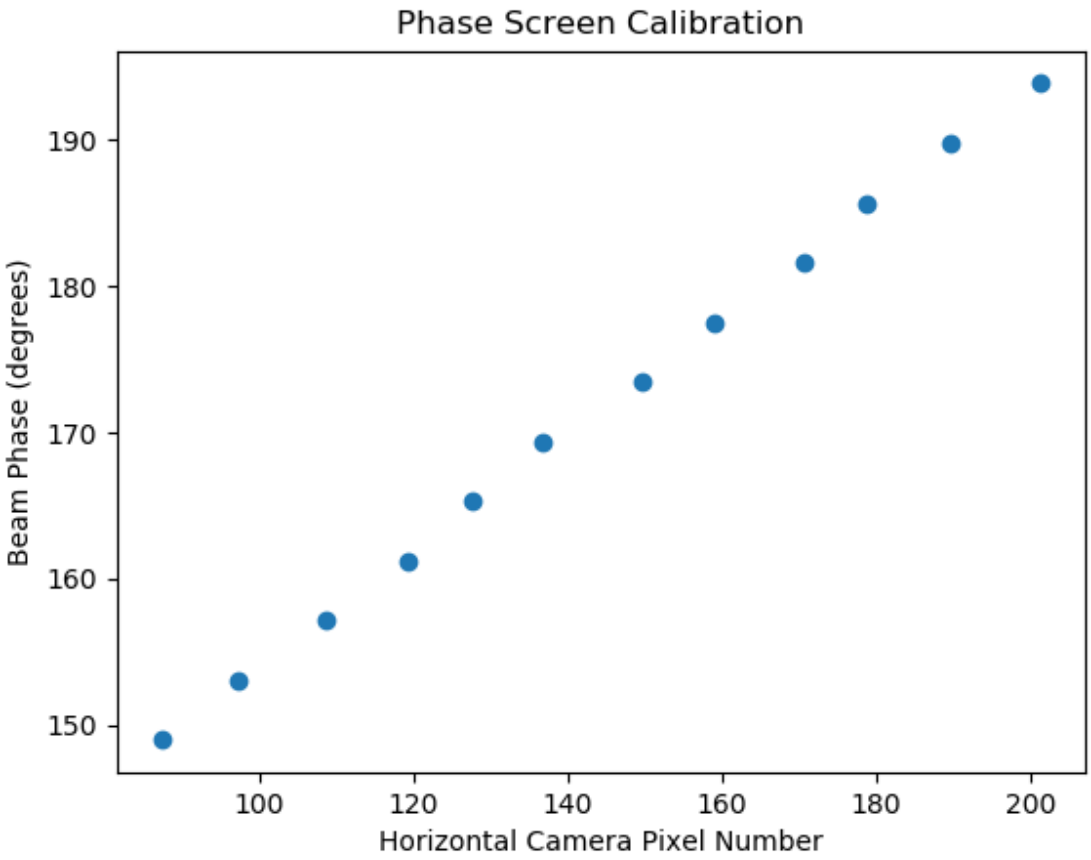

Figure 4.3: Calibration curve for beam phase with the BSM camera.

4.2 Distributions

4.2.1 Projections

Many measurements, including the first full six-dimensional scan, were completed using the technique described above. The six-dimensional scan took 32 hours and resulted in 5,675,740 points in the 6D phase space. In order to visually show possible correlations within the distributions, a method of displaying the high-dimensional results in 2D is needed. This is done through various 1D and 2D projections and partial projections of the higher dimension distributions. The key advantage of using the partial projections is that they avoid integration over all dimensions, which can mask important details of the high dimensionality distribution. The following definitions are used in the data analysis discussion below. Full

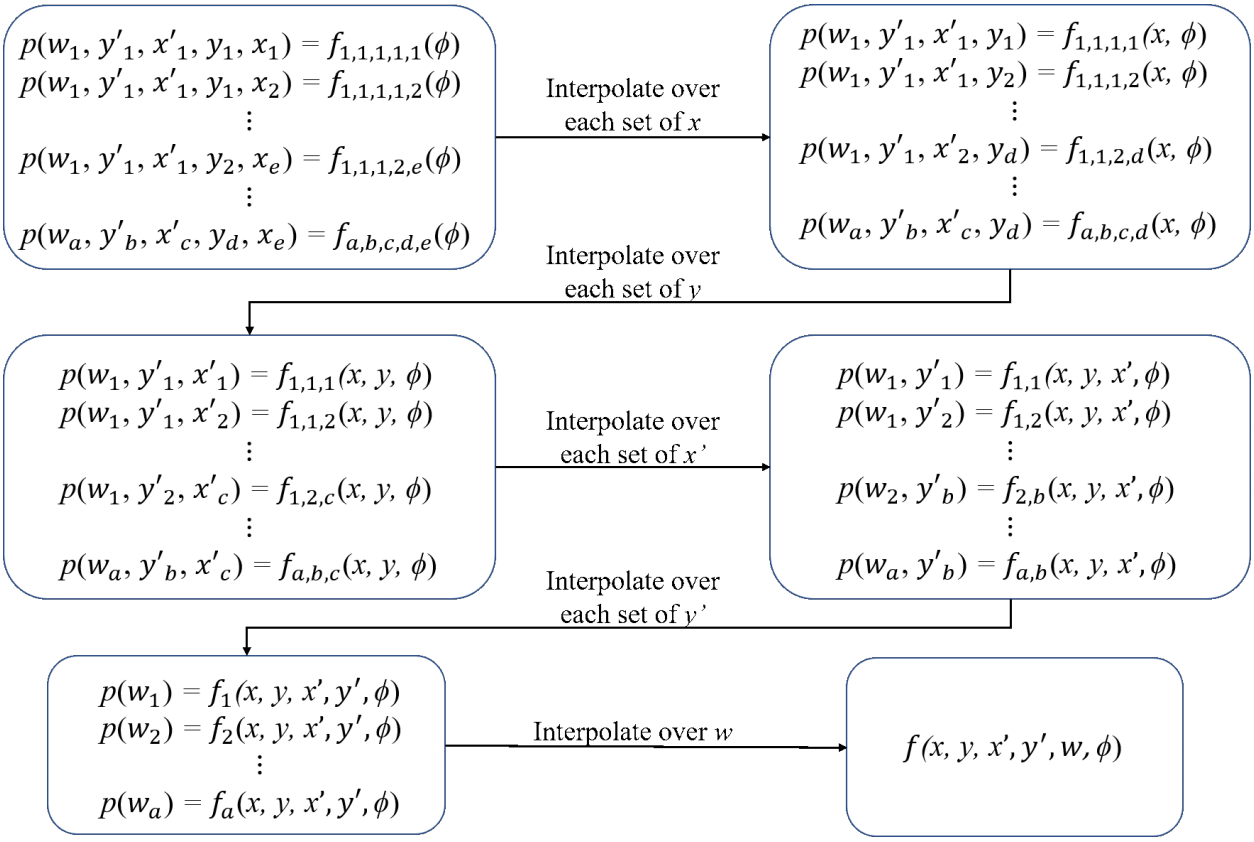

Figure 4.4: The schematic for interpolating the 6D data.

projections are reduced dimensionality distribution functions obtained by integrating over all unused coordinates:

$$1\text{D} : f(a) = \int_{-\infty}^{\infty} f_6(a, \vec{x}) d\vec{x} \tag{4.1}$$

$$2\text{D} : f(a, b) = \int_{-\infty}^{\infty} f_6(a, b, \vec{x}) d\vec{x} \tag{4.2}$$

On the other hand, partial projections are reduced dimensionality distribution functions obtained by fixing select coordinates to constant values and integrating over others:

$$1\text{D} : p(a) = \int_{-\infty}^{\infty} f_6(a, \vec{v} = \vec{v_0}, \vec{x}) d\vec{x} \tag{4.3}$$

$$2\text{D} : p(a, b) = \int_{-\infty}^{\infty} f_6(a, b, \vec{v} = \vec{v_0}, \vec{x}) d\vec{x} \tag{4.4}$$

In the formulas above (a, b) are any coordinates from the (x, x', y, y', w, ϕ) set; $\vec{v}$ is a vector of coordinates remaining in (x, x', y, y', w, ϕ) set after a and b are removed; $\vec{x}$ is the vector of coordinates remaining in (x, x', y, y', w, ϕ) set after a, b, and $\vec{v}$ are removed. Vector $\vec{v}$ is equal to the vector $\vec{v_0}$, which is the fixed coordinate of interest for the partial projection. A partial projection can be measured directly by leaving the selectors responsible for the fixed coordinate $\vec{v_0}$ at fixed positions during a scan. For instance, a partial project of $w = 0$ can be performed directly by fixing the dipole current for that energy and scanning with the remaining dimensions. These scans are much faster than full 6D scans and allow exploring spaces of interest with higher resolution. Multiple scans with different beam parameters can also be done this way in reasonable time durations.

4.2.2 Beam Stability

Measurements throughout the year the BTF was operational remained consistent, including higher dimensional data verified by trusted lower dimensional data. Figure 4.5 shows a one-dimensional scan that used a single slit to measure the horizontal beam distribution and the one-dimensional horizontal axis projection from the transverse four-dimensional scan. Note the agreement is very good. Beam stability was a necessity as 5D scans would last about 5 hours and the 6D scan took 32 hours. Figure 4.6 presents the beam current, measured with a BCM, upstream of the diagnostics during the 6D scan. This shows the BTF produced the necessary stable beam for long scan durations. Finally, Figures 4.7, 4.8, 4.9, and 4.10 are different full projections made from a high resolution 5D scan.

4.3 Uncertainty Analysis

4.3.1 Transverse Uncertainty

Finding the uncertainty for an unknown six-dimensional function is a challenge. We will start by finding the uncertainty in the measurement of each dimension. The four transverse slits are identical with the same widths and movement mechanisms. Each slit is 200 μm which

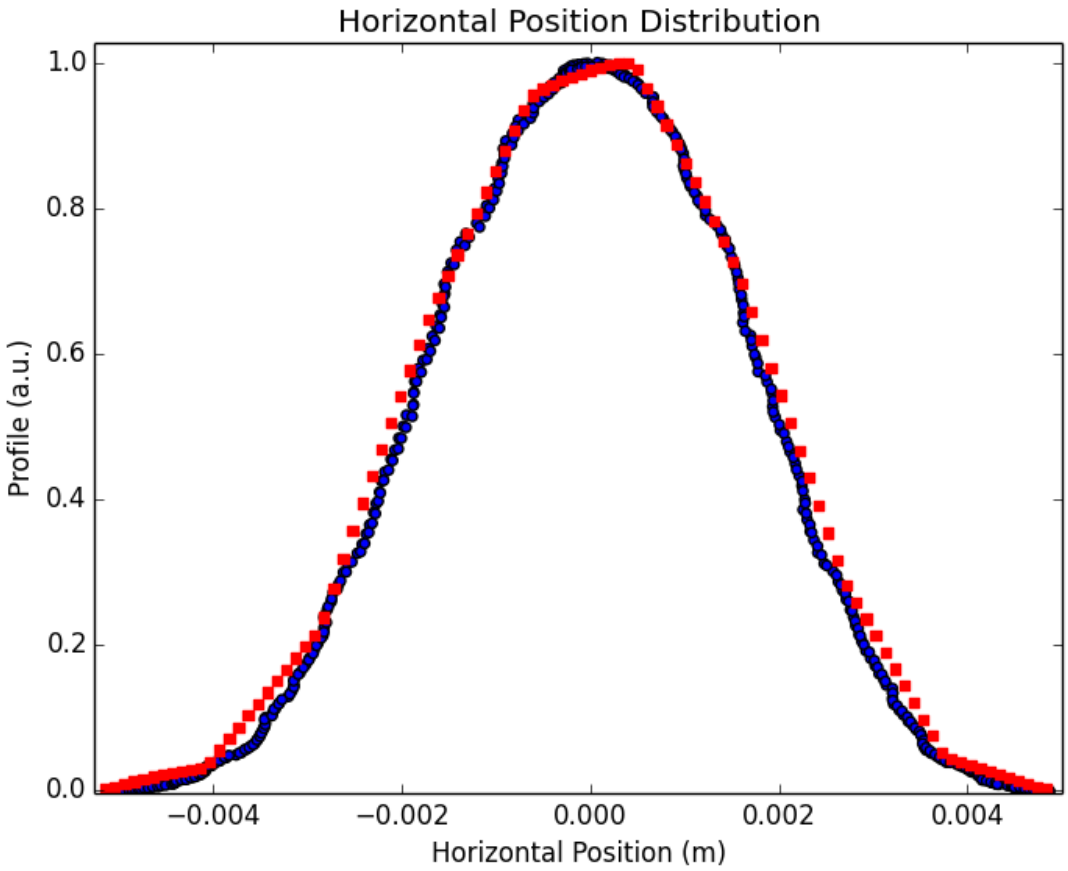

Figure 4.5: Comparison of a one-dimensional scan (blue) and a projection from a four-dimensional scan (red) of the horizontal axis.

gives an uncertainty of $\pm 0.1\,\text{mm}$, and the read-back on the slits position has an uncertainty of about $\pm 0.02\,\text{mm}$. The x and y uncertainties from the first two slits are then:

$$\delta x = \delta y = \pm\sqrt{(0.1\,\text{mm})^2 + (0.02\,\text{mm})^2} \approx \pm 0.1\,\text{mm} \tag{4.5}$$

To find the uncertainty in x' and y', we start with how they are calculated:

$$x' = \frac{x_2 - x}{L_x} \quad \text{and} \quad y' = \frac{y_2 - y}{L_y} \tag{4.6}$$

where x_2, y_2 are the positions of the transverse momentum selectors and L_x, L_y are the distances between the each tranverse selector pair. It is necessary to specify as there are two

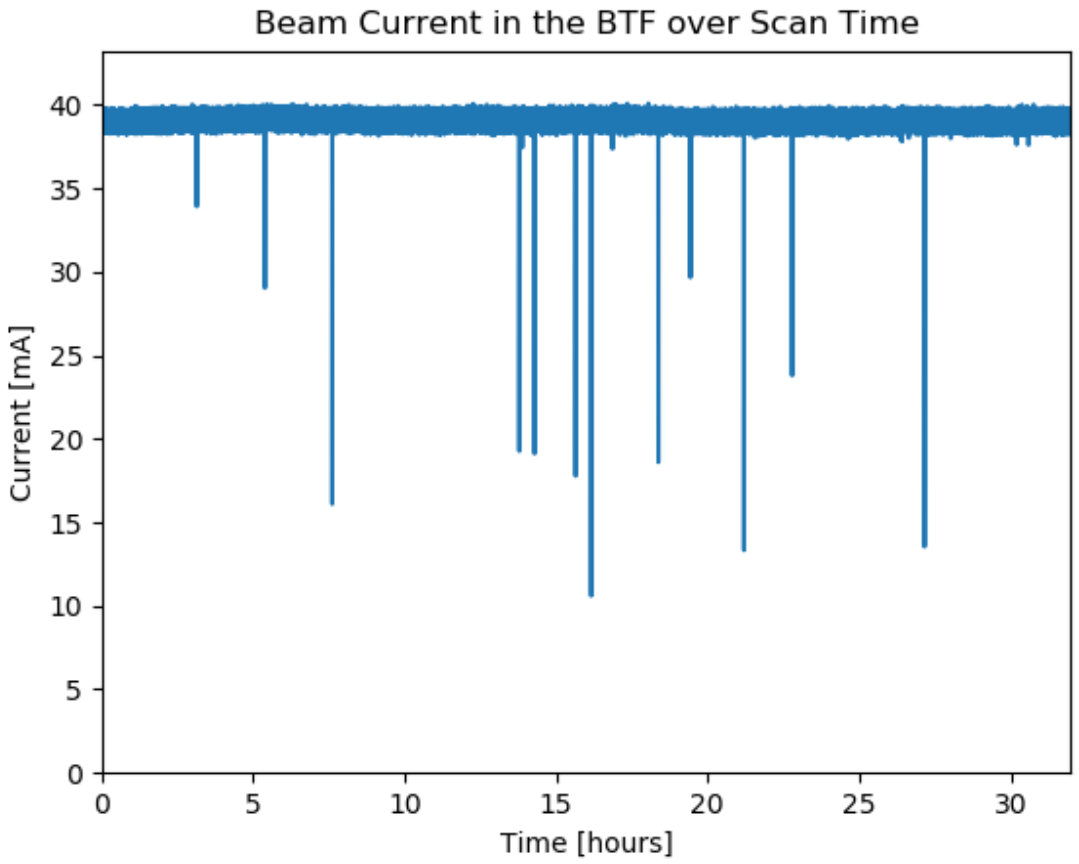

Figure 4.6: A plot of the beam current upstream of the diagnostics during the 6D scan. Notice how the beam remained very steady over the 32 hours with few dropouts. During a dropout, the scan would pause until the beam returned. The dropouts would then be removed from the data during analysis.

possible values for L_y: the distance between the horizontal slits, and the distance from the first horizontal slit to the BSM wire. Taking the total derivative gives:

$$\partial x' = \frac{1}{L_x}\partial x_2 - \frac{1}{L_x}\partial x - \frac{x_2 - x}{{L_x}^2}\partial L_x \quad \text{and} \quad \partial y' = \frac{1}{L_y}\partial y_2 - \frac{1}{L_y}\partial y - \frac{y_2 - y}{{L_y}^2}\partial L_y \tag{4.7}$$

$$\partial x' = \frac{1}{L_x}(\partial x_2 - \partial x - x'\partial L_x) \quad \text{and} \quad \partial y' = \frac{1}{L_y}(\partial y_2 - \partial y - y'\partial L_y) \tag{4.8}$$

The uncertainty in x' and y' is then:

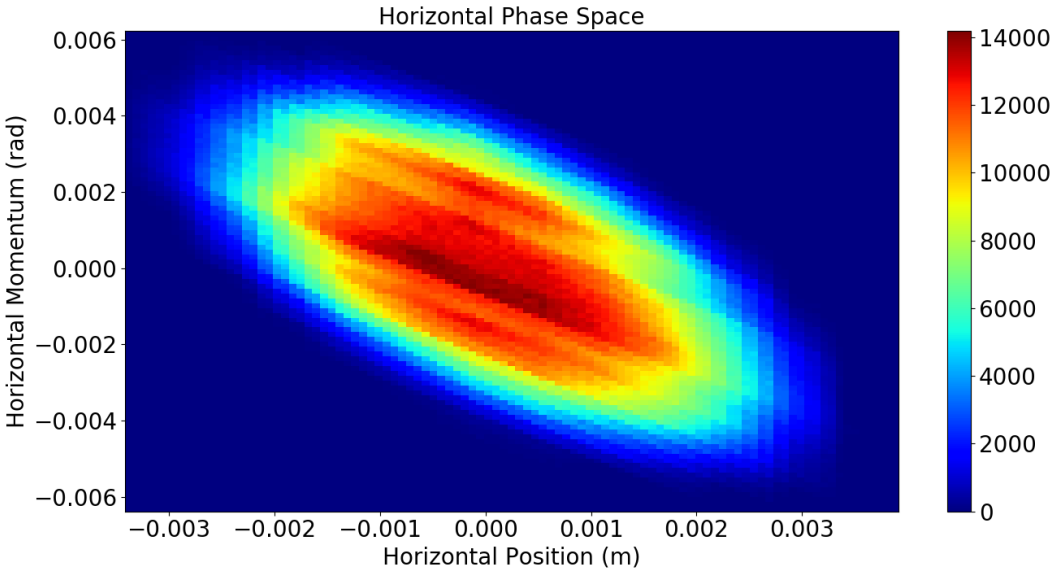

Figure 4.7: The full projection of the horizontal phase space.

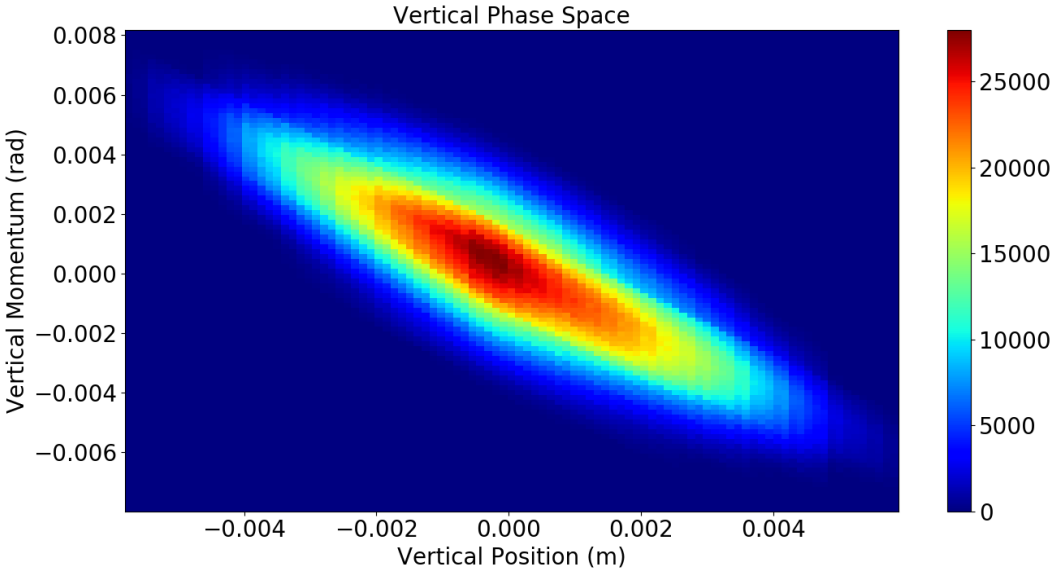

Figure 4.8: The full projection of the vertical phase space.

$$\delta x' = \pm\sqrt{\left(\frac{1}{L_x}\delta x_2\right)^2 + \left(-\frac{1}{L_x}\delta x\right)^2 + \left(-\frac{x'}{L_x}\delta L_x\right)^2} \quad \text{and}$$
$$\delta y' = \pm\sqrt{\left(\frac{1}{L_y}\delta y_2\right)^2 + \left(-\frac{1}{L_y}\delta y\right)^2 + \left(-\frac{y'}{L_y}\delta L_y\right)^2} \tag{4.9}$$

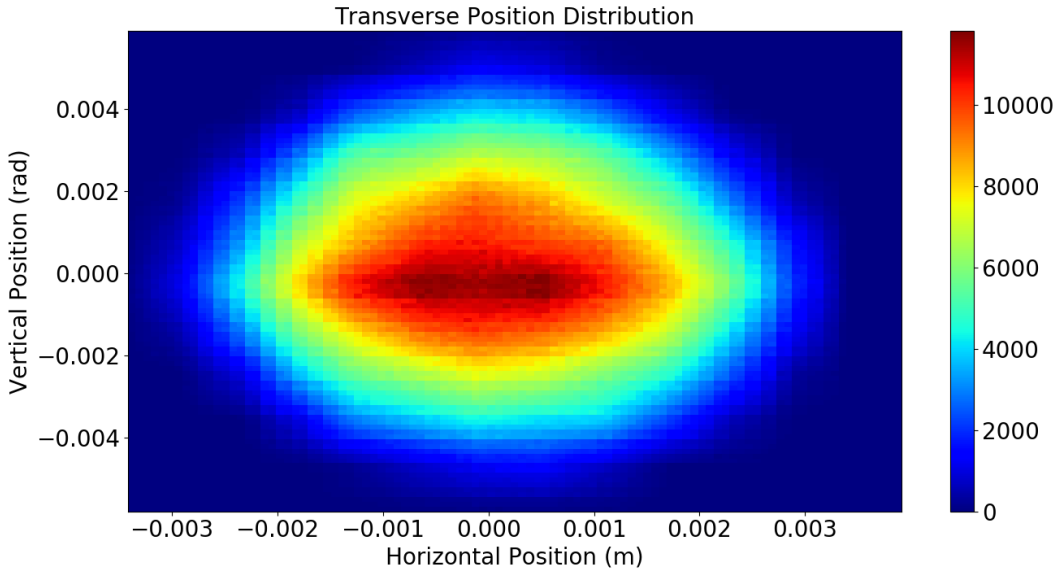

Figure 4.9: The full projection of the transverse distribution.

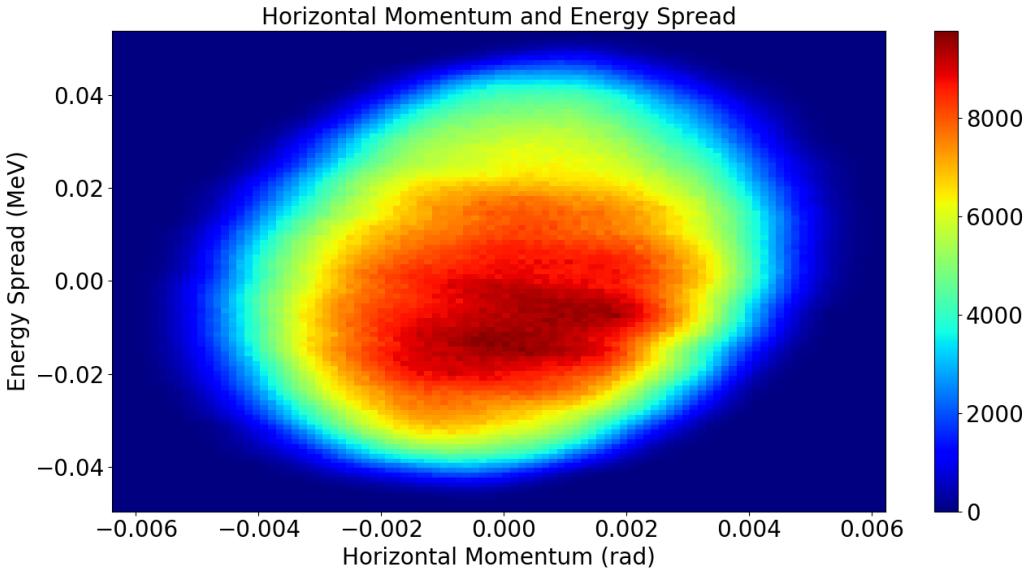

Figure 4.10: The full projection of the (x', E) subspace.

Here, $\delta x_2 = \delta x = \delta y$ and δL_x is 0.5 mm. Because x and y are relatively small ($|x'|, |y'| < 0.01\,\text{rad}$), the third term does not contribute to the final uncertainty. For 4D and 5D scans that used the slit to select y' ($\delta y_2 = \delta y, L_y = L_x$), we then have the uncertainty for x' and y' as:

$$\delta x' = \delta y' = \pm\frac{1}{L_x}\sqrt{2\delta x^2} \approx \pm 0.2\,\text{mrad} \tag{4.10}$$

However, the BSM wire was used as a y' selector for the full six-dimensional measurement. The wire is 0.2 mm wide, but only the bottom portion of the wire emits electrons which can reach the screen. We will estimate the uncertainty associated with the wire size then as 0.05 mm. The distance from the first y selector to the wire is $2.782\,\text{m} \pm 0.5\,\text{mm}$. The uncertainty is then $\delta y' \pm 0.1\,\text{mrad}$. This covers the four transverse dimensions.

4.3.2 Energy Uncertainty

To find our uncertainty in energy, we start with the equation for it from Chapter 3:

$$w(x_0, x_0', x_3) = \sqrt{D^2(x_0, x_0', x_3)((E_s + m_0)^2 - {m_0}^2) + {m_0}^2} - m_0 - E_s \tag{4.11}$$

where:

$$D(x_0, x_0', x_3) = \frac{x_3 + \frac{l}{\rho}x_0 - \left(\rho - \frac{Ll}{\rho}\right)x_0'}{l+\rho} + 1 \tag{4.12}$$

The total derivative of D is:

$$\begin{aligned}\partial D = \frac{1}{l+\rho}\partial x_3 + \frac{l}{\rho(l+\rho)}\partial x + \frac{\frac{L_w l}{\rho} - \rho}{l+\rho}\partial x' + \frac{lx'}{\rho(l+\rho)}\partial L_w \\ + \frac{(l+\rho)\left(\frac{x}{\rho} + \frac{L_w x'}{\rho}\right) - \left(x_3 + \frac{l}{\rho}x - \left(\frac{L_w l}{\rho} - \rho\right)x'\right)}{(l+\rho)^2}\partial l \\ + \frac{(l+\rho)\left(-\frac{l}{\rho^2}x + \left(\frac{L_w l}{\rho^2} - 1\right)x'\right) - \left(x_3 + \frac{l}{\rho}x - \left(\frac{L_w l}{\rho} - \rho\right)x'\right)}{(l+\rho)^2}\partial\rho\end{aligned} \tag{4.13}$$

$$\begin{aligned}\partial D = \frac{1}{l+\rho}\partial x_3 + \frac{l}{\rho(l+\rho)}\partial x + \frac{\frac{L_w l}{\rho} - \rho}{l+\rho}\partial x' + \frac{lx'}{\rho(l+\rho)}\partial L_w + \frac{x + L_w x' - \rho D + \rho}{\rho(l+\rho)^2}\partial l \\ + \frac{1 - \frac{l}{\rho^2}x + \left(\frac{L_w l}{\rho^2} - 1\right)x' - D}{l+\rho}\partial\rho\end{aligned} \tag{4.14}$$

The uncertainty in D is therefore:

$$\delta D = \pm \Bigg[\left(\frac{1}{l+\rho} \delta x_3 \right)^2 + \left(\frac{l}{\rho(l+\rho)} \delta x \right)^2 + \left(\frac{\frac{L_w l}{\rho} - \rho}{l+\rho} \delta x' \right)^2 + \left(\frac{l x'}{\rho(l+\rho)} \delta L_w \right)^2 + \left(\frac{x + L_w x' - \rho D + \rho}{\rho(l+\rho)^2} \delta l \right)^2 + \left(\frac{1 - \frac{l}{\rho^2} x + \left(\frac{L_w l}{\rho^2} - 1 \right) x' - D}{l+\rho} \delta \rho \right)^2 \Bigg]^{\frac{1}{2}} \tag{4.15}$$

Here, $\delta L_w = \delta l = 0.5\,\text{mm}$ and $\delta \rho = 0.05\,\text{mm}$. The value of δx_3 depends on the method used for measuring x_3: whether the slit or the screen is used. When using the screen, pixel size is the limiting factor (0.079 mm), making δx_3 equal to ± 0.04 mm. When using the slit, its important to remember that the dipole magnet current was adjusted while the slit remained stationary, and the uncertainty in the current is ± 0.005 A. Even though the uncertainties in each dimension are small, a linear regression of the energy screen calibration from Figure 4.2 gives a standard uncertainty in the slope of ± 0.007 mm/A, which dominates here. The current range is a little less than ± 10 A, so the maximum uncertainty for the position of the beam on the screen using the dipole current is ± 0.07 mm. However, the energy slit is 0.8 mm wide, so it dominates the position uncertainty, making δx_3 equal to 0.4 mm when using the slit.

Because both x and x' are small, the last three terms do not significantly contribute to the uncertainty. Which of the first three dominates is determined by whether the slit or screen is used to measure the energy. Therefore, δD can be written as:

$$\delta D = \pm \sqrt{ \left(\frac{1}{l+\rho} \delta x_3 \right)^2 + \left(\frac{l}{\rho(l+\rho)} \delta x \right)^2 + \left(\frac{\frac{L_w l}{\rho} - \rho}{l+\rho} \delta x' \right)^2 } \tag{4.16}$$

The above equation yields $\delta D = \pm 0.0007$ for the slit and $\delta D = \pm 0.0003$ for the screen. The total derivative for the energy spread is:

$$\partial w = \frac{D({E_s}^2 + 2E_s m_0)}{\sqrt{D^2({E_s}^2 + 2E_s m_0) + {m_0}^2}}\partial D + \left(\frac{D^2(E_s + m_0)}{\sqrt{D^2({E_s}^2 + 2E_s m_0) + {m_0}^2}} - 1\right)\partial E_s + \left(\frac{D^2 E_s + m_0}{\sqrt{D^2({E_s}^2 + 2E_s m_0) + {m_0}^2}} - 1\right)\partial m_0 \tag{4.17}$$

The uncertainty in w is then:

$$\delta w = \left[\left(\frac{D({E_s}^2 + 2E_s m_0)}{\sqrt{D^2({E_s}^2 + 2E_s m_0) + {m_0}^2}}\delta D\right)^2 + \left(\frac{D^2(E_s + m_0)}{\sqrt{D^2({E_s}^2 + 2E_s m_0) + {m_0}^2}} - 1\right)^2 {\delta E_s}^2 + \left(\frac{D^2 E_s + m_0}{\sqrt{D^2({E_s}^2 + 2E_s m_0) + {m_0}^2}} - 1\right)^2 {\delta m_0}^2\right]^{\frac{1}{2}} \tag{4.18}$$

It should be noted here that the δm_0 is the uncertainty in the mass of the proton and very small. It therefore does not contribute meaningfully:

$$\delta w = \sqrt{\frac{D^2({E_s}^2 + 2E_s m_0)^2}{D^2({E_s}^2 + 2E_s m_0) + {m_0}^2}\delta D^2 + \left(\frac{D^2(E_s + m_0)}{\sqrt{D^2({E_s}^2 + 2E_s m_0) + {m_0}^2}} - 1\right)^2 {\delta E_s}^2} \tag{4.19}$$

To find δE_s, a Beam Phase Monitor (BPM) was used. This device measures the phase of the beam when it reaches the BPM. The BPM is also movable along the beam path, so by measuring the time of arrival of the beam against the position of the BPM, the energy of the beam, E_s, can be found. The graph of the results is shown in Figure 4.11. The uncertainty in the position is ± 0.02 mm, and each phase measurement had an uncertainty of about $\pm 0.5°$. By looking at the maximum and minimum slope, the beam energy is found to be $E_s = 2.49 \pm 0.02\,\text{MeV}$.

Two graphs of δw are shown below: Figure 4.12 is with the energy slit and Figure 4.13 is with the energy screen. Both graphs have their domain limited to where particle energies were found to be measured. The curve upwards as the energy deviates from the central

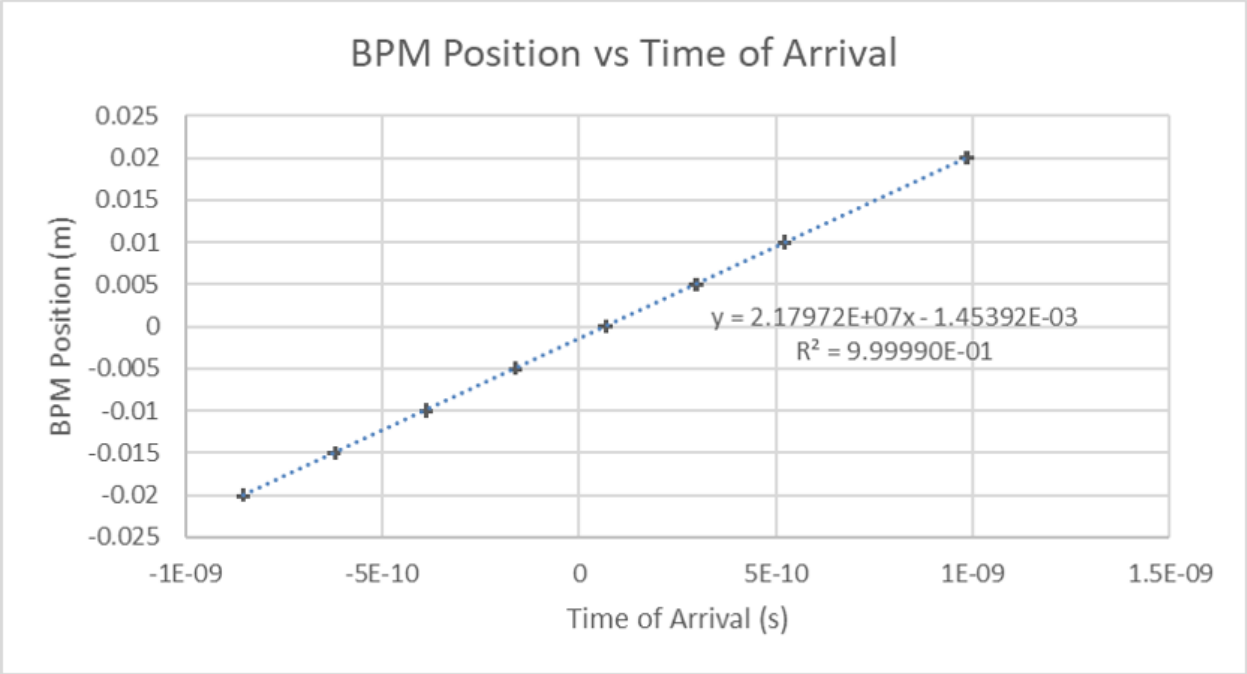

Figure 4.11: Plot showing the results of measuring the time of arrival as the BPM moved. The slope is β_s, which can be used to get E_s.

energy is caused by the δE_s term. When using the slit, δw rounds to $\pm 0.001\,\text{MeV}$. Because δE_s contributes more when using the screen, δw increases as the energy spreads from the center, but the maximum δw when using the screen is $\pm 0.0008\,\text{MeV}$.

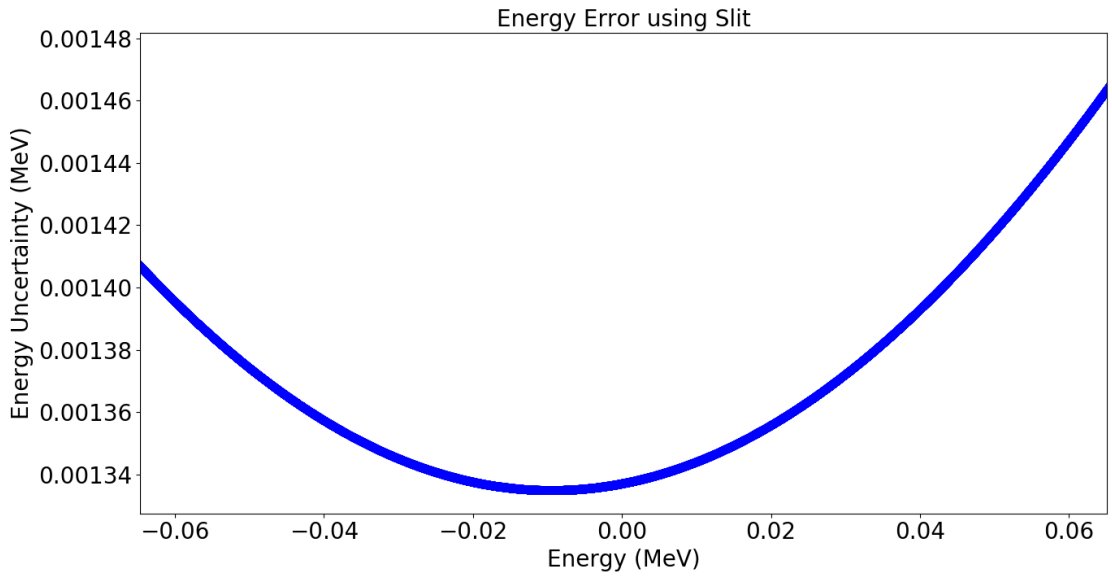

Figure 4.12: Energy uncertainty as a function of energy for the energy slit.

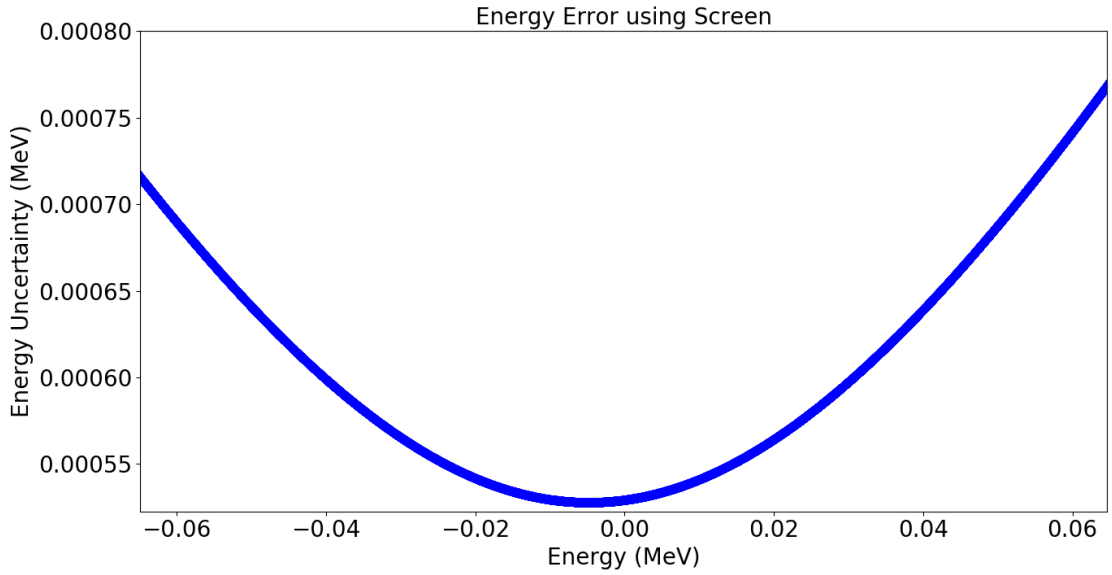

Figure 4.13: The energy uncertainty as a function of energy for the energy screen.

4.3.3 Phase Uncertainty

The final dimension is the phase of a particle. The BSM phase is accurate to a degree, so its uncertainty is $\pm 0.5°$. Figure 4.3 shows the calibration of the BSM screen, and by using the maximum and minimum slopes from uncertainties in the phase and pixel measurement, the uncertainty in the calibration comes to ± 0.01 degrees/pixel. The vertical axis of the camera has 300 pixels, which gives a maximum uncertainty of $\pm 2°$. Finally, one pixel has a range of 0.396 degrees, which is another uncertainty of $\pm 0.2°$. The total uncertainty in the phase measurement is then:

$$\delta\phi = \pm\sqrt{(0.5°)^2 + (2°)^2 + (0.2°)^2} \approx \pm 2° \tag{4.20}$$

To offer some perspective, $\pm 2°$ at a beam frequency of 402.5 MHz is equal to ± 14 ps.

There is a particular issue that needs to be noted. Because the energy and phase are so heavily correlated, the uncertainty contribution to the charge measurement from their cross term cannot be ignored. The relationship between the dipole current and the phase measured on the BSM is about 100 degrees/A. Using the relationship between current and the position on the energy screen, this becomes 84 degrees/mm. When this is combined with

the fact that the energy slit is 0.8 mm wide, the problem becomes apparent. Depending on how narrow the phase spread is for a given dipole current, we may not be sufficiently isolating the energy to properly resolve the phase. For example, if the actual phase spread at a given energy is 50°, the measured phase spread would appear further spread out as all the phases that travel through the slit are integrated. Figure 4.14 demonstrates this example. The importance of this relationship has not been fully studied but will need to be assessed when the BTF resumes six-dimensional measurements.

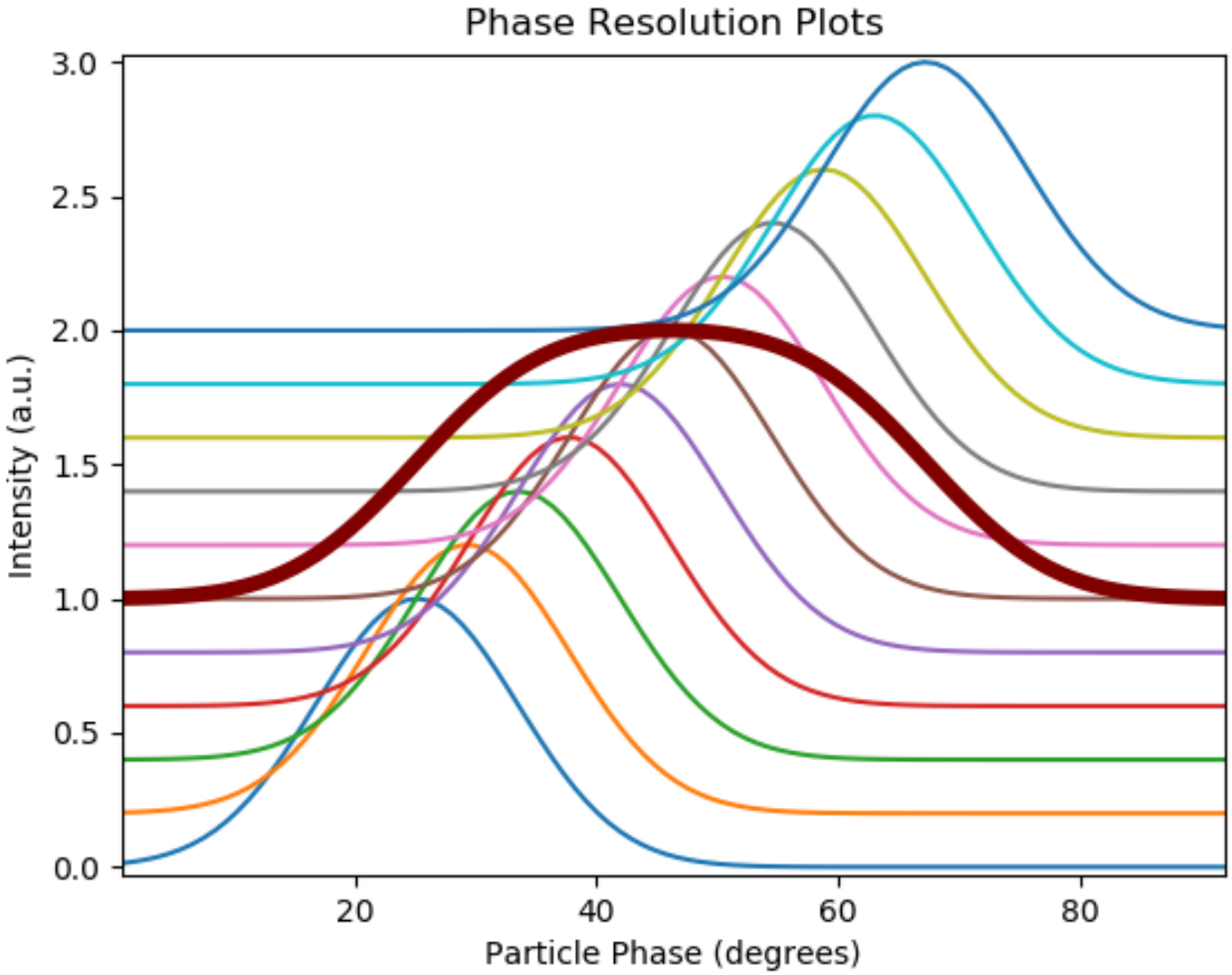

Figure 4.14: Demonstration of how the phase dimension may not have been sufficiently decoupled from the energy. The thin lines are gaussian curves centered at different phases with artificial vertical offsets to represent the phase/energy correlation. The thick line is a normalized sum of the series of thin lines. If the actual phase spread is too small (a thin line), the 6D scan (the thick line) will not accurately measure the phase distribution.

4.4 Energy Correlation

A clearly visible correlation was found between the transverse degrees of freedom and the energy [1]. Figure 4.15 shows a 2D color map of the $p(x', w)$ partial projection with $x = y = y' = 0$ (these slits were fixed in the beam center while the x' slit scanned the beam) and integrated over ϕ (the energy screen was used). A dependence of the w profile upon the coordinate value x' is obvious in the plot. The w distribution showed similar dependence with x, y, and y' as well.

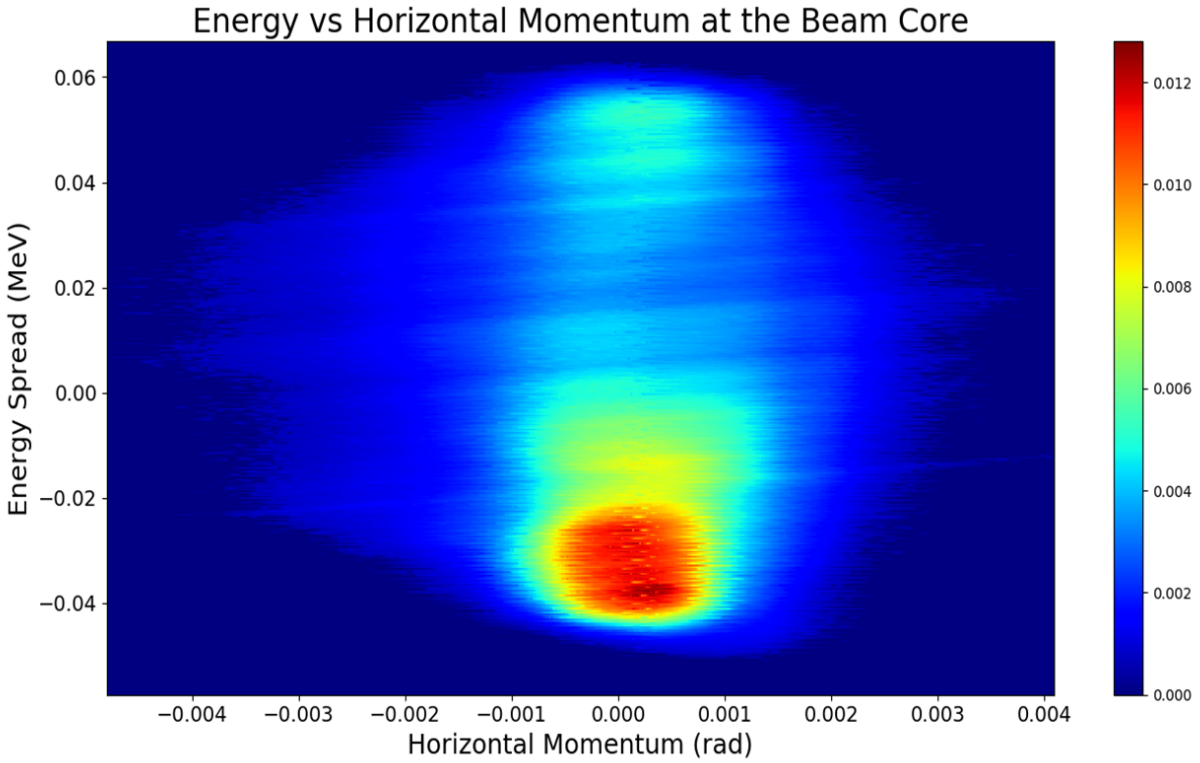

Figure 4.15: A partial projection plot of the energy spread, w, against the horizontal momentum, x'.

The multidimensional nature of the observed correlation is illustrated in Figure 4.16 with plots derived from a 5D scan with integration over ϕ. Several 1D partial projections for different values of x' are plotted on the right. A full projection on the energy axis (i.e., the energy spectrum) is plotted on the left. The full beam energy spectrum projection does not show any hint of the complex internal structure of the distribution visible on the partial

projections. It should be noted that the uncertainty in energy is small enough to validate these results.

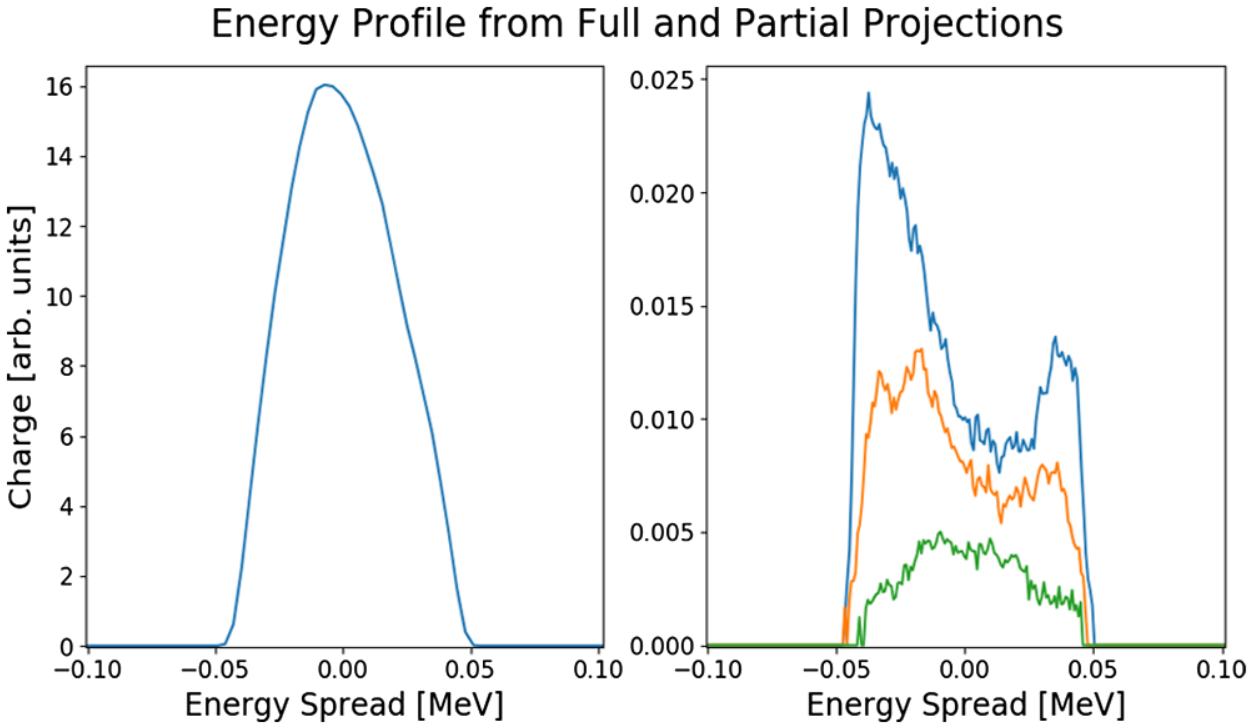

Figure 4.16: Results from a 5D scan. The left plot shows the total projection of the energy spectrum. The right shows different 1D partial projections of energy with three different horizontal momentums. The blue curves x0 is about 0.2 mrad, the yellows is about 0.7 mrad, and the greens is about 1 mrad.

The plots in Figure 4.17 show 1D partial projection energy spectrums with different numbers of fixed coordinates: the green line shows the energy spectrum measured with $x = x' = 0$ and integrated over y and y'; the red line shows the energy spectrum measured with $x = x' = y = 0$, integrated over y'; and the blue line shows the energy spectrum measured with $x = x' = y = y' = 0$. All three measurements are integrated over ϕ. The plots demonstrate the necessity of performing the scan in at least 4D for the correlation to become visible, and in 5D for resolving the details. The plots in Figure 4.18 show 1D partial projections with four fixed coordinates $x = x' = y = y' = 0$ (all slits fixed at the beam center) measured for beam currents of 40, 30, and 20 mA. The correlation is well pronounced at 40 mA, becomes less visible with a smaller beam current of 30 mA, and completely disappears

at 20 mA. This measurement convincingly demonstrates that the observed correlation is created by the Coulomb forces within the distribution.

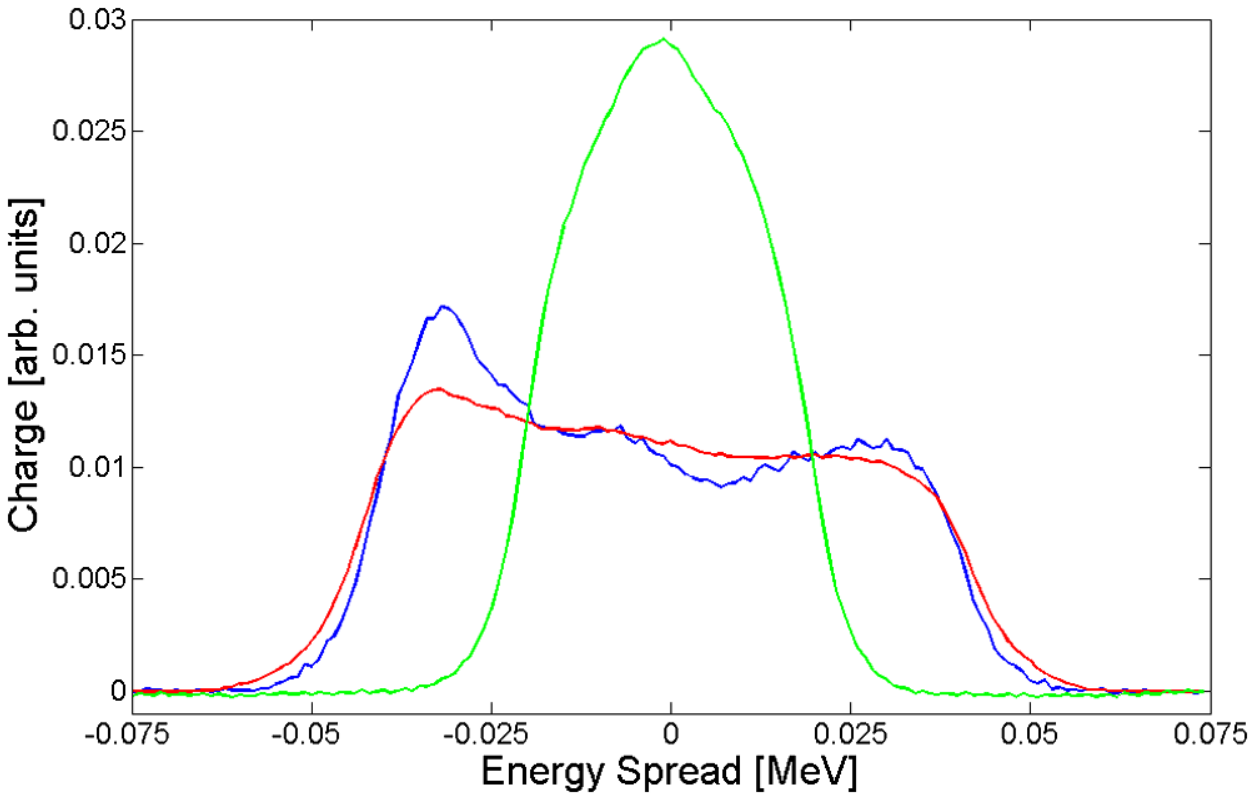

Figure 4.17: Plots of three different 1D partial projections on energy. Each plot has a different number of fixed slits near the center of the beam. The green curve fixes two slits, the red curve fixes three, and the blue curve fixes four. The curves are normalized by area.

While a precise simulation using the measured distribution is left for future work, a simple computer simulation is sufficient to elucidate the beam physics. A meter long transport line consisting of drifts and four quadrupole magnets arranged similarly to the first meter of the BTF beam line was simulated using PARMILA particle-in-cell code [28]. An ideal 6D Gaussian function was used to generate the initial particle coordinates. Partial projections on the w, y' plane of the distribution function at the beam line exit are shown in Figure 4.19 for two cases: a 10 mA and a 100 mA beam current. A pattern similar to the measurement in Figure 4.15 is clearly visible only on the projection for high beam current, confirming that Coulomb forces are responsible for creating this correlation in the 6D phase space distribution. Furthermore, it is interesting to note that reproducing the correlation in simulation does not require any novel or complex beam physics. Parallel with the experiment,

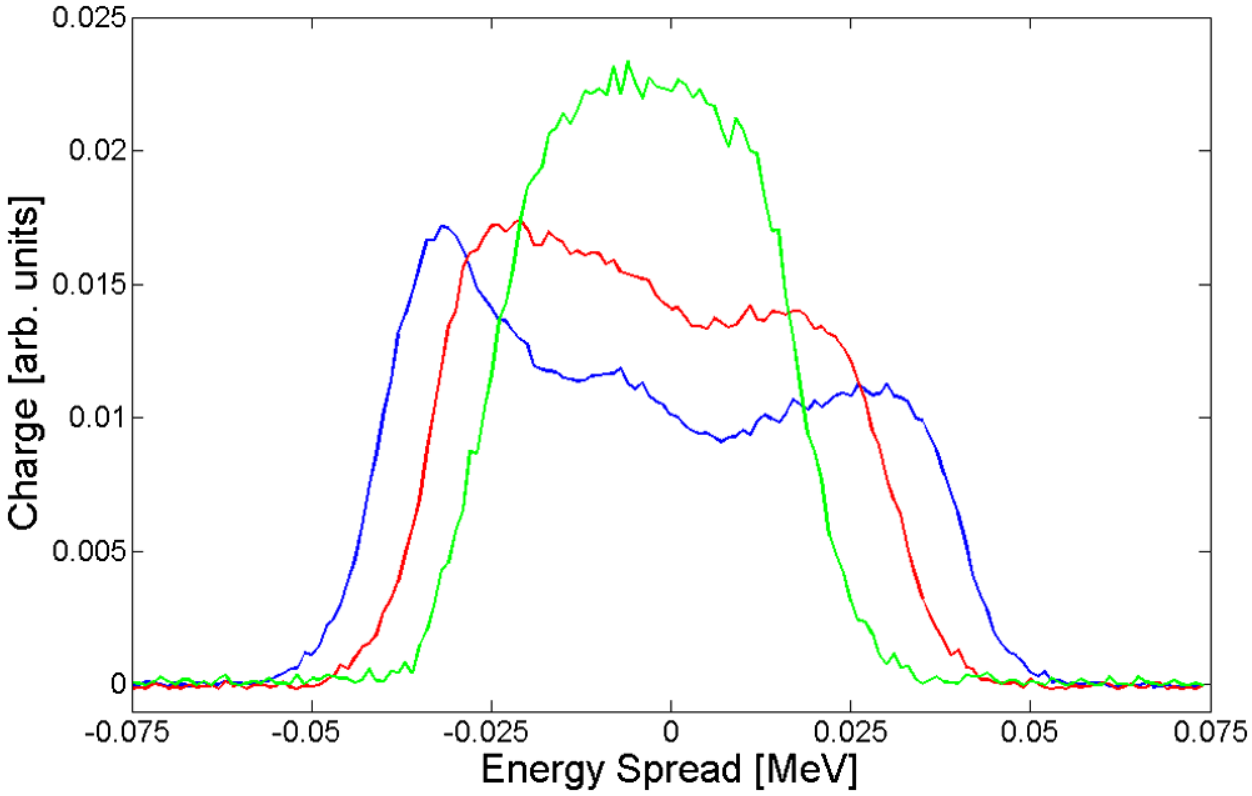

Figure 4.18: Plots of partial projections on energy with three different beam currents. The green curve is from 20 mA, the red curve is from 30 mA, and the blue curve is from 40 mA. The correlation is more pronounced with increasing current, which indicates Coulomb forces cause the correlation. The curves are normalized by area.

the key is knowing to look at the partial rather than the integrated 2D projection (e.g. to maintain a high dimensional approach when viewing the lower dimensional subspaces). This reinforces the notion that the full 6D distribution is required for a complete understanding of the beam physics.

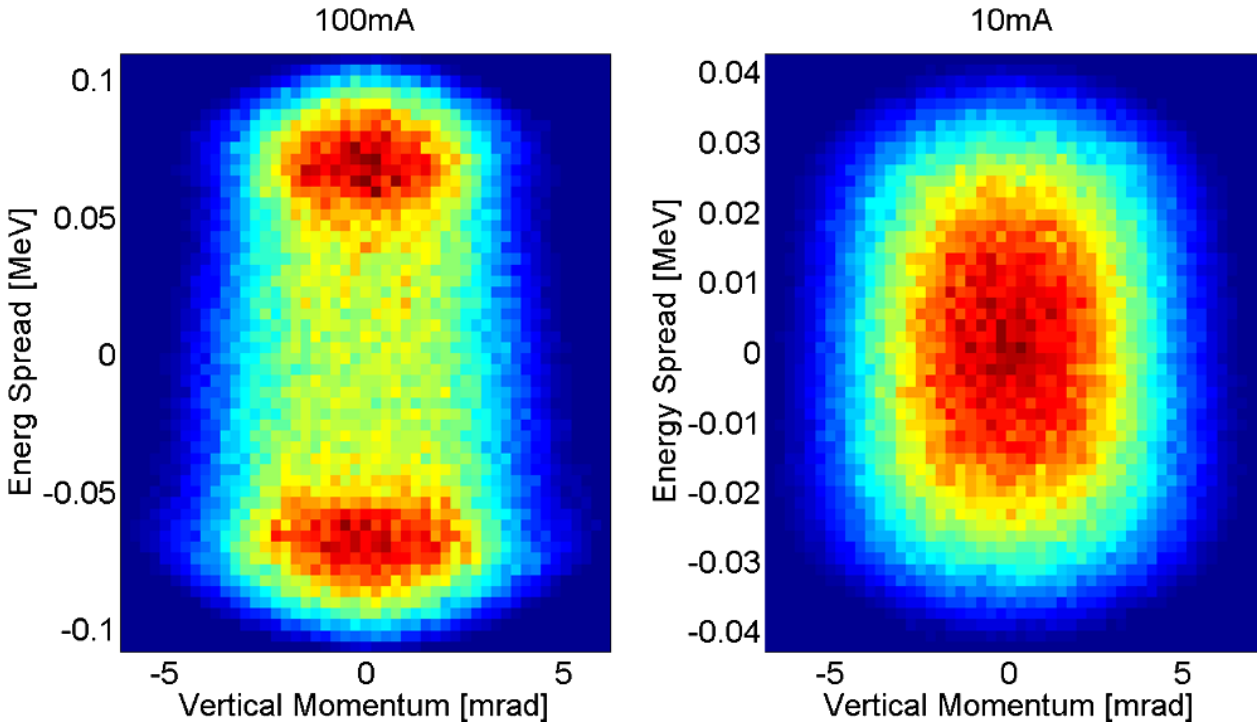

Figure 4.19: Two plots of the partial projection of the energy spread w against the vertical momentum y' for a 100 mA (left) and a 10 mA (right) simulated beam transport.

Chapter 5

Conclusion

In order to build better accelerators, simulations need to accurately predict beam evolution, including beam loss. The most likely explanation for their failure to do so is an incorrect initial distribution provided for the simulations. This experiment is the first ever measurement of the full six-dimensional phase space of an accelerator beam distribution to determine the correct initial distribution.

Results from the measurement showed a hidden relationship between the energy and the transverse phase space of the distribution that had never previously been observed. This proves that non-conjugate degrees of freedom can be correlated and invalidates the long-time assumption that they were not. The correlation was shown to be beam intensity dependent and therefore an effect of Coulomb interactions.

The time required to complete a scan is the largest limiting factor for higher dimensionality scans. This limitation was partially diminished with the use of luminescent screens to measure the energy or the phase. Figure 5.1 shows a plan to significantly decrease scan time by removing the energy slit so that the two longitudinal dimensions can be completely measured simultaneously. In this manner, the BSM screen simultaneously measures energy and phase on different axes. In the future, the BTF beamline will be extended with a series of adjustable quadrupoles and end with a second 4D transverse emittance station (Figure 5.2). This second diagnostic station will be used to study beam propagation through the quadrupoles and benchmark simulations against the final measured distributions [29].

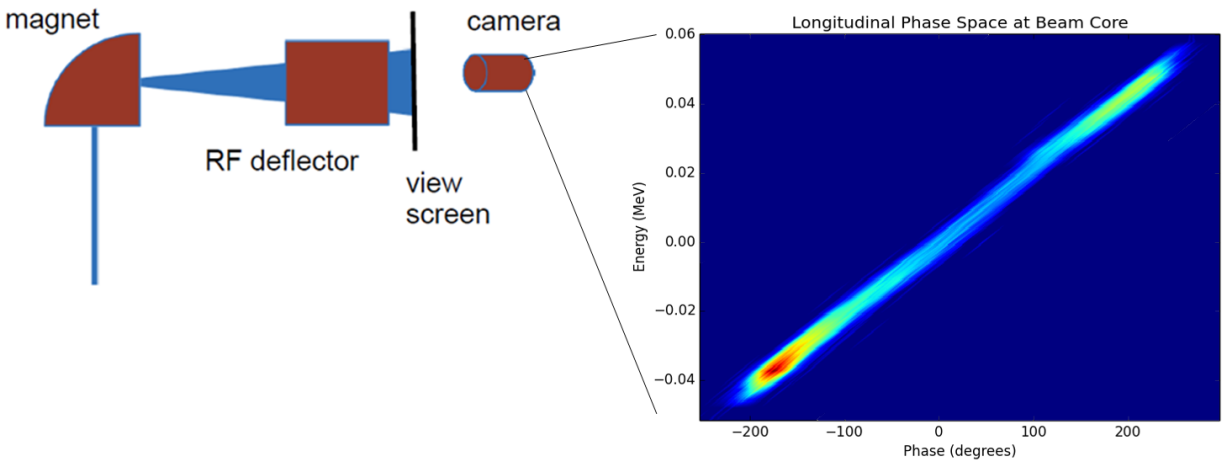

Figure 5.1: Proposed plan to measure the entire 2D longitudinal phase space simultaneously. While the graph on the right was measured at each energy separately, this plan will measure the full longitudinal space in a single pulse.

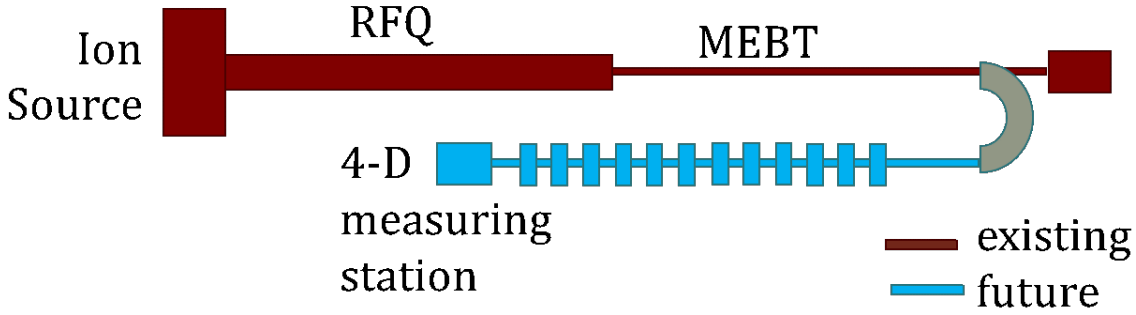

Figure 5.2: Plan showing the addition (in blue) to the BTF of quadrupoles and a 4D diagnostic station.

While the discovery of a correlation already significantly advances our understanding of particle beam distributions in a linear hadron accelerator, future high dimensionality measurements at the BTF will utilize the new beam line to look closely at such correlations between the degrees of freedom and investigate their impact on the beam evolution. Because the BTF is a duplicate of the SNS front-end, the initial distribution measured in the BTF also applies to the SNS. With an accurate measurement of the initial distribution, simulations can be tested and improved so that beam loss is correctly predicted. With correct simulations, improved accelerators with new and novel designs can be built.

Bibliography

[1] Brandon Cathey, Sarah Cousineau, Alexander Aleksandrov, and Alexander Zhukov. First six dimensional phase space measurement of an accelerator beam. *Physical Review Letters*, 121(6):064804, 2018. v, 63

[2] J Qiang, P L Colestock, D Gilpatrick, H V Smith, T P Wangler, and M E Schulze. Macroparticle simulation studies of a proton beam halo experiment. *PRSTAB*, 5(124201):705–706, 2002. 2

[3] S Machida and R D Ryne. Summary of session C: Space charge simulation and experiment. In *Proceedings of ICFA HB2004*, page 454, 2004. 2

[4] S Cousineau and I Hofmann. Working session B summary: Space charge theory, simulations and experiments. In *Proceedings of ICFA HB2006*, page 363, 2006. 3

[5] A Aleksandrov, I Hofmann, and J-M Lagneil. Summary report of the working group b: Beam dynamics in high intensity linacs. In *Proceedings of Hadron Beam 2008*, page 485, 2008. 3

[6] M Plum, Y Sato, and R Schmidt. Summary of the working group on commissioning and operations. In *Proceedings of ICFA HB2012*, page 620, 2012. 3

[7] C K Allen, K C D Cha, P L Colestock, R W Garnett, J D Gilpatrick, W P Lysenko, J D Schneider, R L Sheffield, H V Smith, T P Wangler, J Qiang, K R Crandall, and M E Schulze. Experimental study of proton beam halo in mismatched beams. In *Proceedings of LINAC2002*, page 395, 2002. 3

[8] Jean-Claude Denard. Beam current monitors. 2009. 3

[9] Peter Forck, D Liakin, and P Kowina. Beam position monitors. 2009. 3

[10] A Bosco, MT Price, GA Blair, ST Boogert, G Boorman, S Malton, C Driouichi, T Kamps, F Poirier, K Balewski, et al. A two-dimensional laser-wire scanner for electron accelerators. *Nuclear Instruments and Methods in Physics Research Section A: Accelerators, Spectrometers, Detectors and Associated Equipment*, 592(3):162–170, 2008. 3

[11] S Nath, J Billen, J Stovall, H Takeda, L M Young, K Crandall, and D Jeon. Particle-beam behavior in the sns linac with simulated and reconstructed beams. In *Proceedings of PAC2003*, page 1515, 2003. 4

[12] C. Xiao, M. Maier, X. N. Du, P. Gerhard, L. Groening, S. Mickat, and H. Vormann. Rotating system for four-dimensional transverse rms-emittance measurements. *Phys. Rev. Accel. Beams*, 19:072802, Jul 2016. 4, 23

[13] Eduard Prat, Masamitsu Aiba, Simona Bettoni, Bolko Beutner, Sven Reiche, and Thomas Schietinger. Emittance measurements and minimization at the swissfel injector test facility. *Phys. Rev. ST Accel. Beams*, 17:104401, Oct 2014. 4, 23

[14] T. P. Wangler, K. R. Crandall, R. Ryne, and T. S. Wang. Particle-core model for transverse dynamics of beam halo. *Phys. Rev. ST Accel. Beams*, 1:084201, Dec 1998. 4

[15] V. Danilov, S. Cousineau, S. Henderson, and J. Holmes. Self-consistent time dependent two dimensional and three dimensional space charge distributions with linear force. *Phys. Rev. ST Accel. Beams*, 6:094202, Sep 2003. 4

[16] H. R. Kremers, J. P. M. Beijers, and S. Brandenburg. A pepper-pot emittance meter for low-energy heavy-ion beams. *Rev. Sci. Instrum.*, 84:025117, 2013. 4, 25

[17] V Yakimenko, M Babzien, I Ben-Zvi, R Malone, and X-J Wang. Electron beam phase-space measurement using a high-precision tomography technique. *Physical Review Special Topics-Accelerators and Beams*, 6(12):122801, 2003. 5, 25

[18] D Stratakis, RA Kishek, H Li, S Bernal, M Walter, B Quinn, M Reiser, and PG OShea. Tomography as a diagnostic tool for phase space mapping of intense particle beams. *Physical Review Special Topics-Accelerators and Beams*, 9(11):112801, 2006. 5, 25

[19] Michael Röhrs, Christopher Gerth, Holger Schlarb, Bernhard Schmidt, and Peter Schmüser. Time-resolved electron beam phase space tomography at a soft x-ray free-electron laser. *Physical Review Special Topics-Accelerators and Beams*, 12(5):050704, 2009. 5, 25

[20] S. Hancock, Shane R. Koscielniak, and M. Lindroos. Longitudinal phase space tomography with space charge. pages 1726–1728, 2000. 5, 25

[21] D Stratakis, RA Kishek, I Haber, RB Fiorito, JCT Thangaraj, K Tian, C Papadopoulos, M Reiser, and PG O'Shea. Phase space tomography of beams with extreme space charge. In *Particle Accelerator Conference, 2007. PAC. IEEE*, pages 2025–2029. IEEE, 2007. 5, 25

[22] Gerald N Minerbo, OR Sander, and RA Jameson. Four-dimensional beam tomography. *IEEE Transactions on Nuclear Science*, 28(3):2231–2233, 1981. 5, 25

[23] V Danilov and A Aleksandrov. Beam invariants for diagnostics. In *Proceedings of EPAC2004*, pages 1518–1520, 2004. 5

[24] A Aleksandrov, M Champion, M Crofford, K Ewald, Y Kang, A Menshov, M Middenorf, S Murry, R Saethre, M Stockli, A Webster, R Welton, and A Zhukov. Status of the new 2.5 mev test facility at sns. In *Proceedings of LINAC2014*, page 1105, 2014. 6, 28

[25] IM Kapchinskij and VV Vladimirskij. Limitations of proton beam current in a strong focusing linear accelerator associated with the beam space charge. In *Proceedings of the 2nd International Conference on High Energy Accelerators*, page 274, 1959. 23

[26] A V Feschenko. Methods and instrumentation for bunch shape measurements. In *Proceedings of PAC2001*, page 517, 2001. 39

[27] A.P. Zhukov et al. Open XAL Status Report 2018. In *Proc. 9th International Particle Accelerator Conference (IPAC'18), Vancouver, BC, Canada, April 29-May 4, 2018*, number 9 in International Particle Accelerator Conference, pages 3388–3391. JACoW Publishing, 2018. 41

[28] JH Billen and H Takeda. Parmila manual. Technical report, Report LAUR-98-4478, Los Alamos, 1998 (Revised 2004), 1998. 65

[29] Z.L. Zhang, A.V. Aleksandrov, and S.M. Cousineau. FODO Lattice Design for Beam Halo Research at SNS. In *Proc. of International Particle Accelerator Conference*

(IPAC'17), Copenhagen, Denmark, 1419 May, 2017, number 8 in International Particle Accelerator Conference, pages 2449–2451. JACoW, 2017. 68

Vita

Brandon Lee Cathey was born in 1989 in Nashville, TN to Ricky and Jan Cathey. Raised in Murfreesboro, TN, Brandon and his sister Erica both attended Buchanan Elementary, McFadden School of Excellence, and Siegel High School. While already intrigued by physics, Brandon's passion for this field of study was cultivated his junior year by his mother, who taught his first physics course. That following summer, he began his research career by attempting to create superluminal sound pulses under Dr. William Robertson of Middle Tennessee State University (MTSU). Following graduation from high school, Brandon pursued his undergraduate degree at MTSU where he studied both physics and chemistry. During his fifth year, he served as President of MTSU's chapter of the Society of Physics Students. In 2012, Brandon obtained a Bachelor of Science degree with a double major in Physics and Chemistry from MTSU. After graduating, he interned at Oak Ridge National Labs with the Spallation Neutron Source under Dr. Sarah Cousineau. In 2013, Brandon began his doctoral studies in physics at The University of Tennessee, working first as a Teaching Research Assistant before becoming a Graduate Research Assistant under Dr. Alexander Aleksandrov. This project provided him the opportunity to travel to Denmark, Germany, Canada, and China to present his research at several Particle Accelerator conferences, and in August 2018, his research was published in *Physical Review Letters* and selected as an Editor's Choice. Brandon completed his graduate studies at The University of Tennessee in December 2018 and received a Doctor of Philsophy in Physics.